Bottom Boundary Layer Instabilities Induced By Nonlinear Internal Waves

by Themistoklis Stefanakis

BOTTOM BOUNDARY LAYER INSTABILITIES INDUCED BY NONLINEAR INTERNAL WAVES

A Thesis

Presented to the Faculty of the Graduate School

of Cornell University

in Partial Fulfillment of the Requirements for the Degree of

Master of Science

by

Themistoklis Stefanakis

August 2010

ABSTRACT

Internal solitary waves (commonly referred to as "nonlinear internal waves" due to the balance between nonlinearity and dispersion, with the intense nonlinearity represented by very strong thermocline displacement in nature) are a ubiquitous feature of coastal ocean, lakes and the atmosphere. Over the past four decades, significant progress has been made in the study of internal solitary waves (mostly in the ocean and in lakes) through combined field, laboratory, numerical and theoretical work. Their interaction with the seafloor is, however, a phenomenon that has only began to be understood during the last decade. In situ observations have shown strong resuspension of sedimentary material in the footprint of internal solitary waves propagating over a gently shoaling bottom topography. Ongoing research through laboratory experiments and numerical simulations, during the last decade, has tried to shed light on the dynamics of benthic excitation under nonlinear internal waves, namely providing a qualitative description of the primary shear instability in the wave-driven bottom boundary layer (BBL).

In the current study, 2-D direct numerical simulations (DNS) have been performed in order to investigate the dynamics of the BBL under fully nonlinear internal waves (NLIWs) (as contrasted to weakly nonlinear internal waves described by the appropriate Korteweg-deVries equation). Both elevation and depression waves propagating in a uniform depth two-layer stratification have been examined, with emphasis placed on the latter. The use of a spectral multidomain penalty method

model enables the accurate and robust description of the wave-induced BBL at values of Reynolds number (based on NLIW phase speed and wave-guide depth) as high as 100,000. The BBL under elevation waves is found to be stable in most circumstances, but further investigation of a baroclinically-driven instability, observed in some cases, is needed. On the other hand, spontaneous (initiated without any external noise) and intermittent global near-bed instabilities and subsequent vortex shedding are found to occur in the footprint of depression waves, in the separated BBL behind the wave trough, when the wave amplitude surpasses a critical value, which decreases with increasing Reynolds number, oncoming current strength and deeper thermocline. However, an instantaneous insertion of external noise may excite the NLIW-induced BBL and lead to instability development at even lower amplitudes.

Our findings suggest that the destabilization of the NLIW-induced BBL in the adverse pressure gradient region is highly sensitive to upstream flow conditions near the bed (oncoming current, potentially seeded with turbulence and the impact of leading wave). The structure of the numerically reproduced NLIW-induced BBL shows strong similarities with its laboratory counterpart, although significant questions remain about the role of three dimensional effects and the initialization of the experiments. Finally, based on our results, we propose that the observed instability mechanism can drive a potent turbulence in near-bed wake in the trailing edge of NLIWs in the actual ocean, thus causing significant NLIW dissipation and providing a highly likely means of sediment resuspension.

BIOGRAPHICAL SKETCH

The author was born on June 27 1984 in Athens, Greece. He did his 5-year undergraduate studies at the National Technical University of Athens in the Department of Civil Engineering having Hydraulic Engineering as concentration. His diploma thesis was on the hydrological properties of a catchment in Northern Greece. In 2008 he came to Cornell University and started the Master of Science program in Environmental Fluid Mechanics & Hydrology and conducted research under the supervision of Professor Peter Diamessis on the bottom boundary layer induced by nonlinear internal waves, which is the subject of this thesis.

This thesis is dedicated to my family for guiding and supporting me all those years.

ACKNOWLEDGEMENTS

I would like to warmly thank Professor Peter Diamessis for giving me the opportunity to come to Cornell and study internal waves as well as computational fluid dynamics. He was an inspiring advisor and on his side I learnt what academic professionalism means not only in terms of science, but also in terms of personal relations. I would also like to thank Professor Edwin Cowen for giving me the opportunity to serve as a teaching assistant and gain laboratory experience as well as refreshing interaction with undergraduate students. Moreover, I would like to acknowledge Professor Larry Redekopp (USC) for his insightful remarks, which gave us food for thought. Last but not least, I would like to thank all the students of the Environmental Fluid Mechanics lab for welcoming me in their family and for generously helping me whenever I asked.

TABLE OF CONTENTS

LIST OF TABLES

LIST OF FIGURES

CHAPTER 1

INTRODUCTION

1.1 Fundamentals of Internal Waves

1.1.1 Description and Early Observations

Internal gravity waves (hereafter referred as internal waves or IWs), are waves that travel in the interior of a fluid in contrast with surface waves that travel at the interface of air and liquid. IWs are density waves and as such, they can be observed in fluids which are stratified. In environmental flows, this is the case with the ocean, lakes and the atmosphere.

Internal gravity waves are distinguished into two main categories depending on the ambient stratification profile (Figure 1.1). In the first category belong the waves that propagate in a continuously stratified fluid. They are usually generated by some disturbances inside the stratified fluid such as an oscillating cylinder, like in the laboratory experiments of Mowbray and Rarity [76] (Figure 1.2). In this case, the wave phase speed and the group velocity are perpendicular, while the wavelength is comparable to the scale of the source. An important quantity is the frequency at which the water particles will oscillate under the combined effects of gravity and buoyancy forces and is called Brunt-Väisälä or buoyancy frequency (Eq. (1.1)). The dispersion relation associated with these waves is given in Equation (1.2).

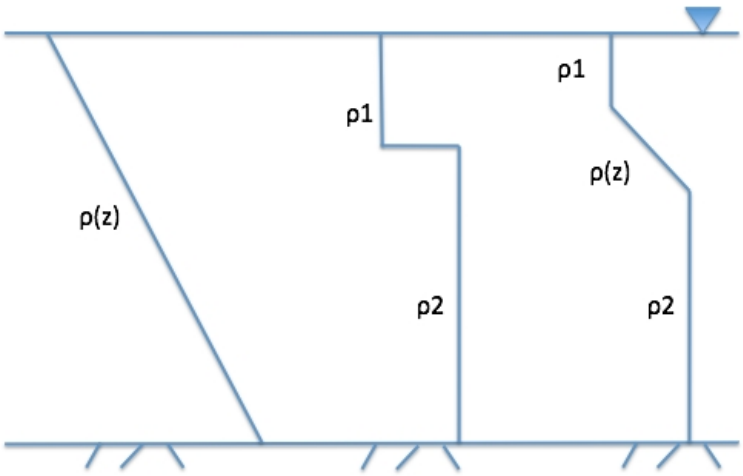

Figure 1.1: Schematic of stratification profiles. On the left an example of continuous stratification, in the middle, an example of a two-layer system and on the right an example of a two layer system with a thermocline.

$$N(z) = \sqrt{-\frac{g}{\rho}\frac{d\rho}{dz}} \tag{1.1}$$

$$\omega^2 = N^2 \sin^2\beta \tag{1.2}$$

Where β is the angle the wave ray forms with the horizontal.

On the other hand, the second category consists of internal interfacial waves which are observed at density interfaces and are long waves. In this case, the group velocity and the wave phase speed are in the same direction. When internal interfacial waves reach the shallow water limit (horizontal length scale is much greater than the vertical length scale), their vertical modal structure can be expressed as the solution

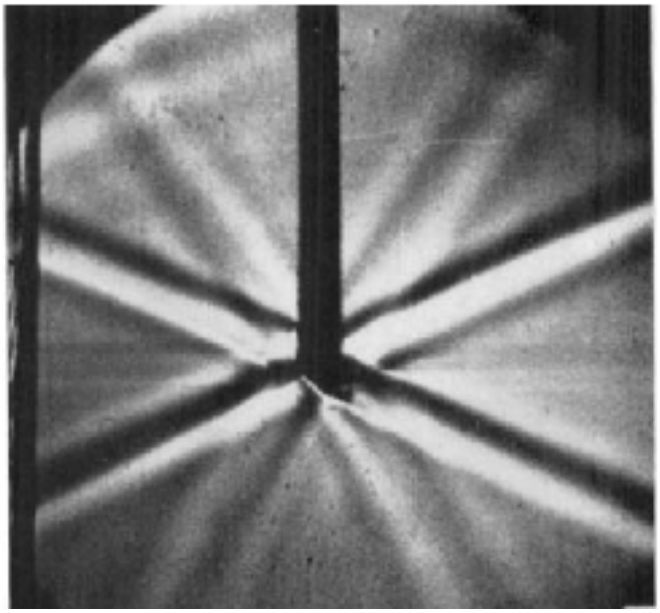

Figure 1.2: Ray propagation of internal waves. Image shows internal wave rays generated and radiating away from a cylinder that is oscillating horizontally in a stratified salt solution with uniform buoyancy frequency N. The cylinder is seen end-on and driven by thin vertical bars that appear black in the image. The light and dark bands are lines of constant phase in a St Andrew's cross pattern caused by the distortion to the density field produced by waves spreading radially away from the cylinder at an angle β with the horizontal, which is the energy propagation direction. From Mowbray and Rarity [76]

of an eigenvalue problem [96]. Internal interfacial waves can be either periodic or solitary. Solitary wave is a traveling wave which is neither preceded nor followed by any wave that has the exact same form. The solitary waveform is the result of the balance between nonlinearity and dispersion. When nonlinearity is strong, then the wave amplitude can reach values of the order of 50 meters in 100 meter water depth. The present study deals with mode-1 nonlinear internal solitary waves, also

known as nonlinear internal waves (NLIWs).

This study is mostly focused on the oceanic case, but examples of NLIWs can also be found in lakes [7] [30] [49] [84] [97] and in the atmosphere such as the Morning Glory bore of the Gulf of Carpentaria in northeast Australia [22]. The ocean typically consists of a well mixed upper layer of warmer and less dense water overlying a thermocline (a zone where the seawater density changes), where the density variation is linear and confined over a narrow region, and either a well mixed lower layer of cold, denser and more saline water or a more diffuse layer (weaker stratification). Any excitation or disturbance of the thermocline will tend to propagate away from the region of generation as an internal wave [3]. In the coastal ocean, internal waves (Figure 1.5) are usually generated by the interaction of the local bathymetry with the tidal currents close to the continental shelf [65] [31].

Advances in the study of NLIWs date back in the 1960s when the development of fast internally recording vertical thermistor arrays made possible the observation of NLIWs in the coastal oceans [43]. Early measurements by Lee (1961) [60], Perry & Schimke (1965), Ziegenbein (1969, 1970) [104] [105], Halpern (1971) [40], Lee & Beardsley (1974) [59] , Apel et al. (1975) [4] have shown that the amplitudes of these waves were quite large compared with the thermocline thickness in order to be considered linear waves. Moreover, the fact that they travelled long distances without significant changes in shape and amplitude suggested that these internal waves were not dispersive waves. Thus, given the fact that the wave amplitude was too large to be described by linear

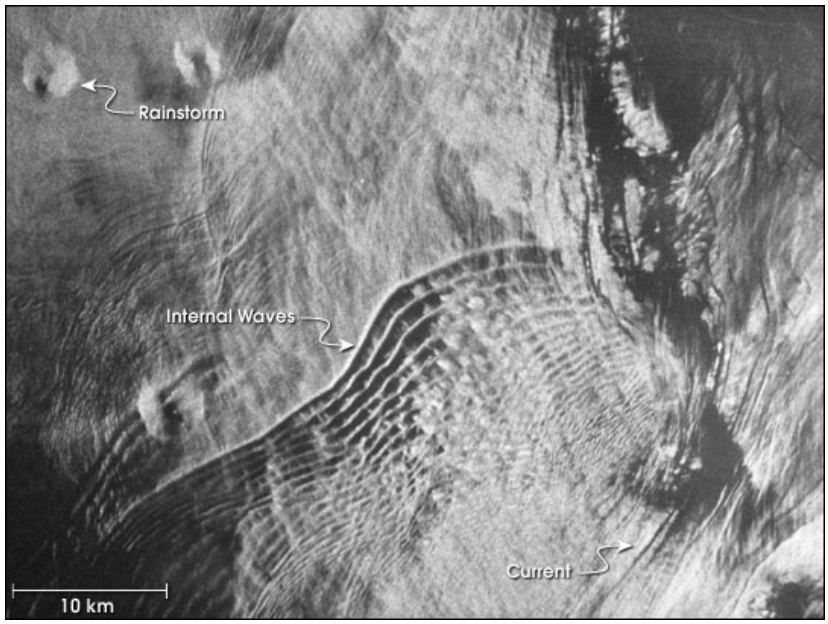

Figure 1.3: Internal waves in the Gulf of Mexico, northeast of the Yucatan Peninsula. Image obtained by synthetic aperture radar (SAR). From www.internalwaveatlas.com

theory and the fact that the aforementioned waves were non-dispersive waves, the nonlinear, solitary nature of NLIWs had been established (see also Section 1.1.2). With the technological advancement, remote sensing and satellite imaging revealed that packets of propagating NLIWs were a ubiquitous feature of the coastal oceans around the globe. Pictures of satellite images of internal waves are shown in Figures 1.3 and 1.4 .

A defining feature of a soliton is the intrinsic balance between nonlinearity and dispersion. If the wave is non-dispersive, nonlinear effects tend to steepen the wavefront until it reaches a shock-like state. On the other hand, in a dispersive system, the nonlinearity is balanced by the dispersion of the various Fourier components of the wave and this

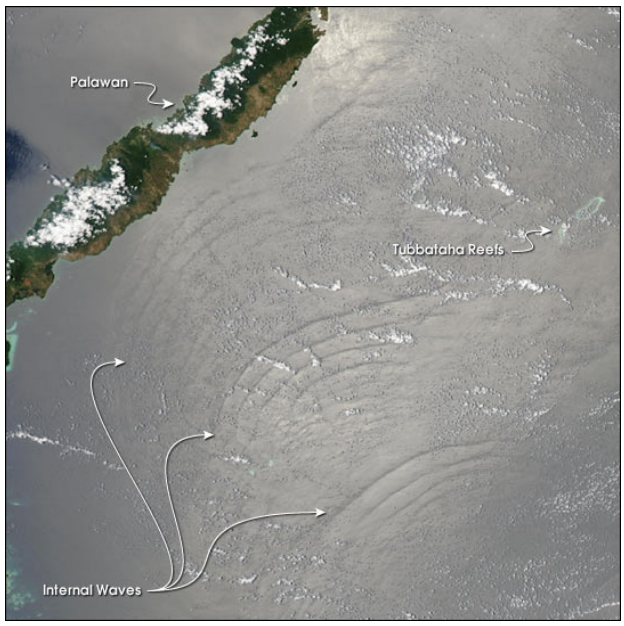

Figure 1.4: Internal waves in the Sulu Sea between Malaysia and Philippines. From www.internalwaveatlas.com

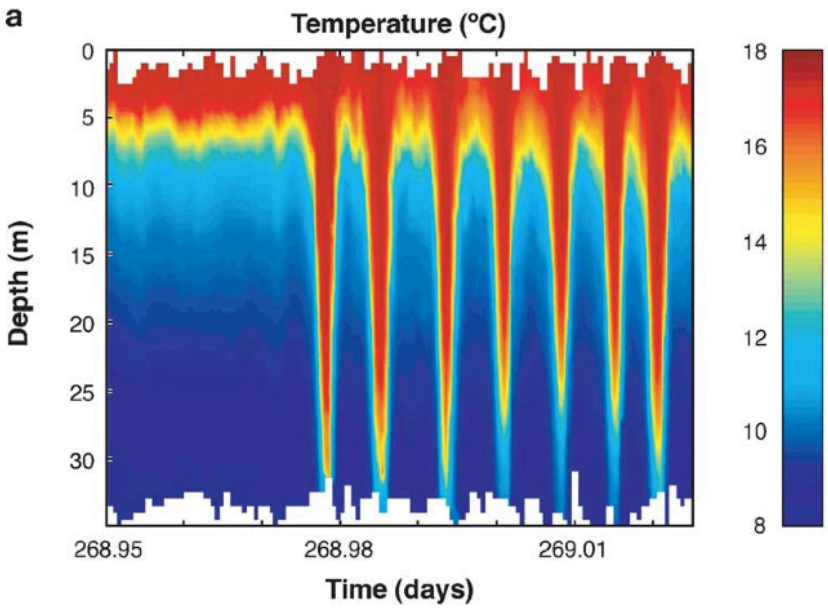

Figure 1.5: Large-amplitude internal waves observed with fixed thermistor arrays. The leading portion of a wave packet observed in about 147 m of water and propagating toward the Oregon coast. From Stanton & Ostrovsky [90].

equilibrium results in a permanent shape (soliton) that propagates at a speed which depends on the layer depths, the density difference and its amplitude. It is not uncommon instead of a single soliton, a train of solitons to be formed which is termed as nonlinear internal wave-trains.

Internal waves transfer energy, mass and nutrients over large distances [16] [87]. They are an important source of strong mixing through their breaking [42] but also through their interaction with the sea bed [12], which is the focus of this study. They can also affect biological processes through the mixing and resuspence of nutrients and through the redistribution of light and heat. They interfere with radar signals and underwater acoustics [5] and they can play a role in underwater navigation, while at the same time ocean drilling platforms are threatened by the forces internal waves can exert on them.

1.1.2 Internal Solitary Wave Theory

In the context of internal solitary waves, the equation that has played the most important role in the description of the waveform was the Korteweg-de Vries (KdV) equation (1.3), derived by Diederik Korteweg and Gustav de Vries in 1895 to initially describe free surface solitary waves in shallow waters since the air-sea interface can be seen as a density interface. This equation was not studied much until 1965 when it was discovered numerically that any initial condition seemed to asymptotically separate in time into a train of solitons [103] . In 1967 an analytic solution was found with the use of the inverse scattering method

[32] .

$$\eta_t + (c_0 + \alpha\eta)\ \eta_x + \beta\eta_{xxx} = 0 \tag{1.3}$$

The KdV equation is a good first order approximation to the observations of internal solitary waves but it is weakly nonlinear and has limitations to its use. It assumes that nonlinearity and dispersion are comparable and small and thus it can only capture small amplitude waves accurately. For this reason several variants of the KdV equation have been developed, one of the most important ones being the extended KdV (eKdV) equation which includes cubic nonlinearity [27] [35] [53] [59]:

$$\eta_t + (c_0 + \alpha_1\eta + a_2\eta^2)\ \eta_x + \beta\eta_{xxx} = 0 \tag{1.4}$$

Where η is the isopycnal (line of constant density) displacement, t is the time and x is the direction of propagation. The parameters α_1, α_2 and β are environmental parameters, while c_0 is the linear phase speed of the wave. Their values are given by the following relationships for a two-layer system with a rigid lid under the Boussinesq approximation:

$$c_0 = \sqrt{\frac{g\sigma h_1 h_2}{h_1 + h_2}} \tag{1.5}$$

$$\alpha_1 = \frac{3}{2}\ c_0\ \frac{h_1 - h_2}{h_1 h_2} \tag{1.6}$$

$$\alpha_2 = -\frac{3}{8}\, c_0\, \frac{(h_2 - h_1)^2 + 8h_1h_2}{(h_1h_2)^2} \tag{1.7}$$

$$\beta = \frac{c_0}{6}\, h_1h_2 \tag{1.8}$$

Where g is the gravitational acceleration, h_1 (h_2) is the upper (lower) mean layer thickness and σ is the mean density difference:

$$\sigma = \frac{2(\rho_2 - \rho_1)}{(\rho_1 + \rho_2)} \ll 1 \tag{1.9}$$

From equations (1.7) and (1.8) one can observe that the sign of the dispersion parameter β is always positive and that α_2 is always negative. The sign of α_1 can either be positive or negative and it defines the polarity of the wave. When $h_1 > h_2$ then the resulting wave is a wave of elevation, while a depression wave results when $h_1 < h_2$. Solutions to the eKdV equation (Eq. (1.4)) have been found by several researchers [53] [68] [77] and solitary waves take the form:

$$\eta = \frac{\eta_0}{b + (1 - b)\ cosh^2\gamma(x - ct)} \tag{1.10}$$

$$c = c_0 + \frac{\eta_0}{3}(\alpha_1 + \frac{1}{2}\alpha_2\eta_0), \qquad \gamma^2 = \frac{\eta_0(\alpha_1 + \frac{1}{2}\alpha_2\eta_0)}{12\beta}, \qquad b = \frac{-\eta_0\alpha_2}{2\alpha_1 + \alpha_2\eta_0} \tag{1.11}$$

Here η_0 is the wave amplitude, c is the nonlinear wave speed and b and γ are parameters.

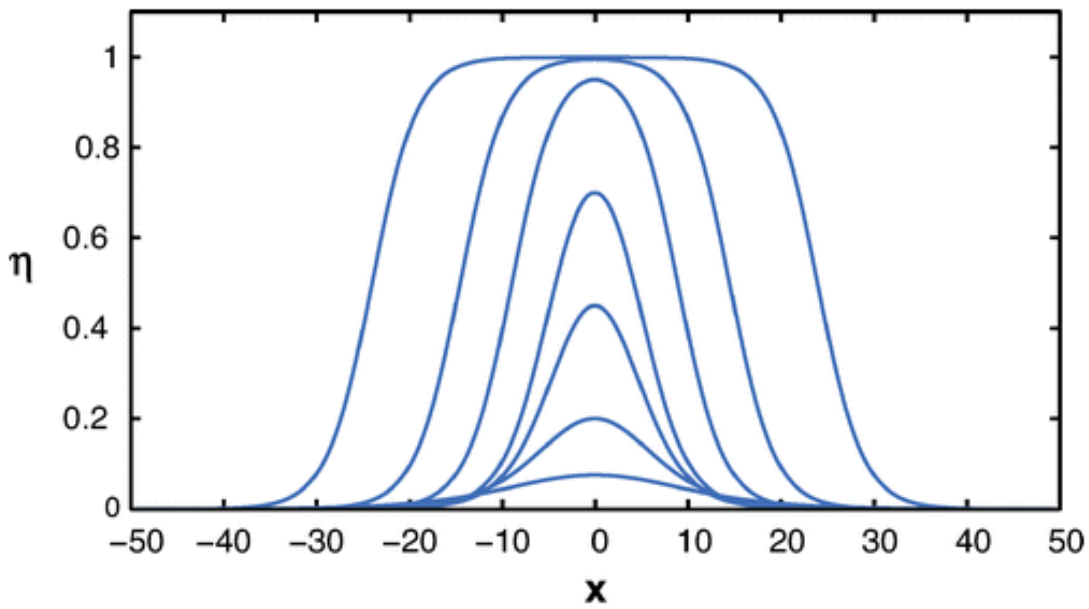

Figure 1.6: The broadening of the wave crest with increasing amplitude as results from the eKdV equation. From Helfrich & Melville [43].

Comparing the waveforms produced by the KdV equation with the ones that derive from the eKdV equation, one can observe that the eKdV captures the broadening of the wave crests as amplitude increases beyond a threshold value, below which the wavelength decreases (Figure 1.6). On the contrary, KdV waveforms become monotonically narrower as wave amplitude increases. The broadening of the wave crests with increasing amplitude agrees with observations extending as early as 1970s until now [40] [90]. The eKdV waves have a maximum wave amplitude above which the waves break due to excessive broadening and this wave amplitude is defined as the conjugate state limit [58].

Miyath and Choi & Camassa [20] extended the weakly nonlinear eKdV model for a two-layer stratification to include full nonlinearity,

while they retained only first-order approximation of the dispersion β. Their model is in agreement with the eKdV theory for $0.4 < h_1/(h_1+h_2) < 0.6$. This validity range was confirmed by laboratory experiments [66] [20] which also showed a very good agreement with the Miyath-Choi-Camassa (MCC) model for a wide range of layer depths. Nevertheless, it was found [51] that for sufficient wave amplitude the solitary waves could be unstable to small wavelength perturbations to Kelvin-Helmholtz instability, which poses a limitation to the use of the MCC model.

Many more models and modifications to the KdV equation have been proposed over the years in order to capture more accurately the NLIW waveform in a variety of cases such as when the earth's rotation is taken into account [36] [37], when the NLIW is propagating over a slowly varying topography [69] or the case of continuous stratification [63] [23] [98]. These models are beyond the scope of this study and the reader is referred at the review articles of Helfrich & Melville [43] or Apel et al. [5] for further information.

1.2 Benthic Excitation Under NLIWs

The bottom boundary layer in the coastal ocean and in lakes consists of the interface between the sediment-laden seabed and the overlying water column, an interface across which active exchange of particles, chemicals and organisms occurs [87]. In order for sediment resuspension to take place, according to the commonly accepted theory, the

speed of the background currents, such as tidal currents in oceans and seiche driven currents in lakes, above the benthic boundary layer should exceed a threshold value, above which the seabed shear stresses have sufficient strength to overcome the gravity forces [34]. The aforementioned mechanism of sediment resuspension is capable of stirring and dislodging material, but it is unclear whether it can transfer particles to significant height above the seabed. Such a question arises from the fact that the turbulent dynamics of this mechanism do not show any coherence in space and time thereby posing questions about its ability to lift sedimentary material to significant height above bottom.

Another possible mechanism for sediment resuspension and the one proposed in this study is through the interaction of NLIWs with the seafloor. This interaction is an ongoing research topic which has been stimulated by recent observations of resuspended material in the footprint of NLIWs [9] [11] [12] [81] [82] [83]. Bogucki was the first to report events of NLIW driven resuspension from data obtained during the Coastal Mixing and Optics 1996 (CMO '96) experiment off the coast of Massachusetts. Afterwards, other observations, numerical simulations and lab experiments gave more insight to this mechanism. A more detailed reference on these studies is made later. Figures 1.7 and 1.8 show observations of sediment resuspension under NLIWs.

The interaction of the NLIW with the bottom has several consequences on the wave itself, on the ecology and on the propagation of acoustical and optical signals. To begin with, through the generation of BBL turbulence, the NLIW dissipates its energy [72] and if the traveling

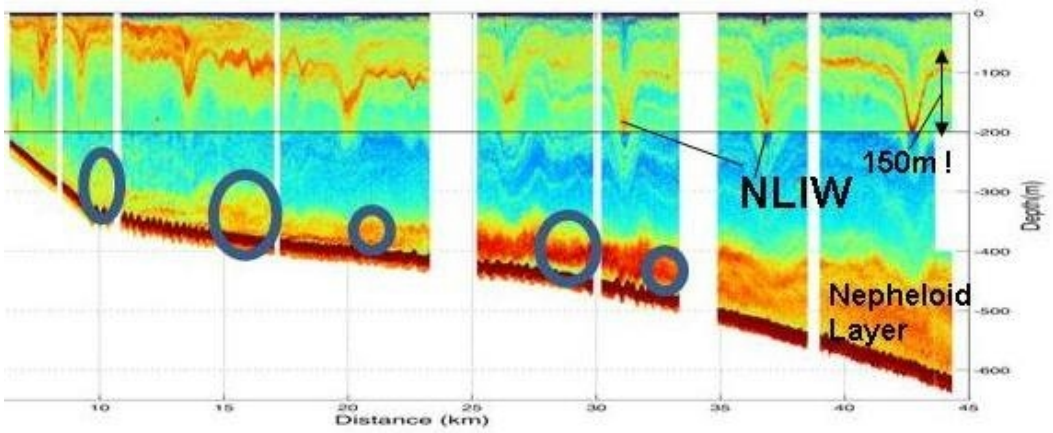

Figure 1.7: Acoustic backscatter image of successive transects of a NLIW propagating over a gently shoaling seabed. Sediment is resuspended and a nepheloid layer is formed in the wave footprint as well as 30 m high sand waves (indicated by circles). The picture is from the Northern South China Sea. Courtesy of Dr Ben Reeder.

distance of the wave is long, the excessive energy loss can lead to altering of the waveform. Furthermore, Stastna & Lamb [92] through their numerical simulations have shown that vortices ejected from the BBL deform the thermocline and ultimately change the NLIW waveform. On the ecological side, together with sediment resuspension, nutrients are also resuspended and in the case of NLIWs with trapped cores, these nutrients can be transported over long distances, which can have a direct impact on the biological productivity [16] [87]. Finally, resuspended sediment causes sound scattering and light attenuation, properties that are exploited by scientists to measure water turbidity [6].

The wave-induced currents drive bottom boundary layer (BBL) which develops both in space and in time and, in real circumstances, can interact with varying topography, background turbulence and back-

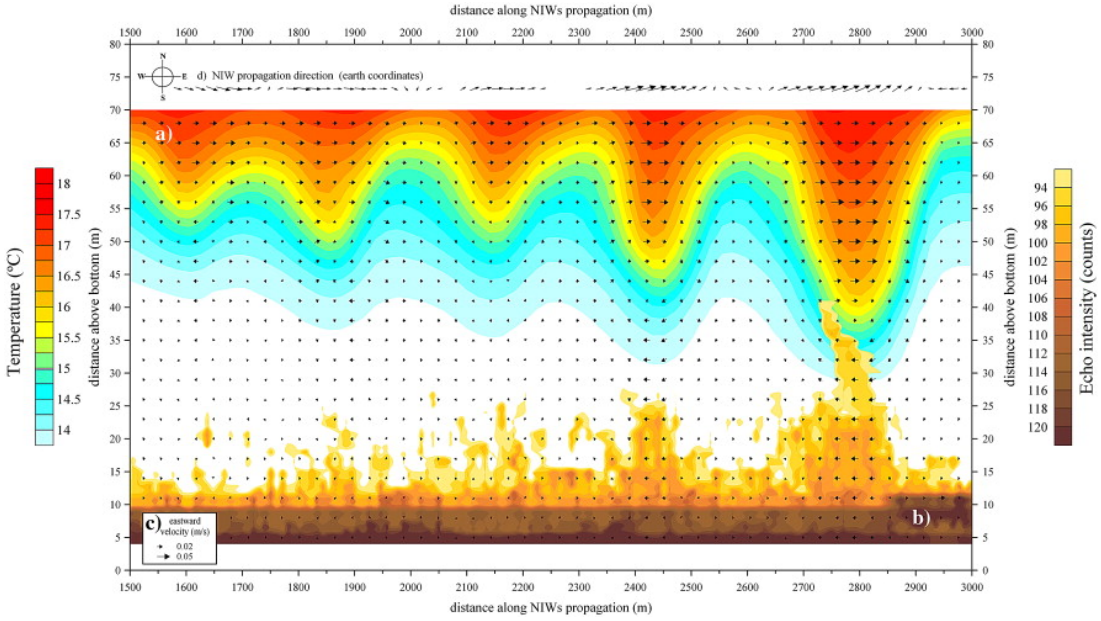

Figure 1.8: In-situ observations of the propagation of the first five NLIWs observed by Quaresma et al. [82] over the western Portuguese mid-shelf (2004). It is composed as an overlay of the following recorded series: a) temperature profile (C), obtained by the thermistors chains; b) 300 kHz ADCP echo intensity (in counts); c) 300 kHz ADCP eastward velocity (as vectors). d) Representation of the short-period current velocity vectors (observed near the surface) showing the propagation direction of each soliton.

ground currents. Furthermore, any variability of the wave velocity field in the along-wave propagation direction implies the existence of a variable pressure gradient impressed on the wave-induced boundary layer [26]. This pressure gradient is adverse under the decelerating part of the NLIW, causing the flow to separate if the adverse pressure gradient surpasses a threshold value. The resulting spatially and temporally varying separated flow is susceptible to self sustained instabilities which can give rise to coherent dynamics under certain environmental conditions.

The existence of a separated flow pocket implies the presence of an inflection point at the velocity profiles. This inflection point gives rise to an inviscid mechanism of shear instability. Hammond & Redekopp have shown that the growth rate of inviscid instability is significantly larger than the one that corresponds to a viscous mechanism [41] (i.e. Tollmien-Schlichting waves). They have further proved that the inviscid instability in shear layers can potentially become of absolute type, while the viscous instability in attached boundary layers is always convective [41]. The absolutely unstable character of the inflectional profile caused by the separation of the BBL may spontaneously give rise to global instability. Global instability is a threshold phenomenon: with decreasing wave amplitude, the growth rate becomes exponentially small. The global instability has a well-defined frequency that leads to spatiotemporally coherent dynamics [21]. These dynamics in the case of a bottom boundary layer will take the form of instabilities in the vorticity field which will later rollup into coherent vortices and travel away from the boundary due to the existence of an image vortex below the bottom boundary. NLIW-induced BBL will present an inflection point caused by the existence of a separated flow, and given the fact that the NLIW- induced BBL has a spatiotemporal dependence, it is susceptible to global instability. The basics of absolute, convective and global instability can be found in Section 1.4.

The benthic excitation under propagating NLIWs should be distinguished from the breaking of NLIWs on steep slopes and the vortex shedding due to abrupt steepening of breaking wave or the formation of internal boluses that ascend up the slope [8] [42], and mixing that fol-

lows. NLIW breaking on steep slopes is a different active area of research and it is a phenomenon which is experimentally studied by Helfrich [42] and Boegman & Ivey [8] among others. Recent numerical simulations have been performed by Venayagamoorthy & Fringer [99], while observations have been made by Leichter et al. [61]. The interested reader is referred to the aforementioned studies for further information.

1.2.1 Observations

Apart from observations of NLIW isopycnal structure, during the last 15 years scientists are also interested in the record of characteristics of these waves such as the velocity wavefield, the pressure field induced by the internal waves and the study of the wave-induced BBL. The instruments that are typically used in the relevant field measurements are a combination of Acoustic Doppler Current Profilers (ADCP), which can measure the particle velocity across the water column, vertical thermistor chains, optical tripods, which measure light attenuation which can be related to particle loading, and echosounders. By making the aforementioned measurements, mixing, particulate resuspension and energy transfer and dissipation due to internal waves can be quantified.

Bogucki et al. [9] were the first to observe sediment resuspension under waves of elevation on the California shelf. They observed flow reversal and boundary layer separation under the wave and they hypothesized that the adverse pressure gradient (APG) underneath the wave causes flow reversal, suggesting that the NLIW acts as a "bot-

tom pump", raising and stirring sediment on its passage. Moum et al. [74] made observations of waves of depression over the Oregon's continental shelf and saw Kelvin-Helmholtz like billows and turbulence at the density interface caused by the passage of the internal wave, which also altered its waveform. Klymak & Moum [55] observed a sequence of three internal solitary waves of elevation propagating over Oregon's shoaling shelf. They were able to capture increased suspended sediments in the BBL and they also saw a trapped core in the leading wave. Scotti & Pineda [86] also reported trapped cores under nonlinear and steep waves of elevation off the coast of Massachusetts. Moum & Smyth [71] calculated, after a theoretical decomposition, the bottom pressure field by measuring the velocity wavefield. Moum & Nash [75] measurements of wave-induced bottom pressure over New Jersey's continental shelf confirmed theoretical predictions using near-bottom velocity fields [71]. Bogucki et al. [12] presented several examples of sediment resuspension at the footprint of mode-1 and mode-2 NLIWs of both polarities during the CMO 96 experiment and associated them with BBL global instability. They also observed high turbidity levels (high levels of beam-C attenuation), while horizontal velocity timeseries showed BBL separation in the rear of the wave for waves of depression and underneath the wave for elevation waves by measuring negative horizontal velocities close to the bottom and positive ones further up at the same streamwise location. In addition, vertical velocity timeseries proved the existence of coherent vortices by measuring rapidly interchanging sign of vertical velocities close to the seafloor. Later, Bogucki & Redekopp [11] claimed that the occurrence of NLIWs and the benthic excitation that they in-

duce present a repetitive pattern or "climate cycle" of NLIW dynamics. Moum et al. [73] in their attempt to quantify energy transport by NLIWs, were not able to measure the dissipative losses inside the BBL. At their later study, Moum et al. [72] approximated the dissipative losses inside the BBL using measurements of the velocity and a wall friction law.

The paucity of observational data on the NLIW-induced BBL coupled with the limited spatio-temporal resolution of associated instrumentation data resolving the flow structure render imperative the need for controlled simulations and experiments to further investigate the flow structure and energetics of this BBL. Not only would such simulations/experiments help interpret field data and guide future deployments, they would provide critical information towards reliable energy budget closures.

1.2.2 Previous Numerical Studies

Bogucki & Redekopp [10] and Wang & Redekopp [100] considered the case of a weakly nonlinear wave of elevation propagating against an oncoming current with a linear profile in a two-layered stratified environment, such that the wave is almost stationary for the timescale of instability evolution. From their 2D Direct Numerical Simulation (DNS) they observed a spontaneous onset of a global BBL instability, which is intrinsic to the separation bubble, to appear when the wave amplitude surpassed a threshold value. The separation bubble was fragmented into a train of coherent vortices (their scale commensurate with

the fundamental horizontal wavelength of the global instability) which were ejected into the water column and were advected with the flow. Stastna & Lamb [92] used a fully nonlinear wave of elevation propagating contrary to an oncoming barotropic current in a continuously stratified fluid. They also observed global instability in the adverse pressure gradient region and subsequent vortex shedding away from the bottom boundary. The vortices in that case deformed the thermocline and altered the waveform. They did not observe any instabilities in the absence of a current or when the current had the same direction with the propagating wave. All these numerical simulations were focused on waves of elevation.

Diamessis & Redekopp [26] were the first to consider waves of depression (and waves of elevation as well). They used weakly nonlinear KdV waves propagating over a flat bottom without any background current. They showed that global instability can occur in the adverse pressure gradient region of the wave-induced bottom boundary layer in the rear of the wave instead of the front, which is the case with waves of elevation, when the wave amplitude exceeds a critical value. They also found that the near-bed vertical velocities were comparable to the wave phase speed, while the bottom shear stresses were found to scale with boundary layer length scales. Moreover, the critical wave amplitude above which instability occurs was found to decrease with increasing Reynolds number for a fixed layer thickness ratio. Finally, the maximum vortex ejection height in their simulations reached values corresponding to 30% - 35% of the depth of the computational domain. However, the weakly nonlinear waves they used with artificially large maximum

wave amplitudes were not representative of the NLIWs observed in the real ocean but given the highly accurate numerical scheme they applied, their results gave a qualitative insight to the problem of wave-induced benthic excitation and serve as the snapboard of the current study. Figure 1.9 shows BBL vortex shedding under weakly nonlinear waves of depression in the rear of the wave from the simulations of Diamessis & Redekopp [26]. Finally, Stastna & Lamb [93], using a fully nonlinear wave of elevation showed that the the onset of BBL instability is a strong function of the background current. They also studied the Lagrangian transport of passive particles due to BBL instability and they found that while particles are lifted to some degree by the wave-induced currents as the pass over the NLIW body, the BBL vortex shedding facilitates the transport of particles to much larger heights.

1.2.3 Laboratory Experiments

Laboratory experiments in the recent years have investigated the internal waveform evolution and wave breaking over shoaling and ridge-like topography [8] [39] [42] [67] [94]. In their first laboratory attempt to observe global instability in the wave-induced BBL, under solitary waves of depression propagating over a flat bottom in a quiescent fluid, Carr & Davies [17] were unsuccessful because for the maximum Reynolds number examined with their experiments, the wave amplitudes above which global instability could occur were above the conjugate state limit. Nevertheless, they were able to observe boundary layer separation as predicted by Diamessis & Redekopp [26] and were able to measure near-

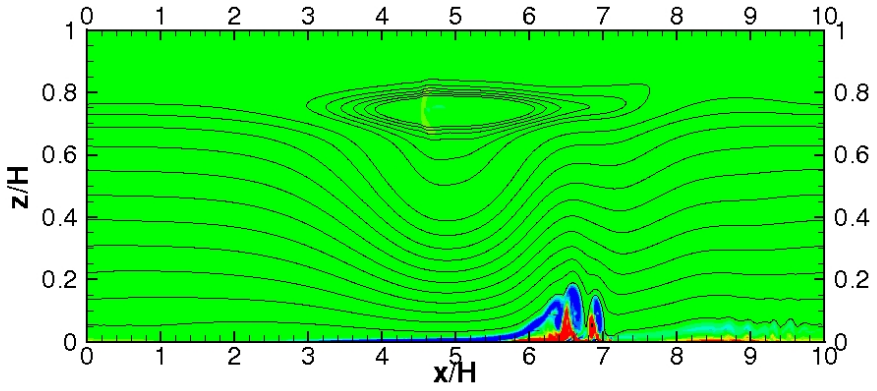

(a)

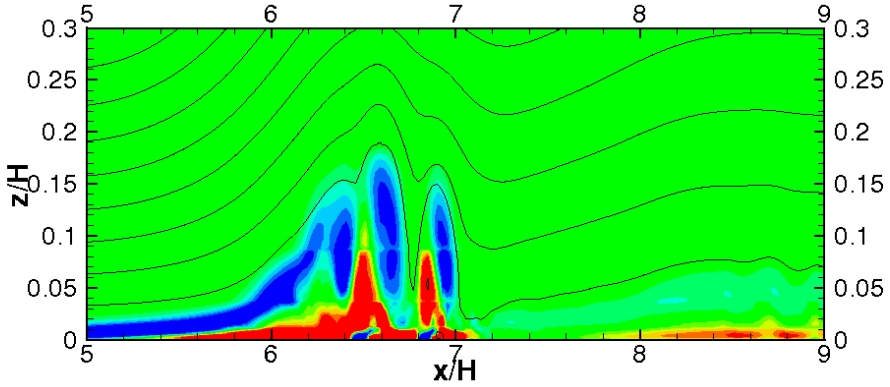

(b)

Figure 1.9: Weakly nonlinear internal waves and BBL vortex shedding from numerical simulations of Diamessis & Redekopp [26]. Black line contours: total density isopycnals; colored contours: perturbation vorticity (red and blue positive and negative vorticity, respectively). Both plots are sampled at $tC_0/H = 5$ from supercritical amplitude ($\alpha_0 = 0.55$) mode-1 wave of depression simulation at $Re_W = 2 \times 10^4$. The wave propagates from right to left. The entire computational domain is shown. Global instability was observed at approximately $tC_0/H = 4$ (a) ; (b) enlarged view of separation bubble in (a).

bed horizontal velocities induced by the internal wave. They also found that the vertical extent of the flow reversal was approximately 8% of the depth of the entire water column. In a subsequent study, Carr et al. [19] using similar experimental setup achieved greater values of wave Reynolds number as well as increased wave amplitudes by changing the experimental geometry and enhancing the stratification, thus allowing them to record BBL instabilities and subsequent vortex shedding in the wave footprint as a manifestation of global instability. Their results, despite the good qualitative agreement with those of Diamessis & Redekopp [26], had quantitative discrepancies which could be attributed to the fact that Diamessis & Redekopp used weakly nonlinear forcing, whereas in the experimental study, the waves were highly nonlinear. Finally laboratory experiments by Carr & Davies [18] under NLIWs of elevation showed no evidence of flow separation and vortex shedding, contrary to speculations of Diamessis & Redekopp who were motivated by the presence of an adverse pressure gradient in the leading edge of the wave.

NLIWs shoaling on non-flat beds have also been explored. Boegman & Ivey [8] studied experimentally the structure and dynamics of the turbulent BBL of NLIWs shoaling over a steeply sloping bottom and observed steepening of the rear of the wave because of the adverse pressure gradient due to rapidly changing slope, flow separation and near-bottom vortices suspending bed material. Aghsaee et al. [1] in a recent numerical investigation of shoaling NLIWs over sloping topography have found that for steep slopes ($S \geq 0.1$) three types of NLIW breaking are possible: plunging, collapsing and surging and they computed the in-

ternal Irribaren number, which is the ratio of the topographical slope over the wave slope, and controls the type of breaking. They also observed that for mild slopes ($S \leq 0.05$) the wave would reverse polarity. Last but not least, high Reynolds numbers ($Re_w \sim 10^4$) were found to trigger global instability which modified the breaking process. Shoaling of NLIWs on non-flat beds is not the focus of the current study.

1.3 Boundary Layer Separation Basics

In a decelerating stream, where the pressure gradient is adverse, the boundary layer has a point of inflection. The existence of this inflectional point implies that if the adverse pressure gradient is strong enough, the flow next to the boundary will reverse direction and a backward flow will result. This reversed flow meets the forward flow at a point upstream where the fluid near the boundary is transported out into the free-stream [57]. Then we say that the flow separates (Figure 1.10). At the separation point the shear stress is zero:

$$\tau_b = \left(\frac{\partial u}{\partial z}\right)_b = 0 \tag{1.12}$$

Where τ is the shear stress, u is the streamwise component of the velocity and z is the vertical to the boundary direction.

The streamline that intersects with the boundary is the dividing streamline and the intersection point is the detaching point. After the boundary layer undergoes transition to turbulence, the dividing stream-

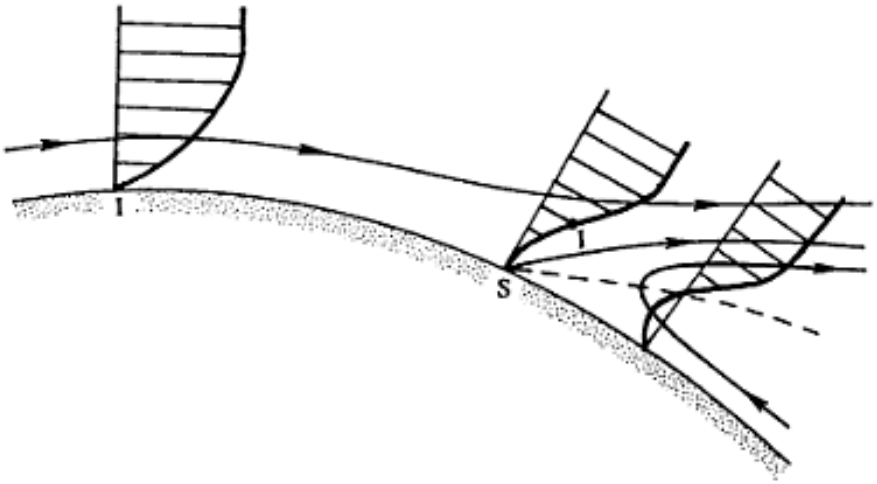

Figure 1.10: Streamlines and velocity profiles near a separation point S. Point of inflection is indicated by I. The dashed line represents $u = 0$. From Kundu [57] .

line reattaches to the boundary at the reattachment point. The separated region, which is called separation bubble, contains a large vortex of recirculating fluid. An illustrative example can be found in Figure 1.11. The length of the separation bubble decreases with increasing strength of adverse pressure gradient for a given adverse pressure gradient lengthscale [95]. If the adverse pressure gradient is strong enough, then the separation bubble becomes unsteady and a periodic shedding of cross-stream vortices is observed which do not seem to be affected by the boundary [79]. The vortex shedding frequency may be predicted by a linear stability analysis of a shear layer in the absence of a boundary.

If one considers a shear layer between two streams with velocities u_1 and u_2, the velocity difference is $\Delta u = u_2 - u_1$, the mean velocity is $\bar{u} = \frac{1}{2}(u_1 + u_2)$, the vorticity thickness is $\delta_\omega = \Delta u/(\partial u/\partial z)_{max}$ and the velocity ratio is $\lambda = \Delta u/(2\bar{u})$. Then according to Monkewitz & Huerre [70] the

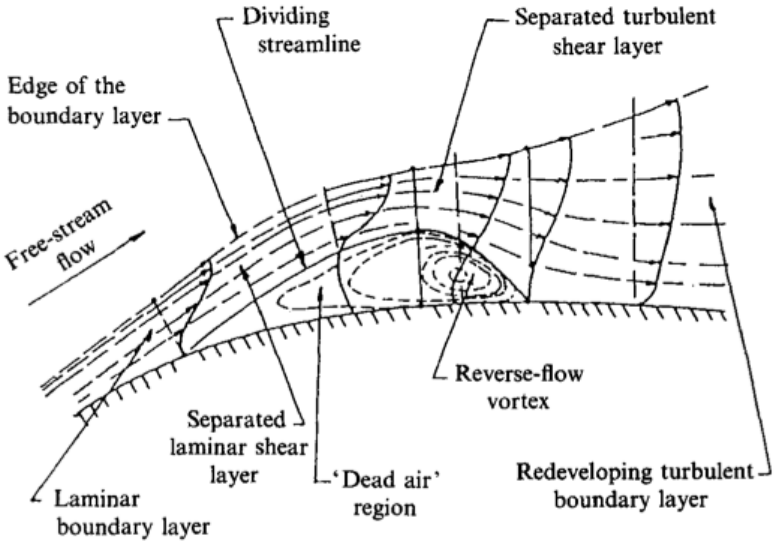

Figure 1.11: The flow field in the vicinity of a transitional separation bubble. From Horton [46] .

nondimensional frequency is:

$$\omega^* = \frac{1}{4}\delta_\omega \frac{2\pi f}{\bar{u}} \tag{1.13}$$

Inviscid (linear) analysis of parallel shear flows predicts that the most amplified frequency for a hyperbolic tangent velocity profile is $\omega^* = 0.21$, so it is reasonable to expect a shedding frequency $\omega^* = 0.21$ inside the separation bubble.The previous stability analysis holds for a free shear layer in parallel background flow. However, separated flow inside a boundary layer differs from that in the sense that there is streamwise dependence of the velocity profile and a boundary is present close to the inflection point. More information about the stability analysis of separation bubbles can be found in the paper of Hammond & Redekopp [41].

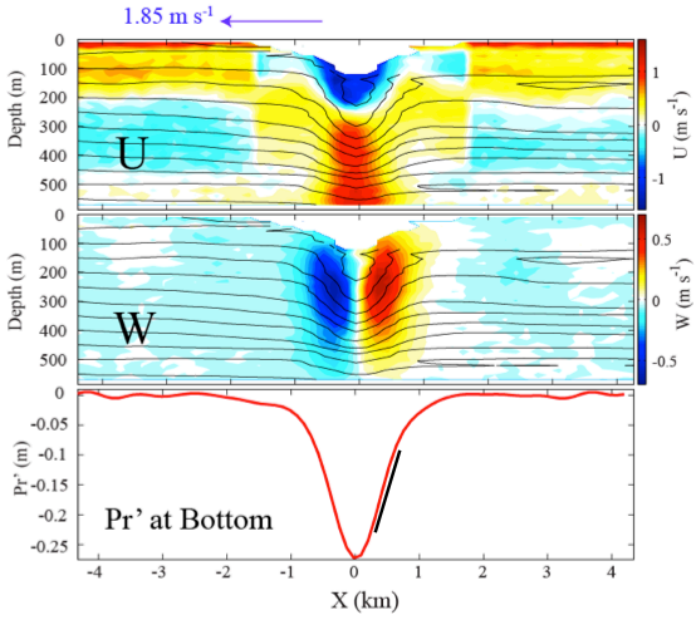

Figure 1.12: NLIW velocity and bottom pressure fields in the South China Sea. Courtesy of Dr Ren-Chieh Lien

In situ measurements have shown the existence of adverse bottom pressure gradients in the rear of a NLIW of depression accompanied with flow separation, high near-bed vertical velocities and high levels of turbidity [12]. Thus, if the aforementioned adverse pressure gradient is of sufficient strength, one would expect flow separation and possible vortex shedding. Measurements of the velocity and bottom pressure fields under a NLIW [75] may be found in Figure 1.12.

It is important at this point to clarify that in the present study the focus will be on separation of laminar boundary layers which can be significantly different from the separation of turbulent boundary layers that are not considered here. The interested reader can look for more information about turbulent boundary layer separation at the review article by Simpson [88].

1.4 Linear Instability Basic Definitions

In the previous sections, reference was made to the concept of instability. In the present section, an effort is made to provide the definitions for *convective*, *absolute*, *local* and *global instability*. Local/global and absolute/convective instability concepts provide the necessary theoretical framework to classify different open shear flows according to the qualitative nature of their dynamical behavior [47].

To begin with, the terms *"local"* and *"global"* refer to the instability of the local velocity profile (at one point) and of the entire flow field, respectively [47]. Local instability can further be distinguished between *"convective"* and *"absolute"* according to the impulse response of the system within the parallel flow approximation (no spatial variation) at each streamwise station. If localized disturbances spread upstream and downstream and contaminate the entire parallel flow, the velocity profile is said to be *locally absolutely unstable* [47]. If the disturbances are swept away from the source, the profile is said to be *locally convectively unstable* [47].

A more formal definition can be given as such: If $G(x,t) = \phi(x,t)\ e^{i(kx-\omega t)}$ is a disturbance which is inserted at t=0 into the flow, then the flow is said to be linearly *stable* if

$$\lim_{t\to\infty} G(x,t) = 0 \quad \text{along all rays x/t = constant} \tag{1.14}$$

and it is linearly *unstable* if

$$\lim_{t\to\infty} G(x,t) = \infty \quad \text{along at least one ray x/t = constant} \tag{1.15}$$

Among the linearly unstable flows further distinction can be made between the impulse response of the basic flow. A flow is *convectively unstable* if

$$\lim_{t\to\infty} G(x,t) = 0 \quad \text{along the ray x/t = 0} \tag{1.16}$$

and it is *absolutely unstable* if

$$\lim_{t\to\infty} G(x,t) = \infty \quad \text{along the ray x/t = 0} \tag{1.17}$$

Figure 1.13 offers a schematic of the aforementioned definitions. It is now clear that a flow is locally linearly unstable if the maximum growth rate of the instability is greater than zero and if it is less than zero, it is locally linearly stable. Furthermore, the distinction between absolute and convective instability depends upon the *absolute growth rate*, which is the growth rate of the wavenumber k_0 along the ray $x/t = 0$. If it is greater than zero, then the instability is characterized as absolute, otherwise the instability is convective. This complex wavenumber k_0 has by definition zero group velocity:

$$\frac{\partial\omega}{\partial k}(k_0) = 0 \tag{1.18}$$

So far the assumption has been that the base flow shows no spa-

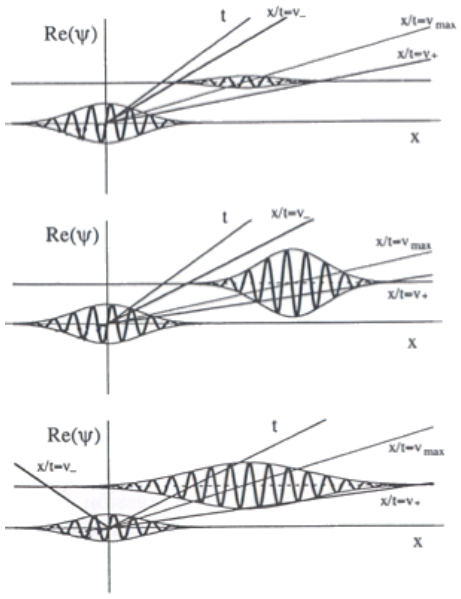

Figure 1.13: Linear response $\psi(x,t)$ to a localized initial state $\psi(x,0)$ of (top) stable flow, (middle) convectively unstable flow, (bottom) absolutely unstable flow. From Huerre & Rossi [48].

tial dependence on the x-direction. In many cases though, including wakes or boundary layers, this assumption is invalid since there is spatial variation of the flow. Spatially varying flows have wavenumbers and frequencies that are x-location dependent. These flows can be distinguished in the following four categories:

If the maximum growth rate $\omega_{i,max}$, which is now a function of x-position, is negative and consequently the local absolute frequency $\omega_{0,i}$, based on the local profile at given x-position, is negative, then the flow is *locally stable uniformly*. If the maximum growth rate is positive but the local absolute frequency is negative, then there is a region of local convective instability and the flow is *locally convectively unstable*. Flows that fall into the aforementioned categories act as external noise

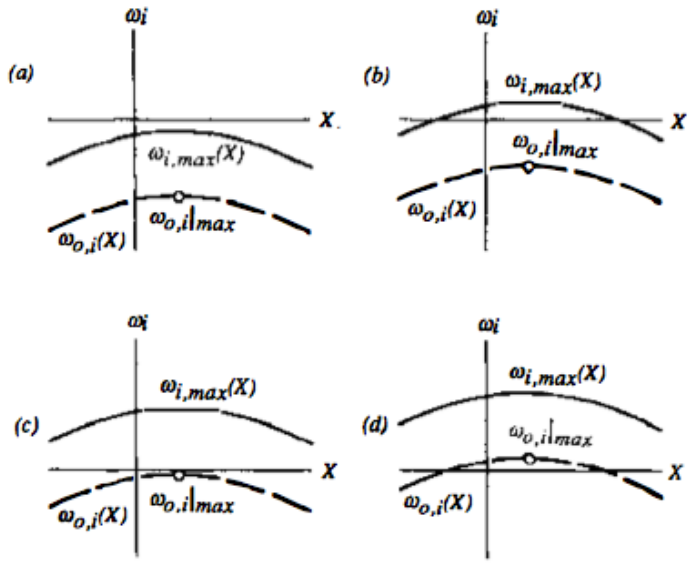

Figure 1.14: Classes of spatially developing flows according to the nature of the local instability. (a) uniformly stable; (b) convectively unstable; (c) almost absolutely unstable; (d) pocket of absolute instability. Here $\omega_{i,max}$ is the maximum growth rate, $\omega_{0,i}$ is the local absolute growth rate and $\omega_{0,i|max}$ is the maximum value of the local absolute growth rate. From Huerre & Monkewitz [47].

amplifiers. They are *globally stable* in the sense that no self-sustained resonant states may arise [47]. The third category consists of the flows which have positive maximum growth rate and the absolute growth rate is negative but vary small. These flows are *almost absolutely unstable* and can admit weakly damped global modes, so they are *marginally globally stable*. Global modes are modes of instability, where all the particles of the medium oscillate with the same frequency and in phase. Global modes have the form $\psi(x,t,X) = \phi(x;X)e^{-i\omega_G t}$ where $\phi(x;X)$ is the x-eigenfunction and X is a slowly varying space scale. The non-existence of an x-eigenfunction in the spatially invariant flows was the reason for not taking into account global modes in the local stability analy-

sis. Continuing with the classification of the spatially varying flows, the fourth category comprises of the flows with positive maximum growth rate and positive local absolute frequency. In this case a *local absolute instability* prevails in a finite streamwise length. Such flows may exhibit self-excited *global modes* at specific complex frequencies ω_G and are defined as *globally unstable*. Figure 1.14 illustrates the maximum growth rate and the local absolute frequency for the four categories of flows.

1.5 Objectives

The objectives of this study are centered around further elucidating the transition to primary global instability and subsequent 2-D evolution of the BBL that forms under NLIWs in uniform depth water and flat topography. They may be formulated as:

1. Extend the work of Diamessis & Redekopp [26] to use fully nonlinear waves of depression with a partial investigation of elevation waves.
2. Determine the impact of Reynolds number, wave amplitude, oncoming current strength and layer thickness ratio on the wave-induced BBL. By doing so, a stability boundary diagram (hopf bifurcation) can be created.
3. Provide a quantitative and qualitative description of the wave-induced BBL.
4. Assess the dependence of wave-induced BBL evolution on upstream BBL characteristics and potential forms of external noise.

5. Compare with previous laboratory and numerical studies to provide a uniform framework for the mechanism driving the instability in NLIW-induced BBLs.

CHAPTER 2

SIMULATION AND PROBLEM CONFIGURATION

2.1 Problem Geometry: Domain Configuration, Wave Forcing and Oncoming Current Set-Up

Figure 2.1 shows the base flow geometry corresponding to a fixed NLIW of depression propagating over a flat bottom in uniform-depth two-layer stratification contrary to an oncoming barotropic current. The choice of a fixed wave is justified by the fact that energy losses due to bottom friction, which is the only sink of energy in our system, are expected to be small during the simulation in order to alter the waveform. The computational domain is periodic in the horizontal with free slip at the top and no slip at the bottom boundary conditions. The simulations are performed in a moving frame of reference with the relative wave phase speed $C_{ph} + U_{C|max}$. This choice is made because it allows us to run the simulations for longer time without sacrificing resolution in the horizontal. Our simulations may be regarded as a "temporal" simulation. In contrast, a "spatially evolving" simulation would require much longer domain.

The barotropic current is kept fixed in time and is designed as such to provide strong shear, localized near the bed. It is given by Eq. 2.1. (Note that the presence of a barotropic current does not alter the wave form as predicted by the method obtained in appendices A & B.)

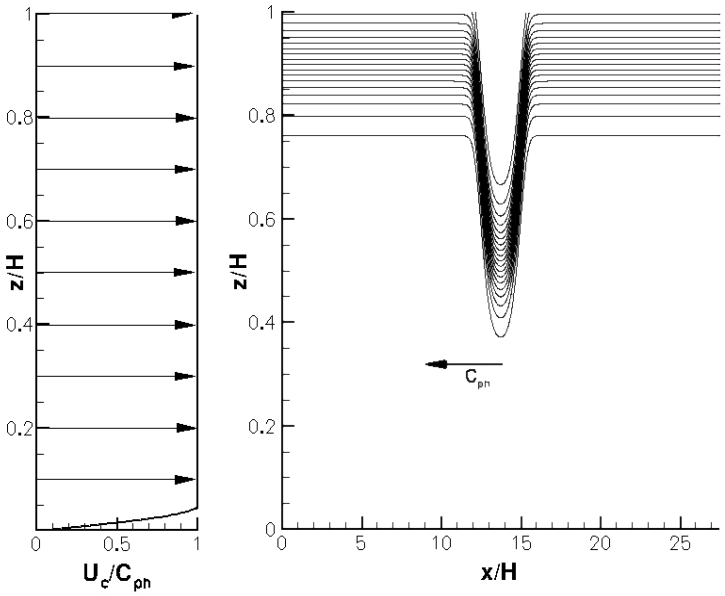

Figure 2.1: Schematic of the basic setup: NLIW of depression propagating contrary to an oncoming barotropic current. The current's shear layer has a height equivalent to 5% of the wave-guide depth. The simulation is on a moving frame of reference with the wave phase speed. The black lines are the isopycnals.

$$U_c(z) = \alpha_c \; C_{ph} \sin\left(\frac{z}{z_0}\frac{\pi}{2}\right) \quad \text{for } z < z_0 \; ; \quad \text{else} \quad U_c(z) = \alpha_c \; C_{ph} \tag{2.1}$$

Where α_c is a constant that defines the strength of the current and z_0 defines the vertical extent of the sheared region due to the current. In our simulations z_0 has a value corresponding to 5% of the wave-guide depth. This profile, even though it is not representative of a real oceanic boundary layer profile, serves as a sufficient approximation. This choice for the profile was based on two criteria: 1) to introduce additional shear into the wave-induced BBL and 2) the profile function and

its first derivative to be continuous and smooth at $z = z_0$, a constraint imposed by the spectral method which cannot handle discontinuities and very sharp gradients, unless explicitly formulated into the penalty scheme [25].

In the present study the NLIW waveform (the function representing the displacement of the thermocline) is taken from the steady state solution of a full range, cubic approximation with nonlinear dispersion evolution model (KdV3Nβ_c) derived by Sakai & Redekopp [85] who used cubic order polynomial fit to the fully-nonlinear phase speed of the wave and corrected the value of the dispersion parameter β by using the local layer depths at each location along the wave instead of their fixed background values and by replacing the linear constant wave phase speed by its nonlinear amplitude-dependent expression (see also Appendix A). The equations are available in Appendix A. The KdV3Nβ_c model is in very good agreement with the MCC model for a wide range of wave amplitudes while at the same time it is much less computationally time demanding.

Four steady-state solutions of the aforementioned higher order KdV equation are shown in Figure 2.2 and represent the NLIW waveforms. Only half waveforms are plotted, as they are symmetric around $x = 0$. One can observe that for the same layer thickness ratio, the wave trough becomes flatter as the maximum displacement increases. Moreover, the maximum wave amplitude for which a steady state solution can be reached increases with decreasing layer thickness ratio.

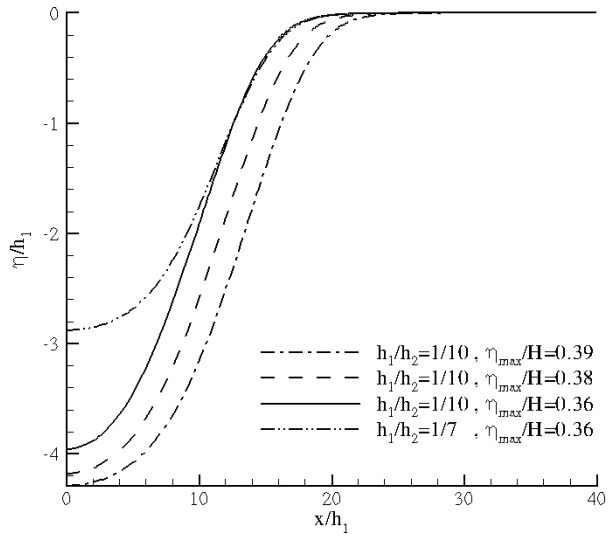

Figure 2.2: Four NLIW waveforms (functions of thermocline displacement) obtained by the steady-state solution of a full-range, cubic approximation with nonlinear dispersion, higher order KdV equation.

2.2 Governing Equations

The governing equations are the Navier-Stokes equations under the Boussinesq approximation [102, 25]:

$$\frac{\partial \mathbf{u}}{\partial t} = \underbrace{-\frac{1}{2}[\mathbf{u}\cdot\nabla\mathbf{u} + \nabla(\mathbf{u}\cdot\mathbf{u})] + \mathbf{F}_g}_{\mathbf{N}(\mathbf{u})} - \frac{1}{\rho_0}\nabla p' + \nu \underbrace{\nabla^2\mathbf{u}}_{\mathbf{L}(\mathbf{u})} - F_w^{\mathbf{u}} \quad , \tag{2.2}$$

$$\frac{\partial \rho'}{\partial t} = -\nabla\cdot(\mathbf{u}(\rho' + \overline{\rho}(z))) + \kappa\nabla^2(\rho' + \overline{\rho}(z)) - F_w^{\rho} \quad , \tag{2.3}$$

$$\nabla\cdot\mathbf{u} = 0. \tag{2.4}$$

$$\text{where} \qquad \mathbf{F}_g = -g\frac{\rho'}{\rho_0}\hat{\mathbf{k}} \quad . \tag{2.5}$$

The non-linear term in the momentum equations (2.2) is written in the skew-symmetric form to minimize aliasing effects in the numerical solution [24]. In addition, for the purpose of time advancement of the discrete equations (2.2), the buoyancy term has been absorbed into $\mathbf{N}(\mathbf{u})$. The quantities p' and ρ' are the perturbations of the pressure and density from their respective (mean) reference values which are in hydrostatic balance [25].

The forcing terms $F_w^{\mathbf{u}}$ and F_w^{ρ} appearing in the equations are determined by employing a particular decomposition of the fields for the velocity and the state variables, in a moving frame of reference, into a wave and perturbation component. The disturbance velocity field $(\tilde{u}, \tilde{w})$ forced by the wave-induced boundary layer is measured relative to the specified wave field (u_w, w_w) and the mean current $(C_{ph} + U_c(z))$, where $U_c(z)$ is the background shear flow satisfying, in general, the condition $U_c(0) = 0$. The disturbance fields $(\tilde{\rho}, \tilde{p})$ for the density and pressure are measured relative to the hydrostatically-balanced base state plus the fields (ρ_w, p_w) associated with the prescribed wave. Hence, the dependent variables appearing in the governing equations are decomposed into the following parts:

$$(u, w, p', \rho') = (u_w + C_{ph} + U_c(z) + \tilde{u}, w_w + \tilde{w}, \tilde{p}_w + \tilde{\tilde{p}}, \tilde{\rho_w} + \tilde{\tilde{\rho}}). \tag{2.6}$$

Note that all wave fields $(u_w, w_w, \tilde{\rho}_w, \tilde{p}_w)$ are chosen as steady in time because of the particular frame of reference selected for the computational problem. Also, the specific expressions for these wave fields that were used in providing the wave forcing for the simulations described later are defined in Appendix B. The pressure and density disturbance fields $(\tilde{\tilde{p}}, \tilde{\tilde{\rho}})$ are measured relative to the hydrostatically-balanced base state

plus those disturbances $(\tilde{p}_w, \tilde{\rho}_w)$ consistent with the specified permanent wave. Substituting (2.6) into the system (2.2)-(2.4) yields the modified form of the Navier-Stokes equations:

$$\frac{\partial \tilde{\mathbf{u}}}{\partial t} + \mathcal{A}(\tilde{\mathbf{u}}) + \tilde{\mathbf{u}} \cdot \nabla \mathbf{u_w} + \tilde{w} \frac{\partial U_c(z)}{\partial z} \hat{\mathbf{i}} = \mathbf{N}(\tilde{\mathbf{u}}) - \frac{1}{\rho_0} \nabla \tilde{\tilde{p}} + \nu \mathbf{L}(\tilde{\mathbf{u}}) \quad , \tag{2.7}$$

$$\frac{\partial \tilde{\tilde{\rho}}}{\partial t} + \mathcal{A}(\tilde{\tilde{\rho}}) + \tilde{\mathbf{u}} \cdot \nabla \tilde{\rho_w} = -\nabla \cdot (\tilde{\mathbf{u}}(\tilde{\tilde{\rho}} + \overline{\rho}(z))) + \kappa \nabla^2 (\tilde{\tilde{\rho}} + \overline{\rho}(z)) \quad , \tag{2.8}$$

$$\nabla \cdot \tilde{\mathbf{u}} = 0. \tag{2.9}$$

The advective operator $\mathcal{A}$ is defined as

$$\mathcal{A} \equiv (C_{ph} + U_c(z) + u_w) \frac{\partial}{\partial x} + w_w \frac{\partial}{\partial z} \quad . \tag{2.10}$$

Note that satisfaction of the solenoidal character of the wave velocity field has been taken into account. In addition, no wave forcing terms appear in equations (2.7) and (2.8) on account of the requirement that the wave velocity-density field be a solution of the Navier-Stokes equations in the interior of the computational domain in the absence of any perturbations. This is indeed the case for the nonlinear waves considered here when u_w, w_w, $\tilde{\rho_w}$, $\tilde{p_w}$ are introduced into the Euler equations. Specifically, the forcing terms appearing in (2.2) and (2.3) are equal to:

$$F_w^{\mathbf{u}} = -\mathcal{A}(\mathbf{u}_w) - \frac{1}{\rho_0} \nabla \tilde{p} - w_w \frac{\partial U_c(z)}{\partial z} \hat{\mathbf{i}} + \nu \mathbf{L}(\mathbf{u_w}) \quad , \tag{2.11}$$

$$F_w^{(\rho)} = -\mathcal{A}(\tilde{\rho_w}) - w_w \overline{\rho}(z) + \kappa \nabla^2 \tilde{\rho_w} \quad . \tag{2.12}$$

The formulation as given assumes that the flow is planar. If a fully three-dimensional disturbance field is allowed, a spanwise velocity com-

ponent and the lateral momentum equation must be introduced in (2.2)-(2.4) and included in (2.7)-(2.9). Consideration is specifically restricted to plane waves whereby the wave-induced boundary layer will, at least in early stages of evolution, also be two-dimensional. Subsequent evolution of the boundary-generated vorticity may exhibit three-dimensional structure, but characterization of issues such as benthic mixing and dissipation are left for future studies.

The boundary conditions used in the numerical model correspond to the idealized waveguide description of the computational domain described earlier. In the horizontal direction, periodic boundary conditions are employed:

$$(\tilde{u}, \tilde{w}, \tilde{\tilde{p}}, \tilde{\tilde{\rho}})(x, z, t) \;=\; (\tilde{u}, \tilde{w}, \tilde{\tilde{p}}, \tilde{\tilde{\rho}})(x + L_x, z, t) \quad . \tag{2.13}$$

The top boundary is a free-slip non-deformable surface:

$$\left.\frac{\partial \tilde{u}}{\partial z}\right|_{(x,H,t)} = 0 \quad , \qquad \tilde{w}(x, H, t) = 0 \quad . \tag{2.14}$$

Choice of the bottom boundary condition for the disturbance velocity $\tilde{u}$ is crucial to obtain a correct simulation of the unsteady, wave-induced boundary layer. Since, as noted earlier, the boundaries of the wave guide are moving with speed C_{ph} to the right, the application of the no-slip condition on the bottom boundary leads to the conditions:

$$\tilde{u}(x, 0, t) = -u_w(x, 0), \qquad \tilde{w}(x, 0, t) = 0 \quad . \tag{2.15}$$

It is the above mismatch in u-velocity at the bottom boundary that leads to the formation of the wave-induced boundary layer and subsequent global instability. Finally, the density perturbation is subject

to a Dirichlet boundary condition at both vertical boundaries:

$$\tilde{\tilde{\rho}}(x,0,t) = \tilde{\tilde{\rho}}(x,H,t) = 0 \quad . \tag{2.16}$$

2.3 Numerical Method

The numerical methodology used is a recently developed spectral multidomain penalty method for the simulation of high Reynolds number incompressible flows in vertically finite domains. A full discussion of the numerical scheme and its validation (through comparison of simulations of stratified turbulent wakes with non-zero net momentum with corresponding laboratory data) may be found in Diamessis et al. [25]. Only a brief overview is provided here.

The temporal discretization of the governing equations combines third-order stiffly-stable and backward-differentiation schemes with a dynamic high-order boundary condition for the pressure [54]. Thus, maximum temporal accuracy is attained and splitting errors at the vertical boundaries are minimized, as $O(\Delta t^2)$ accuracy is achieved in both velocity and pressure. In the periodic horizontal direction, Fourier spectral discretization is used with $\hat{N}_x$ Fourier modes. In the vertical direction, the computational domain is partitioned into M subdomains of variable height H_k and order of polynomial approximation $\hat{N}_k$ ($k = 1, \ldots M$). The total number of vertical grid points is $\hat{N}_z = M(\hat{N} + 1) + 1$. Within each subdomain, Legendre spectral discretization [13] is used and, for the specific problem under consideration, $\hat{N}_k$ is fixed and equal to a fixed $\hat{N}$ in all subdomains. Subdomains communicate with their neighbors via a

simple patching condition [13]. Among others, the primary advantage of the multidomain discretization [44] is flexibility in local resolution which allows positioning of sufficient number of grid points in the boundary layer (and to a lesser degree in the seasonal thermocline) combined with minimal resolution of the less active ambient fluid outside the boundary region.

For the resolutions considered in this study, dictated by available computational resources and the need for rapid run turnaround, the simulations become under-resolved at higher Reynolds numbers. Although the vertical resolution of the bottom boundary is carefully chosen to capture all phenomena critical to the dynamics of the inviscid region of the unsteady boundary layer, the viscous sublayer is not captured. As a consequence, if an orthogonal polynomial-based spectral discretization is used with no auxilliary stability-ensuring methodology (e.g. filters, penalty schemes), viscosity is not felt by the resolved scales and numerical instabilities develop due to lack of sufficient interpolating polynomial modes and subsequent aliasing effects. Spurious energy with increasingly higher and higher frequency content is then generated producing a catastrophic effect on the long-term integration of the governing equations [33]. To ensure stability of the numerical solution, while preserving its spectral accuracy, penalty techniques [45, 44] are used in the vertical direction along with strong adaptive interfacial averaging [28]. As a final safeguard against numerical instability, explicit spectral filtering is used in all spatial directions [62].

In summary, in regards to the flow under consideration, the above numerical scheme provides two distinct advantages. First, the tempo-

ral discretization, when combined with a spectral spatial discretization, provides maximum temporal accuracy at the boundaries [38] and the solution is not contaminated by the formation of splitting-induced spurious numerical boundary layers [13]. Second, the penalty scheme allows the simulation of the "inviscid" physics of the wave-induced boundary layer (provided sufficient grid points are inserted therein [14]) without requiring resolution of the thin viscous sublayer, which would require a prohibitively high number of grid points. Thus, the internal (internal with regards to the viscous sublayer) inviscid high Reynolds number physics of the flow are captured with spectral accuracy without having to worry about under-resolution-driven numerical instabilities. No enhanced numerical viscosities, which will bias the internal flow dynamics when using a spectral scheme [15], are required. In addition, the excessive artificial dissipation of a low-order finite difference scheme, which can damp features at the smallest resolved scales essential to the global instability, is no longer an issue.

2.4 Simulation Description

Simulations were performed, in order to capture the dynamics of the wave-induced BBL, using the spectral multidomain penalty method model presented in Section 2.3. A summary of the grid resolutions and spectral filter orders is provided in Table 2.1. The height of the computational domain is H, while the length has been chosen in a way that it captures the full NLIW wavelength and additionally allows full development of the BBL and subsequent vortex shedding. In the case of waves

Table 2.1: Summary of grid resolutions and spectral filter orders used in the simulations. Shown for each case are the wave polarity (i.e. wave of depression or elevation), the number of subdomains M, domain resolution $\hat{N}_x \times \hat{N}_z$, order of polynomial approximation $\hat{N}$ in each subdomain (corresponding to $\hat{N}+1$ grid points), order of Legendre/Fourier filters and grid name used.

Wave Polarity	M	$\hat{N}_x \times \hat{N}_z$	$\hat{N}$	(p_L, p_F)	Grid Name
Depression	12	2048×396	32	(8,14)	G1
Depression (wave-train)	12	2304×396	32	(8,14)	G2
Elevation	11	512×187	16	(9,18)	G3

of depression the aforementioned length is bigger than the one chosen for elevation waves because the separation bubble is longer, since it appears in the rear of the wave, and is not confined underneath the wave like it does in the case of elevation waves. A uniform grid is used in the horizontal whereas in the vertical a spectral multidomain discretization (Figure 2.4) with M nonuniform subdomains. Inside each subdomain, the order of polynomial approximation is constant and equal to $\hat{N}$. The positioning of the subdomains is made to ensure sufficient resolution of the BBL dynamics and sufficiently smooth resolution of the thermocline. At the same time, minimal resolution is desired for the "non-active" parts of the flow. The choice of filtering order, both in the horizontal and in the vertical direction, served the minimization of aliasing effects but also left a sufficient number of modes (at least 50%) unaffected by the filter to ensure spectral accuracy of the numerical method.

The computational time step Δt was chosen as such that the CFL

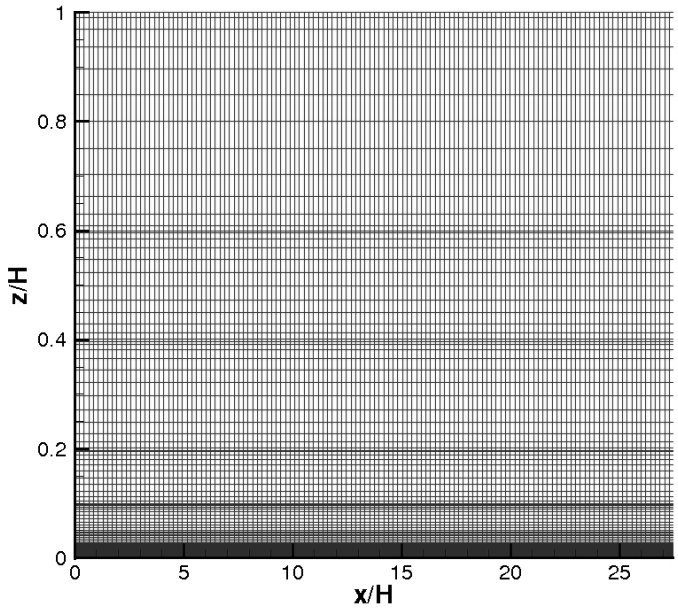

Figure 2.3: The computational grid (G1): less points are plotted for visualization purposes. The distribution of the subdomains and the Gauss Lobatto Legendre points inside each subdomain is the key feature.

stability criterion be satisfied in both spatial directions for a third order stiffly stable scheme at all times [54]. The following requirements are imposed:

$$\Delta t \frac{[C_{ph} + U_C(z) + u_w + \tilde{u}]_{max}}{\Delta x} < 0.2 \quad ; \quad \Delta t \left[\frac{w_w + \tilde{w}}{\Delta z} \right]_{max} < 0.8 \quad . \tag{2.17}$$

In all simulations, the initial time step was set by Eq. (2.17). Upon the onset of global instability, the vertical perturbation velocities increase drastically and consequently the time step needs to be decreased in order to comply with the CFL condition. The dynamic treatment of the time step is provided by an adaptive time-stepping technique [25] based on a third-order variable Δt Adams-Bashforth and backward dif-

Table 2.2: Range of environmental parameters examined.

Parameter	*Symbol*	*Range*
Wave Reynolds Number	Re_w	25,000 –103,000
Wave amplitude	η_{max}/H	0.28 – 0.39
Layer thickness ratio	h_1/h_2	1/10 ; 1/7 4 ; 5
Current strength	U_C/C_{ph}	0 – 0.4

ferentiation schemes. For a typical wave of depression simulation, the total number of time steps is approximately $N_t = 30,000$ requiring four to five days of wall-clock time to run. The simulation ends after the shed vortices re-enter the horizontally periodic computational domain.

The governing environmental parameters of the problem are the wave-based Reynolds number, $Re_w = C_{ph}H/\nu$, the non-dimensional wave amplitude (defined through the maximum isopycnal displacement), η_{max}/H, the layer thickness ratio, h_1/h_2 and the relative current strength, U_C/C_{ph}. The range of parameter values considered in this study is shown in Table 2.4 . The sensitivity of the NLIW-induced BBL to global instability and the associated near-bed flow structure and dynamics to the above parameters are now considered.

A grid independence test was performed using a higher resolution grid of 3072×512 points (grid G4) for the case of a simple depression wave with $Re_w = 100,000$, $\eta_{max}/H = 0.39$, $h_1/h_2 = 1/10$ and $U_C/C_{ph} = 0.4$. The low resolution grid (grid G1) had 2048×396 points. For both grid-

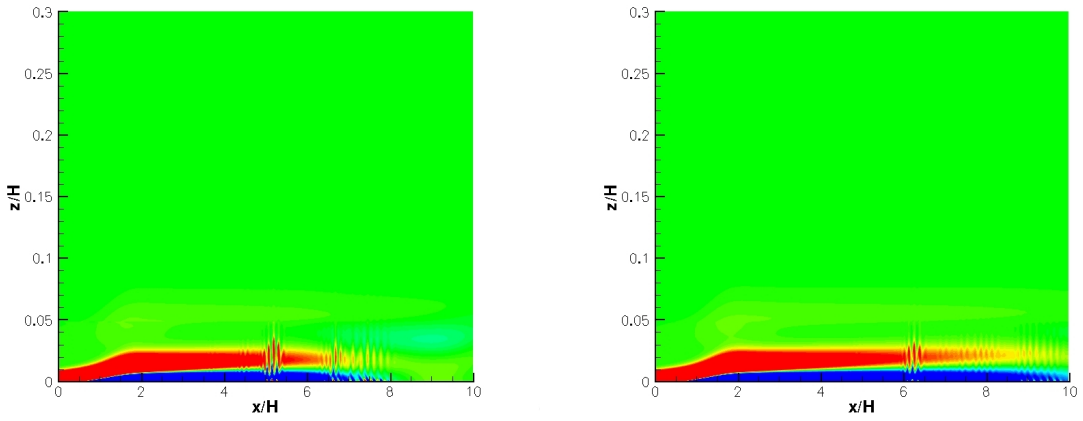

(a) (b)

Figure 2.4: Grid independence test. Exploded views of the perturbation vorticity using grid G1 (a) ($tC_{ph}/H = 7.75$) and grid G4 (b) ($tC_{ph}/H = 10.55$).

independence runs, the computational domain in the horizontal was also smaller ($x/H = 20$) since we only focused on the initial instability development and not the long term evolution and associated intermittency it shows (Section 3.2.1), which would have required a prohibitive computational cost. In Figure 2.4 one can observe that the instabilities in the coarser grid (a) appear at an earlier time and slightly closer to the wave trough than those observed using the finer grid (b). However, beyond this difference the two cases are very similar in terms of vortex diameter, spacing, height of ascent and number of vortices per instability packet, i.e. the basic structure of the BBL is the same for both cases. The difference observed may be attributed to having marginally sufficient resolution with grid G1. Given that the exact origin of vortex shedding is not of interest here (we are more interested in identifying the corresponding stability boundary and characterizing the unstable

BBL structure in terms of the metrics discussed above) and the use of grid G4 for multiple runs could be computationally prohibitive, we elect to work with grid G1 for the remainder of this study. We emphasize that the use of grid G4 was not possible, from a computational and time managing perspective.

CHAPTER 3

RESULTS

3.1 Waves of Elevation

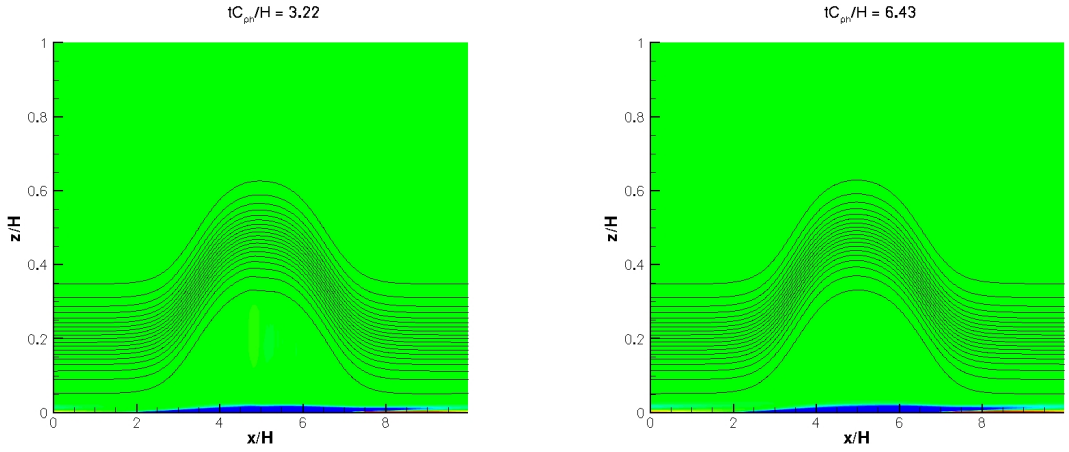

(a) (b)

Figure 3.1: Snapshots of the BBL vorticity field in the wave footprint of an elevation wave ($Re_w = 102,900$; $h_1/h_2 = 4$): Laminar BBL at $tC_{ph}/H = 3.22$ (a). The BBL remains laminar at $tC_{ph}/H = 6.43$ (b).

Even though most of the analysis of the current study is focused on waves of depression, some elevation waves have also been studied. All elevation waves have been simulated in the absence of an oncoming background barotropic current because the current shear profile would overlap with the wave, thus requiring a modified prescription of the NLIW waveform, a capability not offered by the model of Sakai & Redekopp [85]. The observations of the wave-induced BBL could be divided into two categories: 1) The cases of no BBL instability (Figure 3.1), similar to the findings of Carr et al. [18] and 2) the cases where succes-

sive density cores formed inside the wave (Figure 3.2). In the latter case, the core formation was accompanied with baroclinic vorticity generation in the center of the wave, under the wave crest. The cores also interacted with the wave-induced BBL and led to the formation of Kelvin-Helmholtz billows, which deformed the thermocline in the lee side of the wave, contrary to the thermoclinic deformation observed by Stastna & Lamb [92], which was due to the ejection of coherent vortices from the wave-induced BBL into the thermocline at both the leading and trailing edge of the wave. The formation of the cores was found to be dependent on the wave Reynolds number Re_w with core formation being observed at lower Re_w values.

3.2 Waves of Depression

Simulations of depression waves without an oncoming current did not show any BBL instabilities for the Reynolds numbers examined. By comparing the velocity vectors of a simulation without oncoming current (Figure 3.3) and the PIV image obtained from the laboratory experiments of Carr et al. [19] (Figure 3.4), one could observe a key difference: In the laboratory there is a clear flow reversal, whereas in the simulation there is a backflow, but insignificant forward flow. Consequently, in the laboratory experiment there is a region of high shear around $z/H = 0.03$ which is not apparent in our simulation. Therefore the laboratory experiment is more susceptible to an inviscid instability than our simulation. However, it remains unclear if at higher Reynolds number values the wave-induced BBL could become unstable.

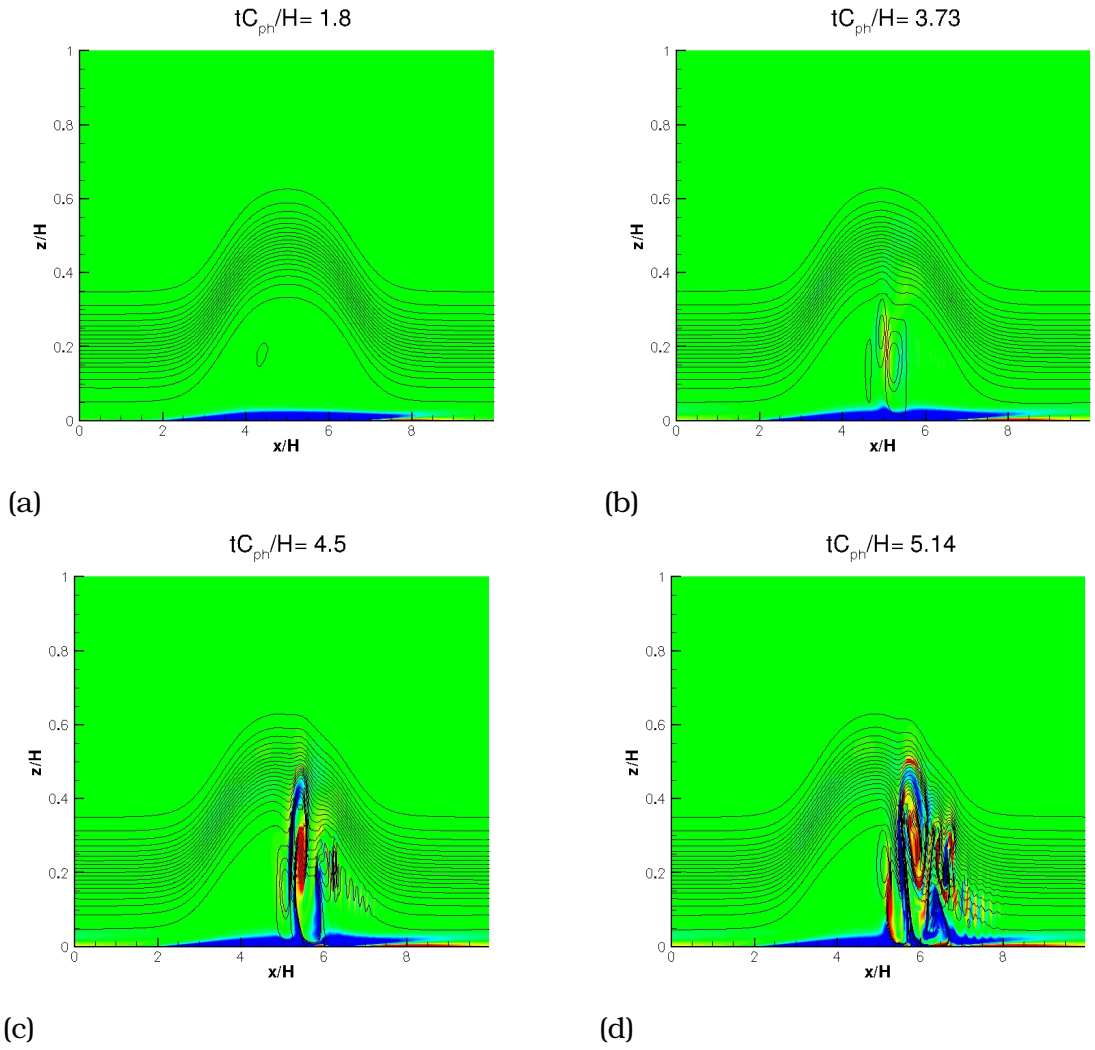

Figure 3.2: Snapshots of the BBL vorticity field in the wave footprint of an elevation wave ($Re_w = 25,700$; $h_1/h_2 = 4$): Laminar BBL at $tC_{ph}/H = 1.8$ and formation of the first density core (a), secondary cores and vorticity between the cores at $tC_{ph}/H = 3.73$ (density isolines interact with the BBL at $x/H = 5.4$) (b), Kelvin-Helmholtz billows at $tC_{ph}/H = 4.5$ deform the thermocline (c) and further deformation of the thermocline at $tC_{ph}/H = 5.14$ (d).

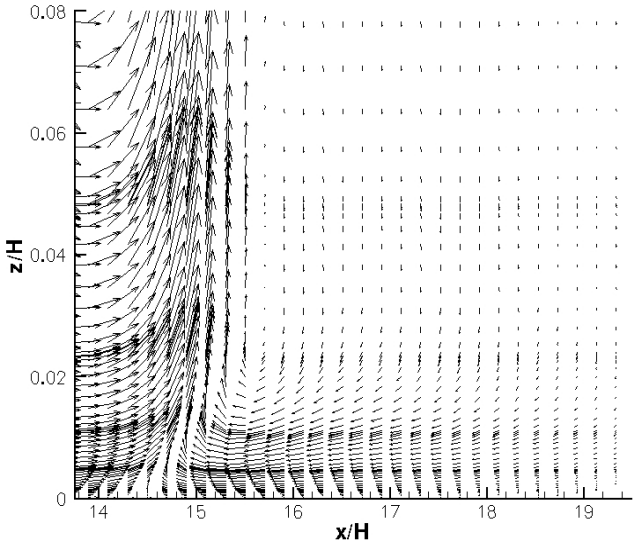

Figure 3.3: Velocity quiver plot at $tC_{ph}/H = 5.90$. ($Re_w = 100,000$; $\eta_{max}/H = 0.39$; $h_1/h_2 = 1/10$; $U_C/C_{ph} = 0$)

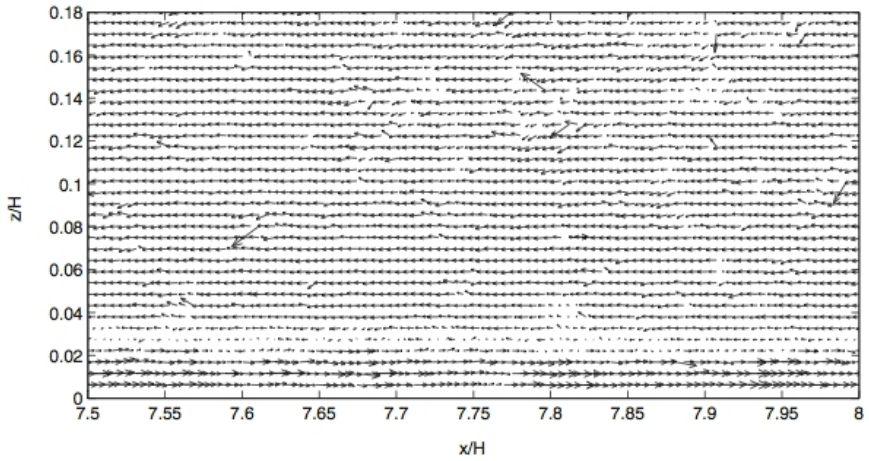

Figure 3.4: PIV image of the wave-induced BBL at $tC_{ph} = 4.10$ from the experiments of Carr et al. [19]. This case corresponds to a depression wave with amplitude $\eta_{max}/H = 0.3$ propagating to the right in a calm ambient environment (no oncoming current) with layer thickness ratio $h_1/h_2 = 1/5$. The wave Reynolds number is $Re_w = 100,000$. The wave is propagating from left to right.

We now focus on the case of a wave of depression propagating against an oncoming current. The case presented here is one of the most favorable towards BBL instability appearance and has the following values of environmental parameters:

$Re_w = 100,000$; $\eta_{max}/H = 0.39$; $h_1/h_2 = 1/10$; $U_C/C_{ph} = 0.4$

Hereafter we will refer to this case as the "base case".

3.2.1 Instability Structure and Evolution

Figure 3.5 (top) is an exploded view of the velocity quiver plot at the wave footprint. The flow separates because of the adverse pressure gradient and creates a separation bubble between $x/H = 14.6$ and $x/H = 18.6$ which can become unstable for values of environmental parameters that exceed a lower critical value. The streamlines make the visualization of the aforementioned separation bubble more evident in Figure 3.5(bottom).

The evolution of the separation bubble of the base case is shown in Figure 3.6. Streamlines show that the core of the separation bubble remains robust but its upstream edge is fragmented at times $tC_{ph}/H = 7.25$ (a) and $tC_{ph}/H = 7.77$ (b) by releasing the first instability packet. The location of the partial fragmentation is close to the reattachment point and this location is the same for all subsequent intermittent vortex shedding events (see also Figure 3.23). After the initial packet, another set of three instability packets (not shown) continues to partially fragment the separation bubble. A relaxation period then follows, during which

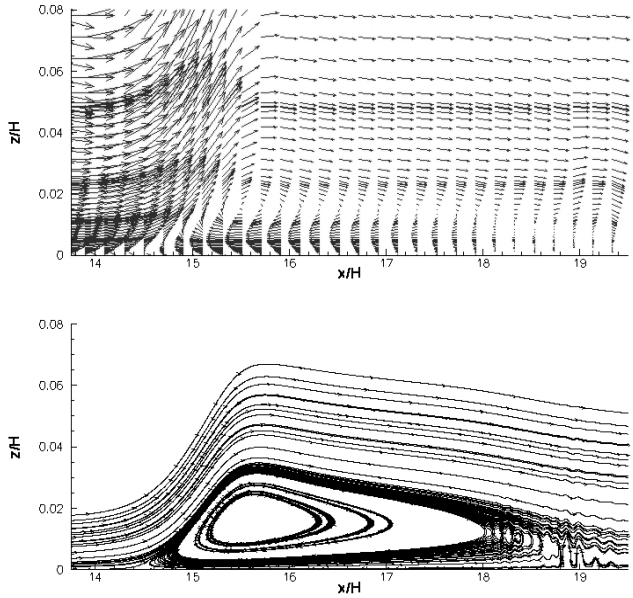

Figure 3.5: Velocity quiver plot (top) and streamtraces (bottom) visualize the flow separation and the separation bubble of the base case respectively at $tC_{ph}/H = 5.82$.

the bubble is reformed (c) and at $tC_{ph}/H = 14.23$ (d) an intermittent instability packet appears that will partially fragment again the separation bubble. The fragmentation of the separation bubble differs from the findings of Diamessis & Redekopp [26], who observed an annihilation of the separation bubble after some vortex shedding.

Four snapshots present the evolution of the NLIW- induced BBL vorticity field in figure 3.7. At early times, before the onset of global instability, a separation bubble forms in the footprint of the NLIW at the rear of the wave and the BBL is laminar (Figure 3.7 (a)). At $tC_{ph}/H \approx 7.3$, a global instability is spontaneously initiated inside the separation bubble which imposes its characteristic length scale, visible as instability waves propagating downstream (Figure 3.7 (b)).The separation bubble

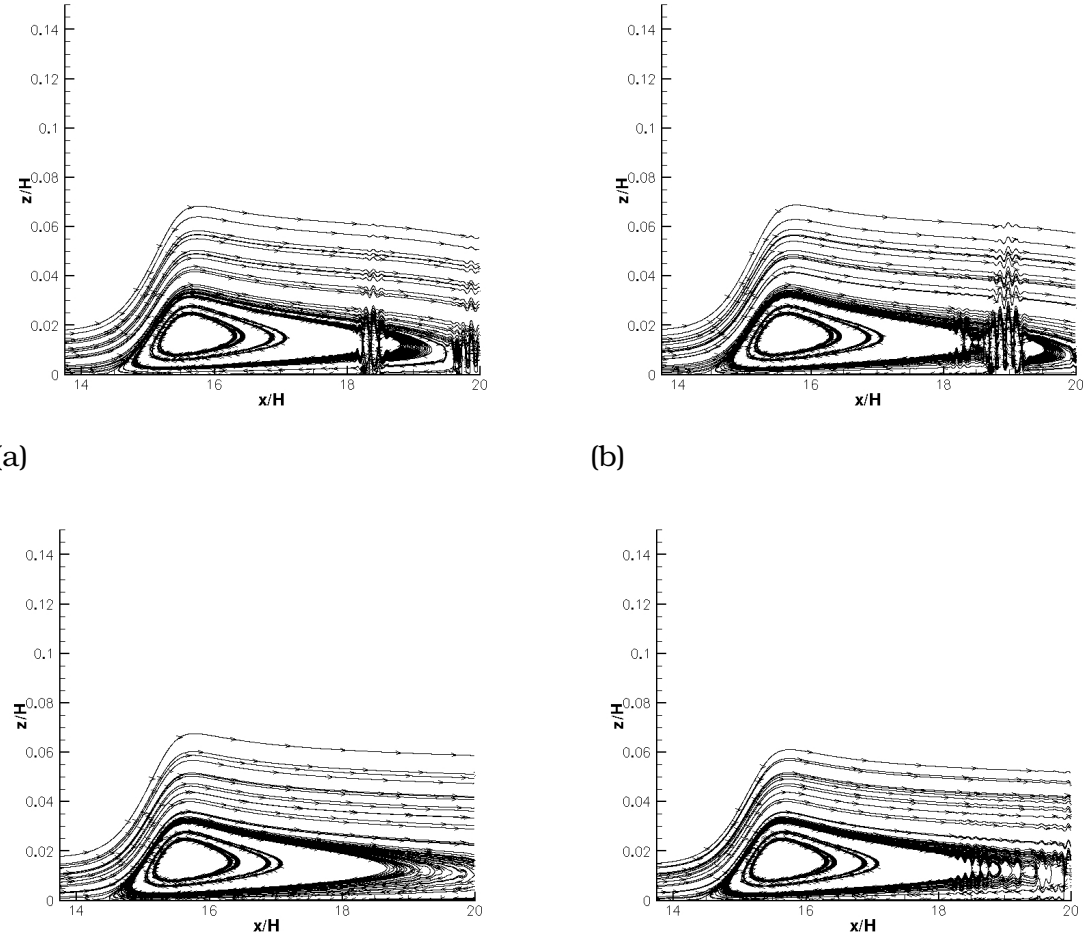

Figure 3.6: Evolution of the separation bubble (streamlines) of the base case. The first instability packet fragments the separation bubble close to the reattachment point at tC_{ph}/H = 7.25 (a) and tC_{ph}/H = 7.77 (b). After the initial packet, another set of three instability packets appears (not shown) and then a relaxation period follows, during which the bubble is reformed (c) (tC_{ph}/H = 11.97). Intermittent instabilities will partially fragment again the separation bubble (tC_{ph}/H = 14.23) (d).

Table 3.1: Comparison of geometrical characteristics of ejected vortices from the wave-induced BBL during the simulation with those obtained from recent laboratory experiments by Carr et al. [19] (Figure 3.8). Note that all the values are non-dimensional.

Vortex	*Simulation*	*Lab*
Thickness	0.05	0.06
Spacing	0.14	0.12
Ejection Height	0.08	0.08

is partially fragmented into a sequence of coherent vortices which are shed up to a maximum height of 8% of the wave-guide depth (Figure 3.7 (c)). This vortex shedding event is not the final. After the initial vortex shedding, a quiescent period follows, the separation bubble then reforms until it reaches a critical size and then breaks again into a second set of coherent vortices (Figure 3.7 (d)), indicating the intermittent nature of the global instability (successive instability packets followed by quiescent periods). The thickness, spacing and maximum ejection height of the vortices are in qualitative agreement with recent laboratory experiments [19] (Figure 3.8) as it is shown in Table 3.2.1. It is also important to observe the existence of "pockets" of alternating vorticity at the bed after the appearance of the instability waves and the shed vortices (Figure 3.7 (b) , (c) and (d)).

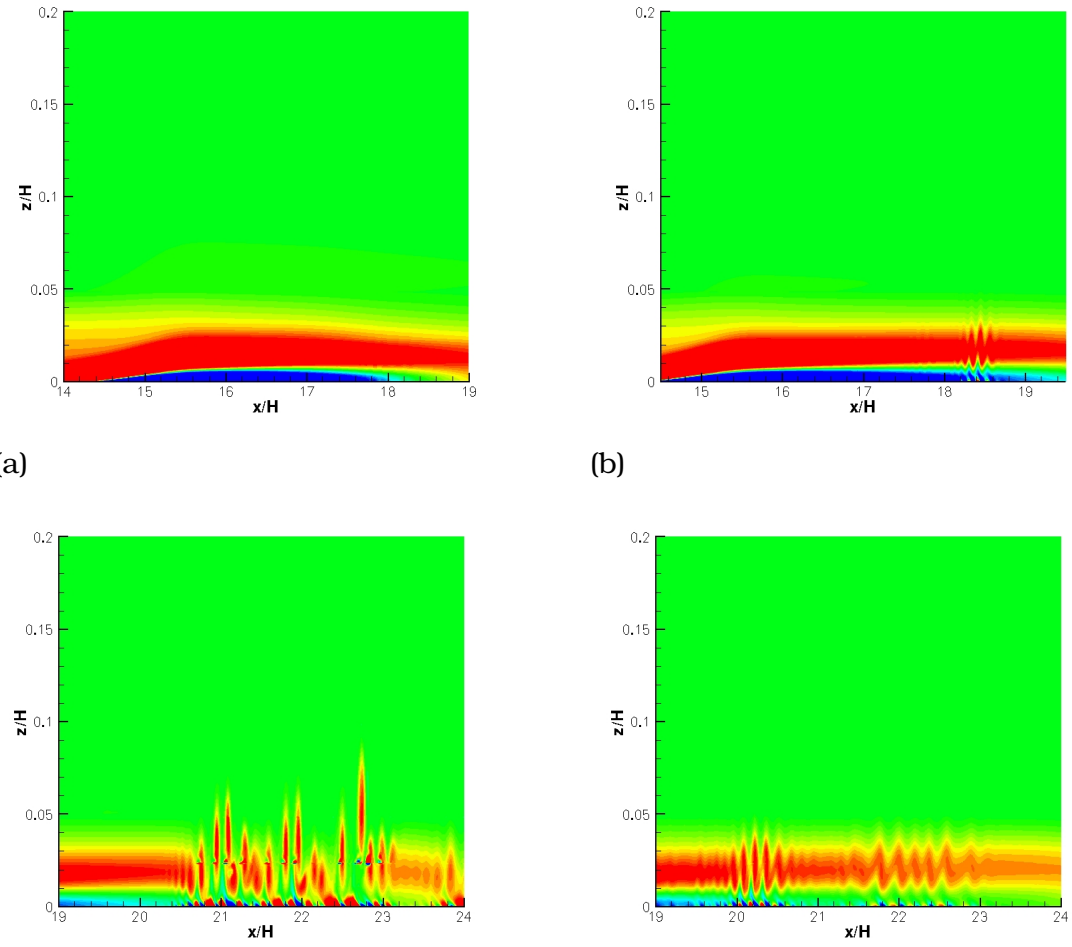

Figure 3.7: Snapshots of the total BBL vorticity field in the wave footprint: Laminar BBL at $tC_{ph}/H = 4.9$ (a), first instability wave packet at $tC_{ph}/H = 7.3$ (b), vortex shedding at $tC_{ph}/H = 10.8$ (c) and secondary instability wave packets at $tC_{ph}/H = 14.2$ (d). The minimum/maximum values of the x-coordinate differ between snapshots but the x-interval is the same.

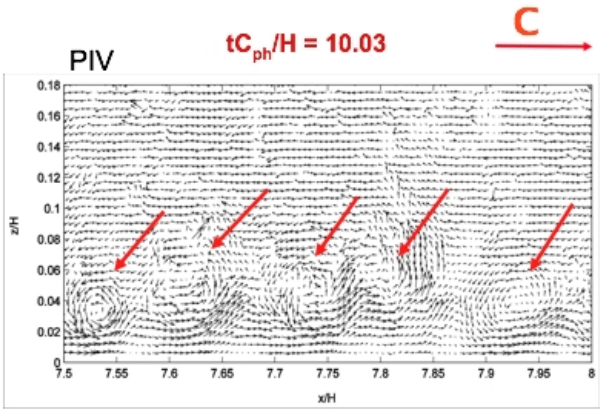

Figure 3.8: PIV image of the wave-induced BBL at $tC_{ph}/H = 10.03$ from the experiments of Carr et al. [19]. This case corresponds to a depression wave with amplitude $\eta_{max}/H = 0.3$ propagating to the right in a calm ambient environment (no oncoming current) with layer thickness ratio $h_1/h_2 = 1/5$. The wave Reynolds number is $Re_w = 100,000$. Red arrows indicate vortices shed from the wave-induced BBL.

3.2.2 Near-Bed Velocities

The vertical perturbation velocities recorded by a virtual point sensor (positioned at $x/H = 20.6$ and $z/H = 0.02$ translating with the wave phase speed C_{ph}) are shown in Figure 3.9. The vertical velocities assume values up to 13% of the wave phase speed when the vortices are shed, contrary to the findings of Diamessis & Redekopp [26] who observed vertical velocities of the same order with the wave phase speed caused by the artificially large wave amplitudes predicted by the weakly nonlinear KdV theory they applied. The oscillations in the velocity timeseries

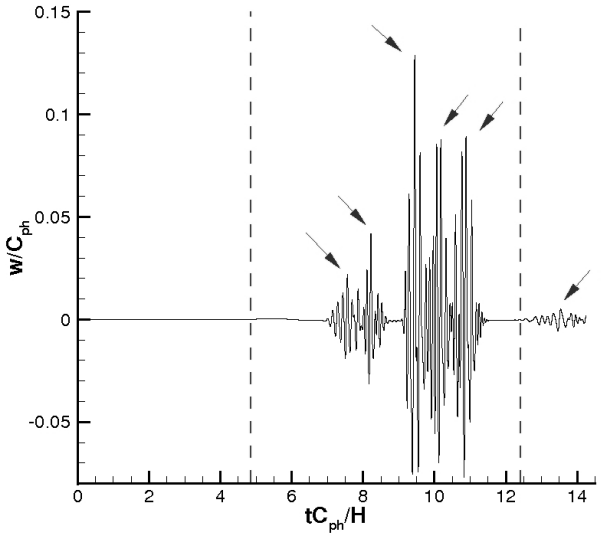

Figure 3.9: Near-bed perturbation vertical velocities obtained from virtual point sensor translating with the wave phase speed. The arrows indicate the maximum vertical velocities during each vortex shedding event.

are the signature of vortex shedding. The intermittency associated with highly active periods (indicated by arrows) interrupted by inactive ones is indicative of successive instability packets (and groups of shed vortices) driven by the global instability. Furthermore, one can observe that the velocity amplitudes in the active periods are enveloped, assuming values of approximately zero at the beginning and at the end of each active period and maximum absolute values at the center, separating in this way the instability packets. Finally, a dominant frequency, characteristic of the global instability, is observed in the time series with a peak to peak separation of $tC_{ph}/H \approx 0.15$.

Near bed perturbation velocities were also obtained by Eulerian virtual point sensors located at $x/H = 13.04$ and at three vertical positions

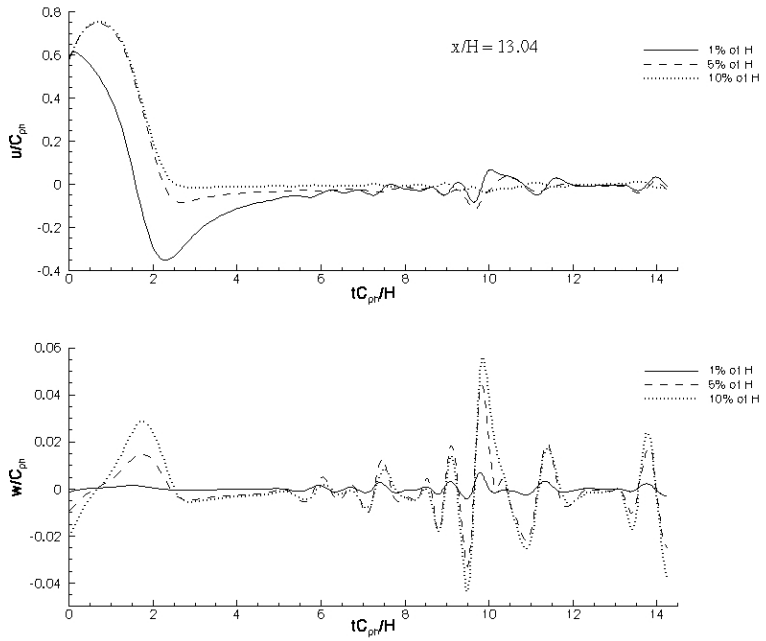

Figure 3.10: Near-bed perturbation velocities obtained by an eulerian virtual sensor array positioned at $x/H = 13.04$.

corresponding to 1%, 5% and 10% of the wave-guide depth. The horizontal velocity components are shown in Figure 3.10 (top), while the vertical ones are shown in the same figure at the bottom. By looking at the horizontal velocities one can observe that the point sensor positioned at 1% of the wave-guide depth assumes negative values right after the passage of the wave, because of the flow reversal caused by the adverse pressure gradient, while at later times, the horizontal velocities are oscillating around the zero value and the lower two sensors have a 180^0 phase shift with the sensor located at a depth equal to 10% of H (Figure 3.11), a signature of the shed vortices. Similar alternations in sign appear in the vertical perturbation velocities as well, again indicative of a single vortex. Note that the vertical velocities are higher in absolute magnitude for the sensors located at 5% and 10% of the water

column than those of the sensor which is located closest to the bed, which means that the shed vortices pass closer to the two aforementioned sensors. The magnitude of the velocities is similar to the ones observed in the laboratory (Figure 3.12).

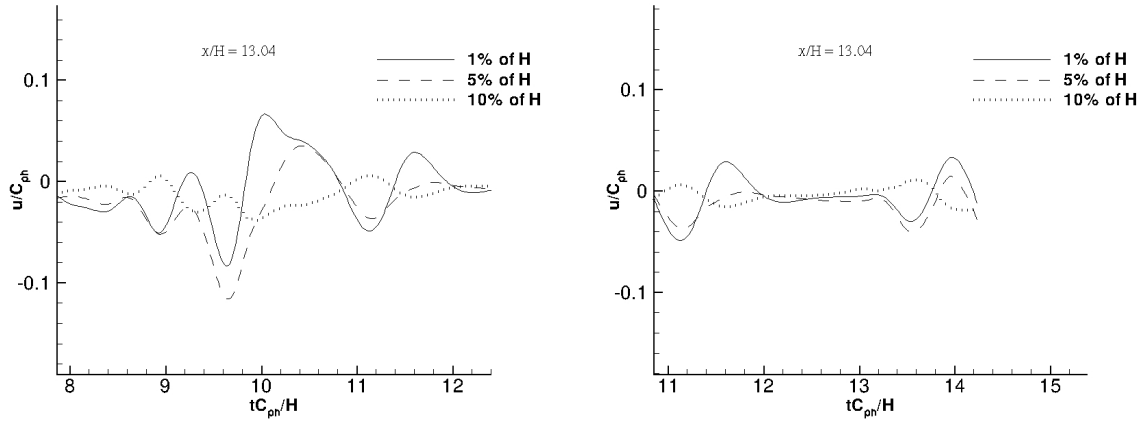

(a) (b)

Figure 3.11: Exploded view of the u perturbation velocity obtained by the eulerian virtual point sensor array. Signature of vortex shedding is the fact that the lower two sensors have 180^0 phase shift with the sensor located higher in the wave-guide.

3.2.3 Bottom Shear Stress Evolution

Two images of the bottom shear stresses are shown in Figure 3.13 at times tC_{ph}/H = 4.84 and 12.40, indicated by dashed lines in Figure 3.9. At tC_{ph}/H = 4.84 the bottom shear stresses are everywhere zero apart from their laminar component induced by the passage of the wave. Later, during the onset of instabilities and the subsequent vortex shedding, the bottom shear stresses at the rear of the wave assume values comparable

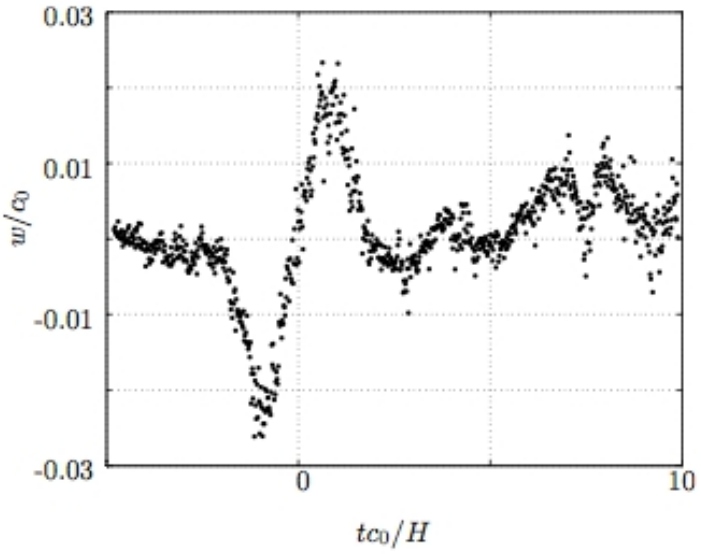

Figure 3.12: Near-bed vertical velocities obtained in the laboratory (Carr et al. [19]) by an eulerian virtual sensor positioned at $x/H = 7.598$ and $z/H = 0.052$.

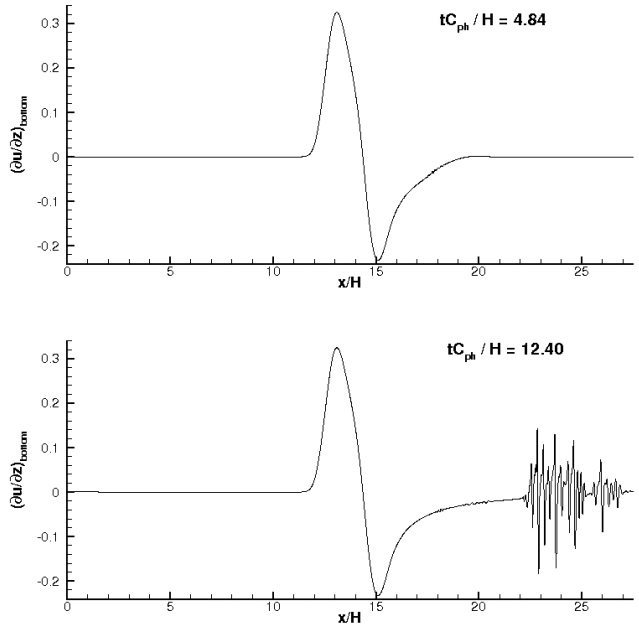

Figure 3.13: Bottom shear stresses before and after instability appearance at times $tC_{ph}/H = 4.84$ and 12.40 .

with the ones induced by the wave. Moreover, the high spatial variability of the bottom shear stresses suggests an enhanced potential for bottom sediment resuspension.

3.3 Effect of Environmental Parameters on the Bottom Boundary Layer Instabilities

The effect of environmental parameters such as the wave Reynolds number Re_w, wave amplitude η_{max}, current strength U_C and layer thickness ratio h_1/h_2 on the instability structure and evolution are now examined. Table 3.3 shows the cases considered.

Table 3.2: Cases compared in order to examine the effect of layer thickness ratio, wave amplitude, wave Reynolds number and current strength on the BBL instabilities.

Case	h_1/h_2	η_{max}/H	Re_w	U_C/C_{ph}
Base Case	1/10	0.39	100,000	0.4
C1	1/7	0.365	100,000	0.4
C2	1/10	0.38	100,000	0.4
C3	1/10	0.39	60,000	0.4
C4	1/10	0.39	100,000	0.2

To begin with, the effect of the depth of the thermocline will be examined. It is important to note that both case C1 and the base case have wave amplitudes close to the conjugate state limit, which is, however, not the same for different layer thickness ratios. Figure 3.14 shows the

evolution of BBL instabilities, which is similar to the base case (Figure 3.7). Upon the onset of global instability ($tC_{ph}/H = 6.70$), instability wave packets propagate downstream (top) with a characteristic length scale. Later, the separation bubble is partially fragmented into a series of coherent vortices which are again shed up to a maximum height equal to 8% of the wave-guide depth (bottom). The thickness and spacing of the vortices are similar to the ones observed at the base case. Furthermore, the existence of "pockets" of alternating vorticity at the bed is also apparent in this case.

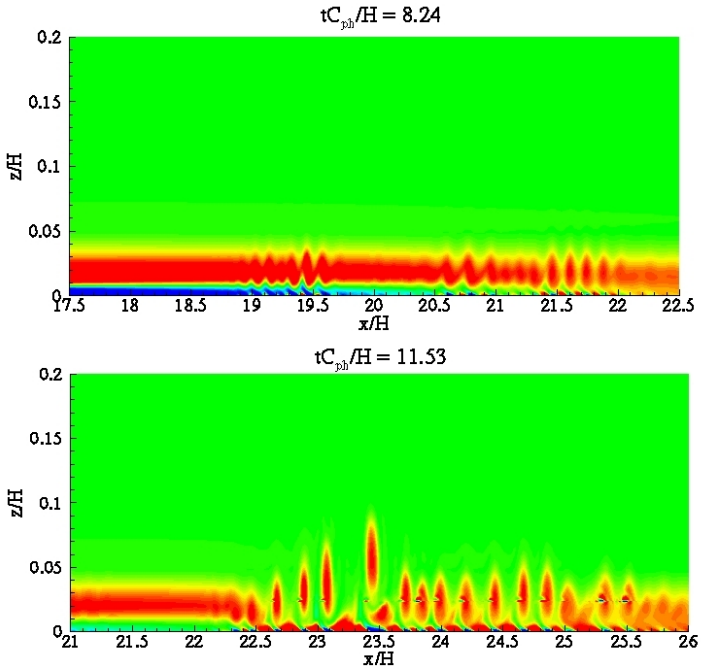

Figure 3.14: Snapshots of the total BBL vorticity field corresponding to case C1 at times $tC_{ph}/H = 8.24$ and 11.53 .

Subsequently, the effect of reducing the wave amplitude is examined for case C2. In Figure 3.15 (top), instability waves appear at $x/H = 21.4$, in comparison with the base case and case C1, where the instability waves appeared at $x/H \approx 19$, suggesting that in case C2 the instability

waves appeared further away from the wave trough than in the previous two cases. Weak instabilities are also apparent at later time, but no coherent vortex shedding is observed.

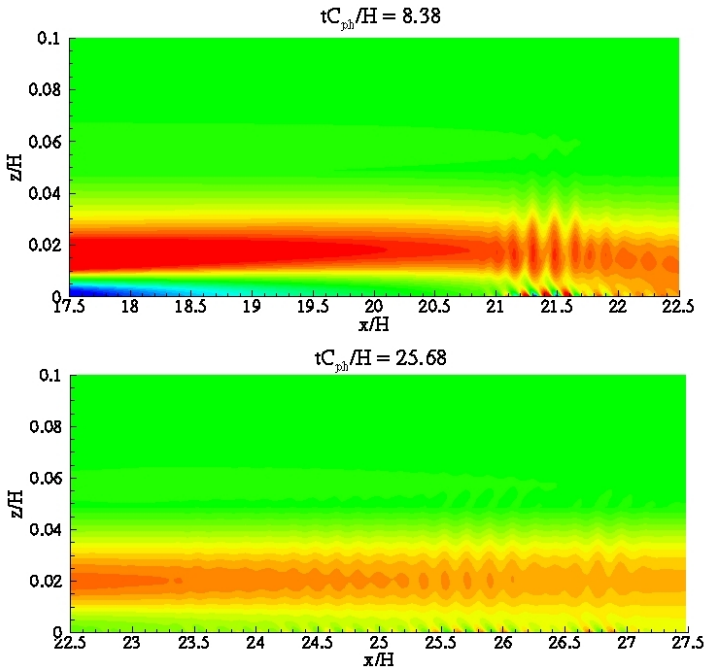

Figure 3.15: Snapshots of the total BBL vorticity field corresponding to case C2 at times tC_{ph}/H = 8.38 and 25.68 .

Reducing the wave Reynolds number or the oncoming current strength has similar effect on the structure of the wave-induced BBL instabilities with a reduction in wave amplitude. The instability waves appear further away from the wave trough (x/H = 20.5 and x/H = 21.5 respectively) than in the base case (Figures 3.16 (top) and 3.17 (top)). Weak vortex-like structures are apparent at times tC_{ph}/H = 15.99 and tC_{ph}/H = 14.17 respectively but they are neither as intense as in the base case nor as numerous (Figure 3.16 (bottom)). In table 3.3 the time of onset of global instability is identified for all the cases.

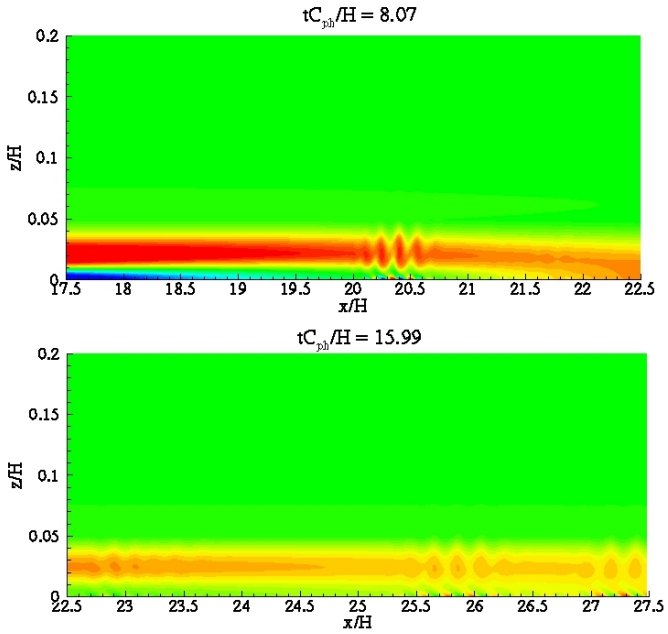

Figure 3.16: Snapshots of the total BBL vorticity field corresponding to case C3 at times $tC_{ph}/H = 8.07$ and 15.99 .

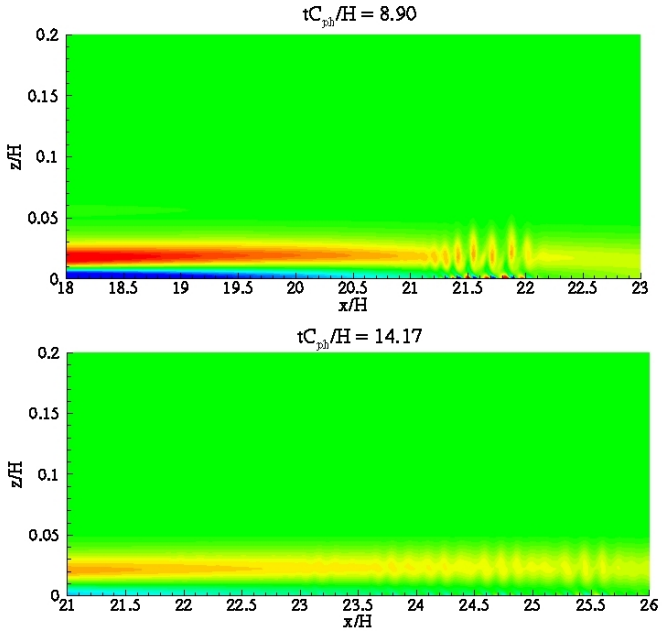

Figure 3.17: Snapshots of the total BBL vorticity field corresponding to case C4 at times $tC_{ph}/H = 8.90$ and 14.17 .

Table 3.3: Time of onset of global instability identified for all the cases.

Case	Time of Onset (tC_{ph}/H)
Base Case	6.20
C1	6.70
C2	7.13
C3	7.18
C4	6.78

The near-bed perturbation velocities obtained by a virtual point sensor positioned at $x/H = 20.6$ and $z/H = 0.02$ and translating with the wave phase speed are shown in Figure 3.18 for cases C1, C2, C3 and C4. Apart from case C1 where the perturbation vertical velocities assume values up to approximately 13% of the wave phase speed, in all the other cases the aforementioned velocities are not higher than 5% of the wave phase speed, significantly lower than the values assumed by the base case (Figure 3.9). However, all cases present some key similarities: 1)Intermittency in the appearance of the instability is associated with the succession of highly active periods with inactive ones, 2) a dominant frequency, characteristic of the global instability, is apparent on the time signal and this frequency is similar for all the cases ($tC_{ph}/H \approx 0.15$) and 3) the velocity amplitudes at each active period are enveloped, with higher values in the middle of each period.

Comparison of the bottom shear stresses is provided in Figure 3.19. The times chosen for the comparison correspond to the times when absolute maximum values of bottom shear stress, induced by the instabil-

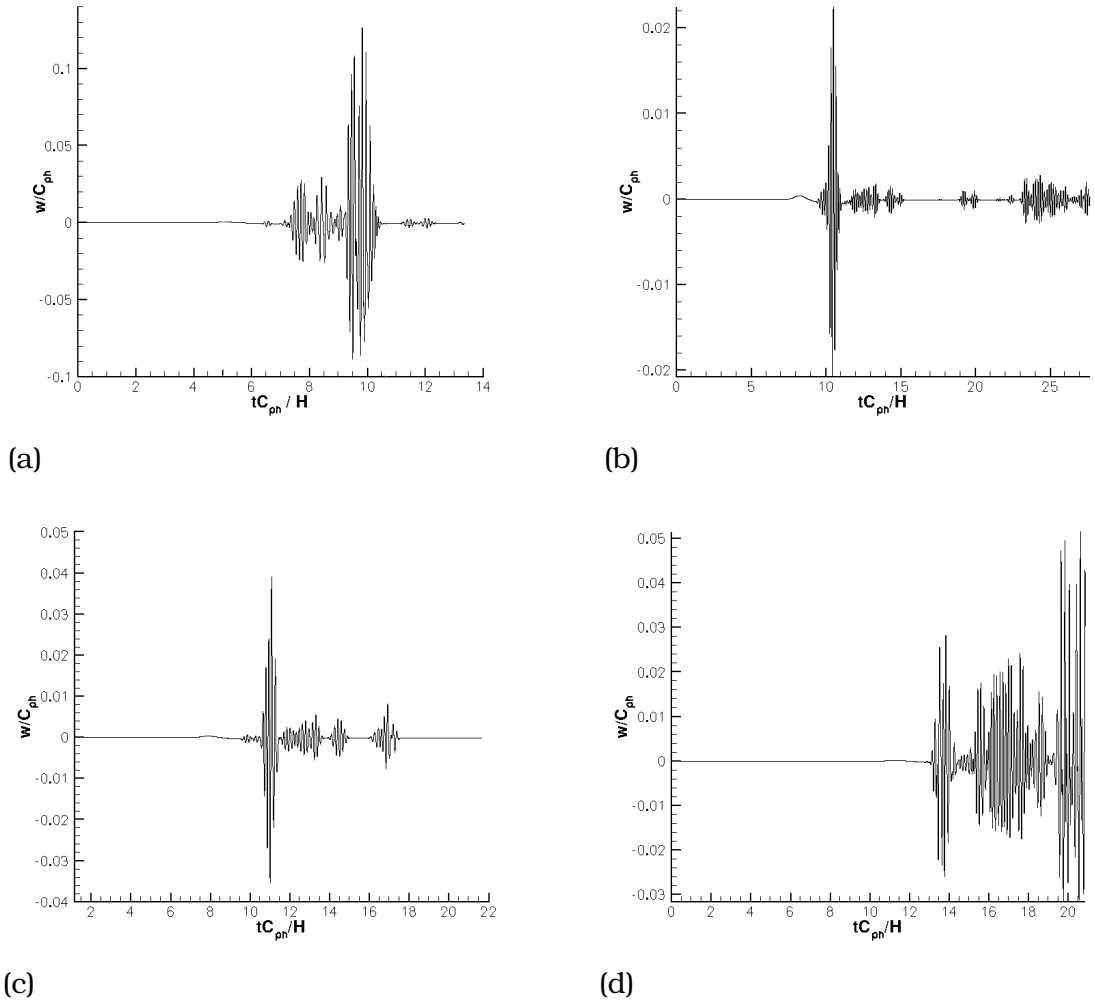

Figure 3.18: Comparison of near-bed vertical perturbation velocities obtained by a virtual point sensor positioned at $x/H = 20.6$ and $z/H = 0.02$ and translating with the wave phase speed. Case C1 (a), case C2 (b), case C3 (c) and case C4 (d).

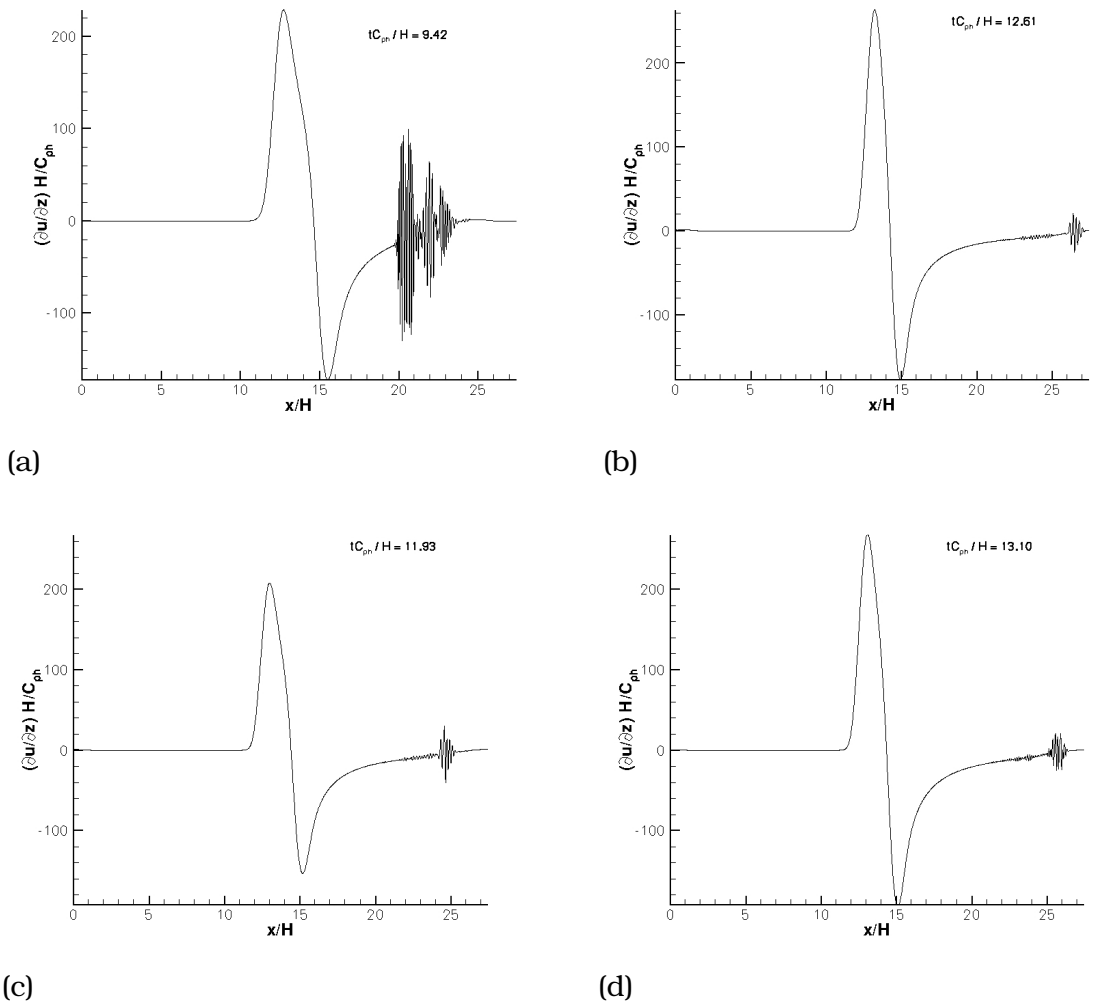

Figure 3.19: Comparison of bottom shear stresses. Case C1 (a), case C2 (b), case C3 (c) and case C4 (d).

ities in the rear of the wave, are observed. The partial values in cases C2, C3 and C4 are not comparable with the ones induced by the wave, which is expected since there is no or weak vortex shedding in these cases and consequently no ”pockets” of alternating vorticity on the bed, the existence of which is directly related to the vortex shedding, with one ”pocket” of positive vorticity underneath each vortex. Consequently, since vorticity is equal to shear stress at the bottom, by measuring the

crests of the bottom shear stresses, one can find the number of shed vortices. In case C1, similarly to the base case (Figure 3.13), the bottom shear stresses assume values comparable to the ones induced by the wave and they present high spatial variability, with interchanging positive and negative sign, which implies an enhanced potential for sediment resuspension. In all cases, during each burst, the number of shed vortices varies between 5 and 12, with more vortices per burst being observed in case C1 and the base case.

3.4 Separation Bubble Structure

Since wave-induced BBL vortex shedding is directly related to the partial fragmentation of the separation bubble underneath the NLIW, it is important to identify how the structure of the separation bubble is affected by the layer thickness ratio and the oncoming current strength. To this end, comparison of snapshots of the separation bubbles (visualized by streamlines) of cases C1 and C4 with the base case is made. The snapshots were taken just before the onset of global instability.

The effect of the layer thickness ratio is presented in Figure 3.20. The top picture corresponds to case C1, while the bottom one corresponds to the base case. It is important to note that, in both cases, the separation bubble is partially fragmented into a sequence of coherent vortices which were shed further up in the water column. Both separation bubbles have similar geometry, and approximately equal maximum height. In the base case, the separation bubble is slightly shorter and is located

slightly closer to the x-location of the wave trough (x/H = 13.75). There is also stronger recirculation inside the bubble, which can be seen by the greater number of closed streamlines inside this region.

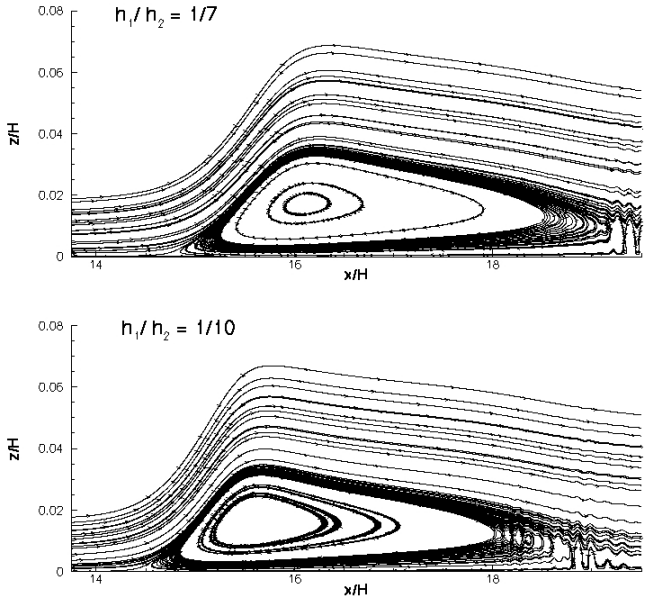

Figure 3.20: Snapshots of the separation bubble underneath the NLIW for different layer thickness ratios (case C1 on top and base case on bottom).

The effect of the oncoming current strength is presented in Figure 3.21. The top picture corresponds to case C4, while the bottom one corresponds to the base case. In case C4 only weak vortex shedding was observed. The separation bubble is thicker and its maximum height is approximately 50% greater than the that of the base case but its x-location is equal in both cases ($x/H \approx 15.7$). The separation bubble corresponding to case C4 is longer and appears to have stronger recirculation inside. However, comparison on the strength of the recirculation inside the two bubbles might be inappropriate in this case since they do not

have the same thickness.

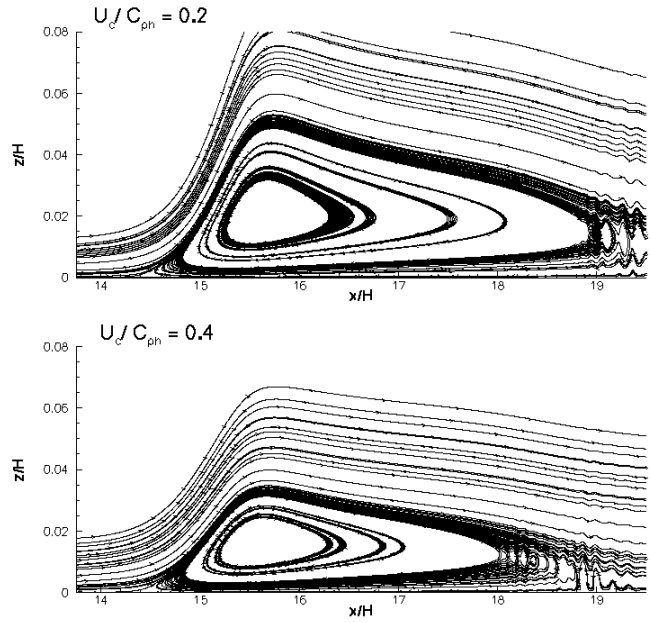

Figure 3.21: Snapshots of the separation bubble underneath the NLIW for different layer thickness ratios (case C4 on top and base case on bottom).

3.5 Stability Boundary Curve

A stability boundary which provides the critical wave amplitude above which global instability is observed as a function of Re_w may now be constructed. To this end, a simulation is regarded as one with a globally unstable boundary layer if instabilities are observed before the wave-induced b.b.l. re-enters the computational domain because of periodic boundary conditions in the horizontal direction. The critical wave amplitude for BBL instability onset is identified as a function of the Reynolds number for different layer thickness ratios and oncoming cur-

rent strength (Figure 3.22). On the same diagram are plotted a selected critical value from the laboratory experiments performed by Carr et al. [19] denoted by black circle. The critical wave amplitude decreases with increasing Reynolds number, oncoming current strength and deeper thermocline.

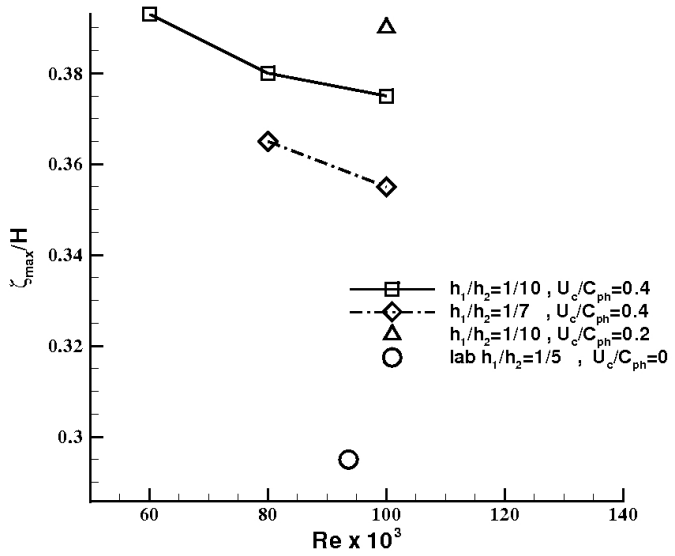

Figure 3.22: Critical wave amplitude for instability appearance as a function of Re_w. All data points are obtained from our DNS, with the exception of the circle which is obtained from the laboratory experiments of Carr et al. [19].

3.6 Bottom Shear Stress *x-t* Contour Plot

Earlier it was observed that "pockets" of alternating vorticity were present at the bottom at the cases when global instability was observed. These "pockets" are located underneath the instabilities and thus they propagate with the same speed. Furthermore, one can directly find that

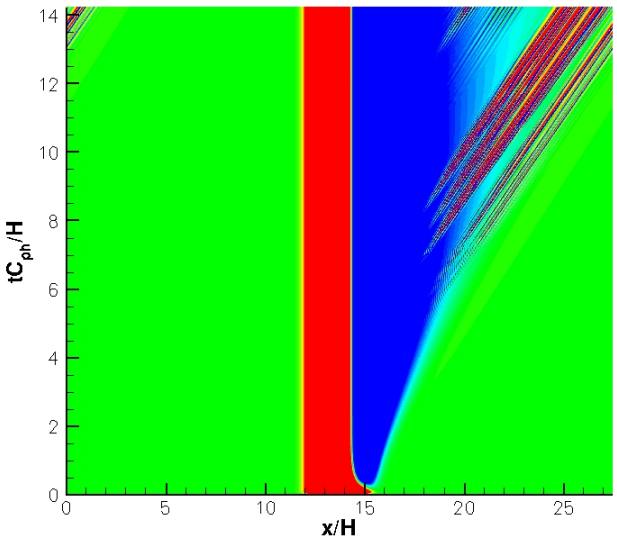

Figure 3.23: Bottom shear stress x-t contour plot corresponding to the base case.

the bottom shear stresses are equal with the vorticity at the bottom since $\frac{\partial w}{\partial x} = 0$ everywhere at the bottom boundary. Hence, from an x-t contour plot of the bottom shear stresses one can find the propagation speed of the instabilities, the location where they first appear and the time it takes between two successive vortex shedding events.

In Figure 3.23 one can observe that the instabilities first appear at $tC_{ph}/H = 6$ and $x/H \approx$ 18-19. This x-location according to Figures 3.20 (bottom) and 3.21 (bottom) corresponds to the region close to the reattachment point of the separation bubble and remains the same location for all the vortex shedding events (Figure 3.23). The instabilities have a constant relative propagation speed 17% higher than the wave phase speed, which can be found by the inverse of the slope of a ray of constant bottom vorticity. The propagation speed of the instabilities is

constant (the rays do not have an inflection point or a curvature) and is the same for all instability packets (parallel rays). Finally, one can observe by looking at $x/H = 19$ that after the onset of global instability and the subsequent energetic vortex shedding period, follows a period during which the bottom shear stresses relax. Secondary instabilities appear at $tC_{ph}/H = 13.5$, having the same propagation speed, which denotes the intermittent nature of these wave-induced BBL instabilities. (Note that some instabilities have re-entered the computational domain because of x-periodicity at time $tC_{ph}/H = 13$). Figure 3.24 represents the bottom shear stress x-t contour plot in a fixed frame of reference, from which it can be observed that the ejected vortices are almost stationary.

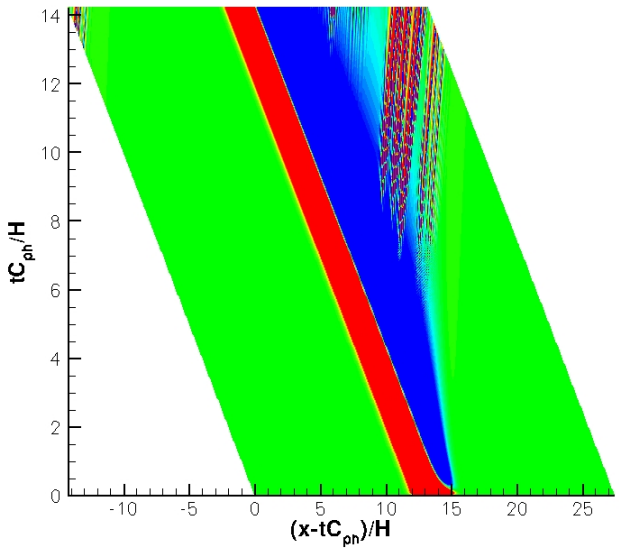

Figure 3.24: Bottom shear stress x-t contour plot corresponding to the base case.

3.7 Two-Wave Scenario

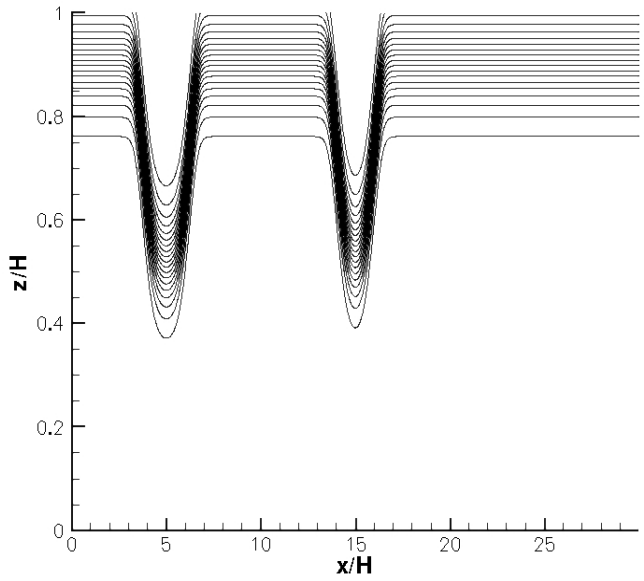

Figure 3.25: Supercritical leading wave and subcritical trailing wave geometry.

In nature, NLIWs usually cannot be found as solitary waves but instead propagate as wave-packets. So the question that arises is how does the BBL of a trailing wave interact with the BBL of the leading wave? More specifically, we were interested in the case of a NLIW of subcritical amplitude following a NLIW with supercritical amplitude. Figure 3.25 shows the geometry of the 2-wave-train. The leading wave has amplitude $\eta_{max}/H = 0.39$ while the amplitude of the trailing wave is $\eta_{max}/H = 0.37$. The Reynolds number is $Re_w = 100,000$ and the oncoming current strength is 40% of he wave phase speed. Before the two BBLs interact with each other, one can observe, vortices being shed under the leading wave while the BBL of the trailing wave is laminar (Figure 3.26

(a)), in agreement with the stability boundary diagram (Figure 3.22). When the vortices shed by the BBL of the leading wave interact with the BBL of the trailing wave, the latter becomes unstable, instability packets appear and subsequently vortices are shed (Figure 3.26 (b)). The separation bubble finally partially fragments and the vortex shedding under the subcritical trailing wave is even more intense than the equivalent procedure under the supercritical leading wave.

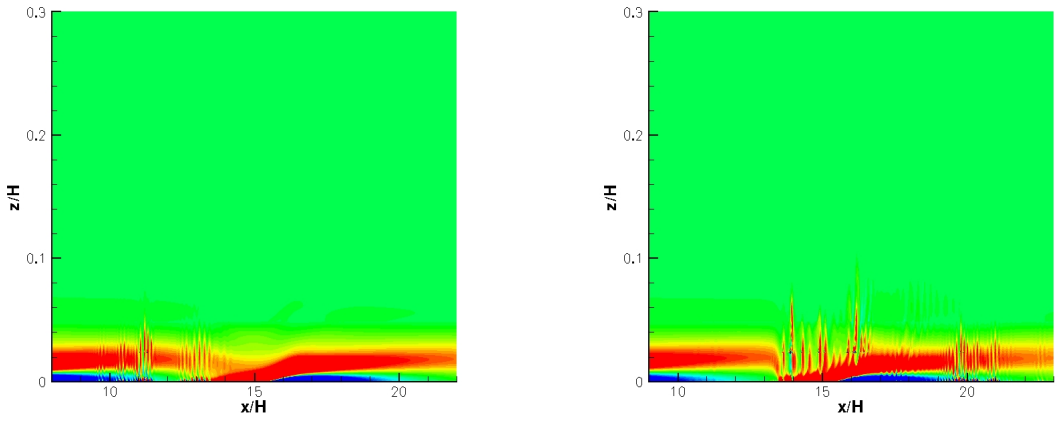

(a) (b)

Figure 3.26: BBL vorticity contours before (a) and after (b) the vortices shed by the BBL of the leading wave interact with the BBL of the trailing wave at times $tC_{ph}/H = 8.7$ and $tC_{ph}/H = 12.2$ respectively.

In Figure 3.27 a bottom shear stresses x-t contour plot is shown. Again here it can be seen that instabilities under the trailing wave appear after the interaction of the BBL instabilities induced by the leading wave interact with the BBL induced by the trailing wave. However, an important observation is that the instabilities under the trailing wave have the same propagation speed with those induced by the leading wave. Figure 3.28 shows the near bed vertical velocities obtained by a

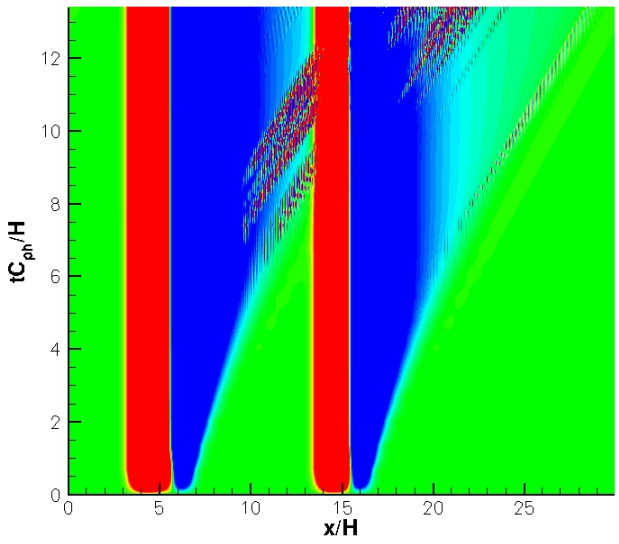

Figure 3.27: Bottom shear stress x-t contour plot corresponding to the base case.

virtual point sensor positioned at $x/H = 20.6$ and $z/H = 0.02$ and translating with the wave phase speed. The vertical velocities assume values up to 12% of the wave phase speed, similarly to the base case and are highly oscillatory (frequency $tC_{ph}/H \approx 0.12$).

3.8 Noise Insertion

Despite the fact that the laboratory experiments of Carr et al. [19] are inherently Three-Dimensional, the observed flow structure in the wave-induced BBL, is similar to that obtained from our 2-D simulations. However, they observed global instability for a less favorable set of environmental parameter values (Figure 3.8) than those predicted by our

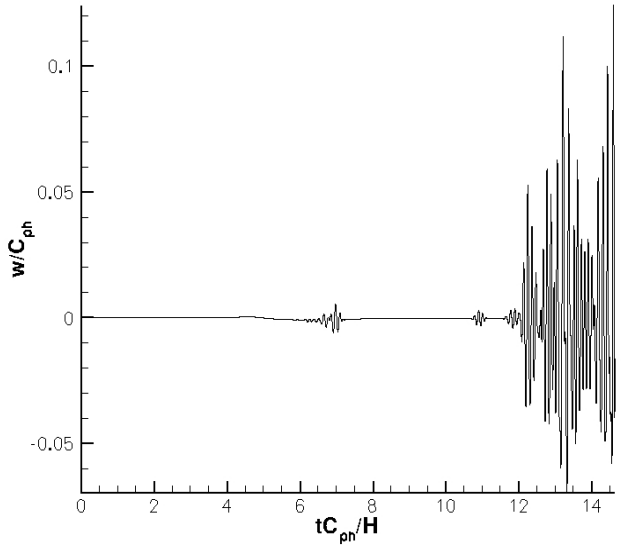

Figure 3.28: Near bed vertical velocities recorded by a virtual point sensor positioned at $x/H = 20.6$ and $z/H = 0.02$ and translating with the wave phase speed.

simulations (Figure 3.22). The fact that in the laboratory, the BBL instabilities appeared with sets of environmental parameter values less favorable towards instability, together with the finding from the 2-wave scenario that the BBL under the trailing subcrcritical wave became unstable when it was perturbed by a physically generated noise (vortices shed by the BBL of the leading wave), led us to wonder whether the wave-induced BBL under a subcritical NLIW could be excited and become unstable after the instantaneous insertion of a controlled external noise. To investigate this possibility, we imposed a perturbation velocity field on the wave-induced BBL at the x-location where maximum flow reversal was observed. The perturbations were inserted after the BBL was fully developed. The perturbation field was designed to excite the most unstable primary instabilities of the reverse velocity profile in the sepa-

rated BBL. The velocity field was constructed assuming a parallel shear flow analysis with the standard hyperbolic tangent shear layer profile used as an approximation of the region close to the inflection point. The aforementioned analysis is not the optimal for the NLIW-induced BBL profile which is x-dependent, but is easy to implement and is sufficient to ”trigger” the BBL.

Thus, the perturbation velocity field has the following form [89]:

$$\hat{u} = \frac{u_0}{2}\left[-cos(2k_0x) + 2b\,cos(k_0x)\right] tanh\,\frac{2(z-z_0)}{h_0}\,sech^2\,\frac{2(z-z_0)}{h_0} \tag{3.1}$$

$$\hat{w} = \frac{u_0}{4}\left[sin(2k_0x) - b\,sin(k_0x)\right] sech^2\,\frac{2(z-z_0)}{h_0} \tag{3.2}$$

Where h_0 denotes the perturbation layer thickness, u_0 is the absolute value of the maximum velocity difference inside the shear layer, k_0 is the streamwise wavenumber of the fastest growing eigenmode and z_0 is the vertical location of the shear layer's velocity inflection point. The streamwise wavenumber was carefully selected to result in a wavelength which is an integer fraction of the computational domain length in order to ensure periodicity in the horizontal direction. The magnitude of the perturbations was controlled by a coefficient α. The parameters h_0 , z_0 and k_0 can be determined using the shear layer thickness δ_ω, which is the vertical distance from the point of maximum backflow to the point where the velocity reaches a constant value, as:

$$h_0 = \frac{\delta_\omega}{3},\ z_0 = \frac{2\delta_\omega}{3},\ k_0 = \frac{2\pi h_0}{\lambda} \tag{3.3}$$

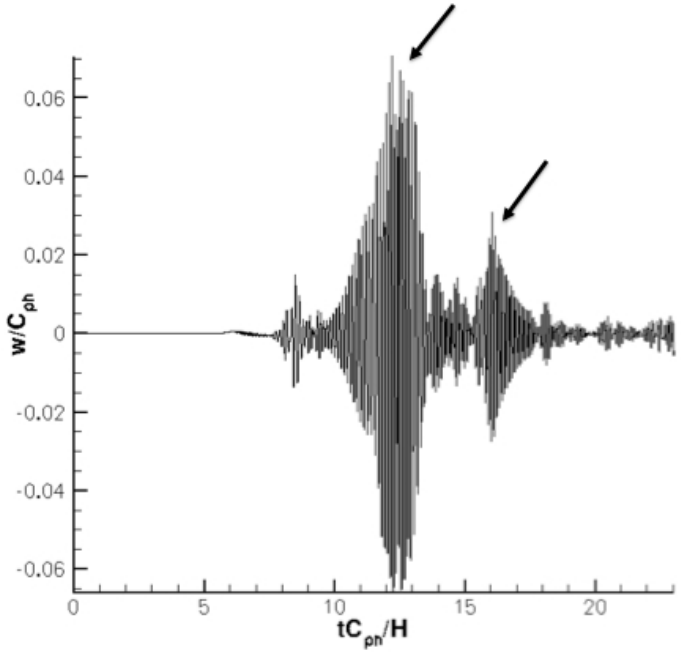

Figure 3.29: Near-bed vertical perturbation velocities obtained by a virtual point sensor located at $x/H = 20.6$ and $z/H = 0.02$, translating with the wave phase speed. The first arrow indicates the initial instability packet "triggered" by the noise, while the second arrow points the intermittent instability packet.

The case tested was the one that corresponds to a wave amplitude $\eta_{max}/H = 0.37$, Reynolds number $Re_w = 100,000$ and current strength $U_c/C_{ph} = 0.4$, which, according to the stability boundary diagram (Figure 3.22), is marginally stable. The noise was inserted at $tC_{ph}/H = 6.2$ and, at $tC_{ph}/H = 8.9$, the first packet of instability waves appears in the BBL(Figure 3.30 (a)), while the first train of Kelvin-Helmholtz billows (convective instability) is observed at $tC_{ph}/H = 10.7$ (Figure 3.30 (b)).

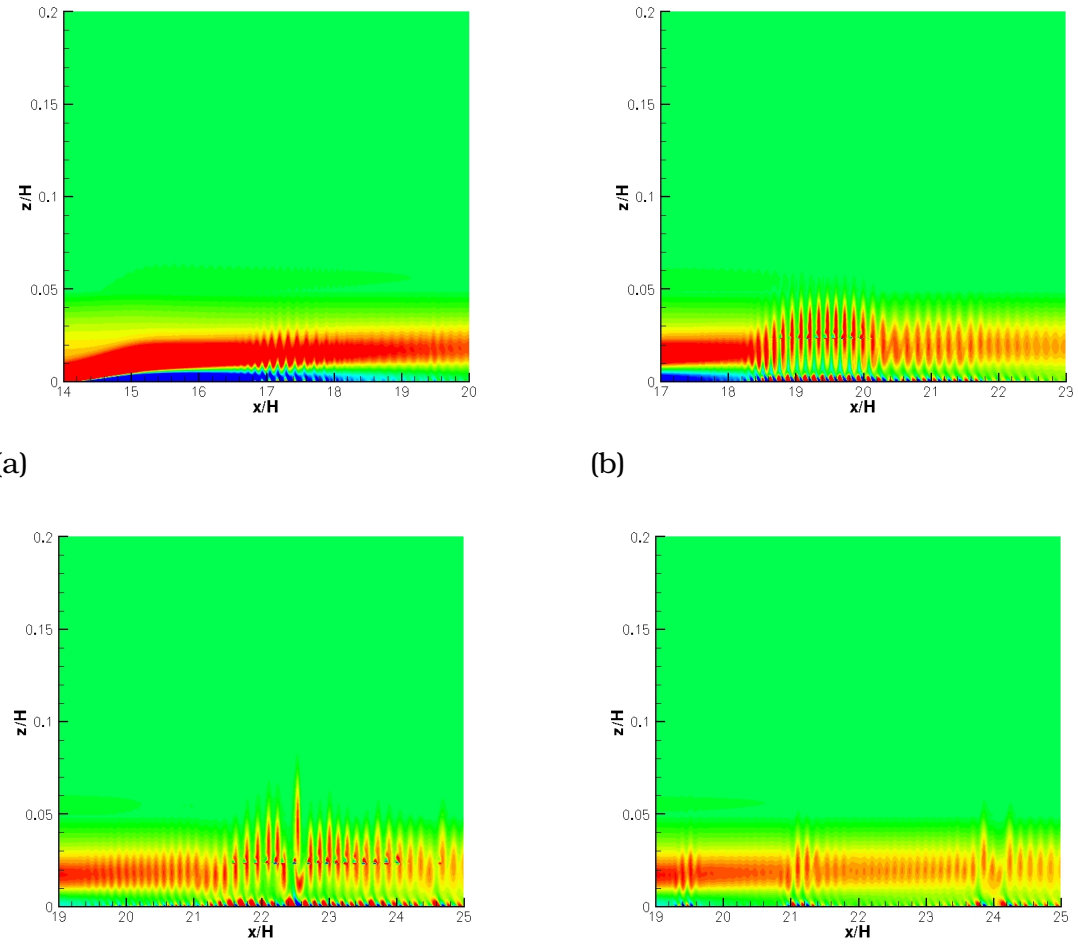

Figure 3.30: Snapshots of the BBL vorticity field after noise insertion: First instability packet (convective instability) appears at $tC_{ph}/H = 8.9$ (a), Kelvin-Helmholtz billows form at $tC_{ph}/H = 10.7$ (b), thenjump higher in the water column at $tC_{ph}/H = 13.3$ (c) and the intermittent vortex shedding continues (global instability) at $tC_{ph}/H = 18.1$ (d).

Then, instability waves are released, owing their existence to global instability, which contrary to the primary ones, are less in number and have smaller size (Figure 3.30 (d)). Similarly to the unperturbed cases, one can observe that the vortex shedding events are interrupted by inactive periods, again denoting the intermittent nature of the instability.

In Figure 3.29 near-bed vertical perturbation velocities are recorded by a virtual point sensor located at $x/H = 20.6$ and $z/H = 0.02$, translating with the wave phase speed. The first packet of Kelvin-Helmholtz instabilities triggered by the inserted noise, induce near-bed vertical velocities which assume values up to 7% of the wave phase speed. The shedding of secondary vortices leads to recorded values of maximum 3% of the wave phase speed because the size and the strength of the vortices is smaller than the equivalent of the primary ones.

CHAPTER 4

DISCUSSION

4.1 Stability Boundary

The current study has stimulated questions about the interpretation of the results, the comparison of the numerical simulations findings with the data obtained by laboratory experiments [18] [19] and the implications of the current study for field observations. To begin with, this is the first time that the BBL under a NLIW of depression propagating contrary to an oncoming barotropic current is studied. The presence of a background current provides additional shear to the flow reversal driven by the wave-induced adverse pressure gradient in the trailing edge of a wave of depression, but also enables a more localized separation region in the wave rear by enhancing BBL re-attachment, thus strongly increasing the potential for instability in the wave footprint (see Figure 3.3 and Figure 3.5 (top)). The characteristic thickness of the current-driven BBL (5% of H) was chosen approximately equal to the thickness of the wave-induced BBL and it is comparable to the values observed in the oceanic tidally-driven currents [101].

The critical wave amplitude for instability was found to decrease with increasing wave Reynolds number, since the greater Reynolds number values resulted in a thinner separation region and thus more shear. An increase in wave amplitude results in a stronger adverse pressure gradient, which enhances flow reversal in the wave-induced BBL, thus rendering the BBL more susceptible to global instability. Another inter-

esting finding is that the critical wave amplitude decreases with deeper thermocline. This might be attributed to the fact that when the thermocline is deeper, the trough of the wave lies closer to the bottom, thus inducing stronger adverse pressure gradient at the bottom than a wave of the same amplitude but with a shallower thermocline region. However, in order to answer that more detail is needed on the NLIW-induced pressure field.

The global instability is threshold dependent, which means that subcritical wave amplitudes will not produce any instabilities. At lower Reynolds numbers, instabilities do not develop because the growth rate of the global instability is extremely slow and the wave amplitude required to excite instabilities is beyond the conjugate state limit. Note that exploration of higher Reynolds number values was not possible because of resolution restrictions. Too much resolution had to be spent on inactive regions of the flow.

4.2 Intermittency

The global instability in the wave-induced BBL and the subsequent coherent vortex shedding are self-sustained (no external forcing is required) and show intermittency in time. Consequently, there might be a connection between the intermittent sand waves observed in the wave footprint in the rear of depression waves (Figure 1.7) and the BBL instabilities observed in our simulations, even though it is unclear whether these sand waves are formed immediately upon the passage of a sin-

gle NLIW or the repeated passage of multiple waves. Furthermore, the observed vortices and accompanying near-bed w-velocities and bottom shear stresses may be a driving factor in the formation of nepheloid layers observed in the wave footprint (Figure 1.7) and any benthic excitation and mixing in the coastal ocean and lakes, with all the implications it has for aquatic biology, industrial applications such as waste disposal and of course sound scattering and light attenuation, which could affect radars, sonars and other measuring devices.

Intermittent vortex shedding is also observed during numerical simulations of laminar separated boundary layer (LSBL) behind a topographical bump [29] or in the 3-D LSBL of airfoils [2] at moderate Reynolds numbers and is called boundary layer "bursting", "breathing" or "flapping". The vortex shedding in these cases is found to depend on the height of the bump or the angle of attack, which set the extent of flow reversal and the vortex shedding is found to begin at the region close to the reattachment point of the separation bubble similarly to what is observed in our simulations. Experimental investigation of 3-D separation bubbles on a flat plate [56] have also shown intermittent slow bursting (may be a slow global mode) which becomes more intense with increasing Reynolds number, while at small Re values the separation bubble remained stable. Consequently, BBL breathing is not only a 2-D phenomenon but can also occur in 3-D.

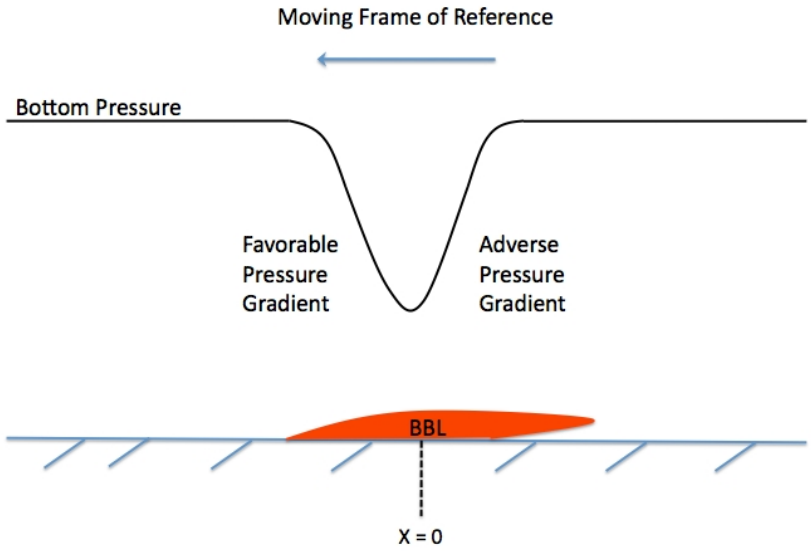

(a)

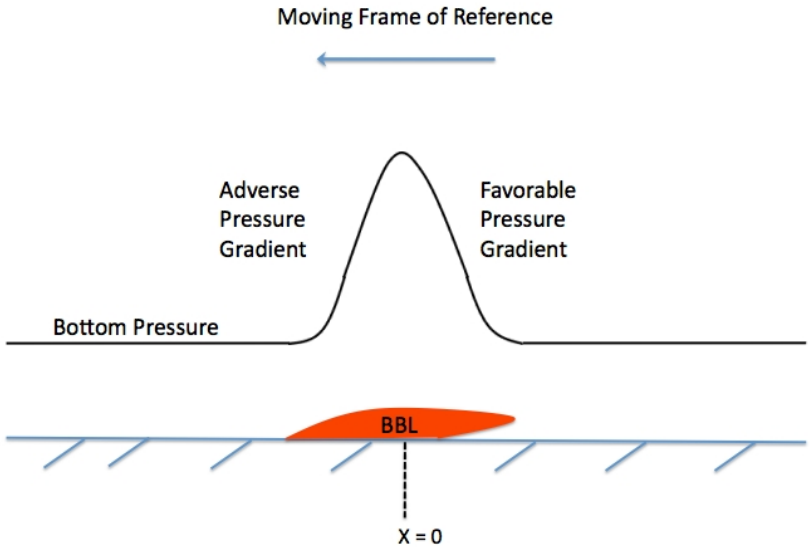

(b)

Figure 4.1: Schematic comparison of the bottom pressure and the BBL under a depression (a) and an elevation (b) wave. The BBL under the depression wave starts to develop in the favorable pressure gradient region before it enters the adverse pressure gradient region which will cause the BBL to separate. In the case of the elevation wave, the BBL starts to develop directly in the adverse pressure gradient region.

4.3 Role of Upstream BBL Conditions

Previous studies [9] [26] have conjectured that a sufficiently strong adverse pressure gradient is responsible for the onset of global BBL instabilities. However, our simulations of elevation waves, together with the results from the recent laboratory experiments of Carr & Davies [18], seem to question the notion that the adverse pressure gradient is the sole driver of the wave-induced BBL instabilities. The difference between elevation and depression waves is that in the latter, the wave-induced BBL has already developed before it reaches the adverse pressure gradient region, which does not happen in the case of elevation waves (Figure 4.1). This is confirmed both by our work and the work of Stastna & Lamb [91]. However, a current guarantees a fully developed boundary layer from the leading edge of the wave (Figure 4.2). Furthermore, the strength and structure of the oncoming current play an important role on the stability of the BBL and so do in general the upstream conditions as it is shown by the simulation of the two wave-train, which implies that oncoming turbulence may be a destabilizing factor of the NLIW-induced BBL. Hence, the above suggest that the wave-induced BBL instabilities do not only rely on the strength of the adverse pressure gradient but also depend on the upstream flow structure as dictated by a leading NLIW or current.

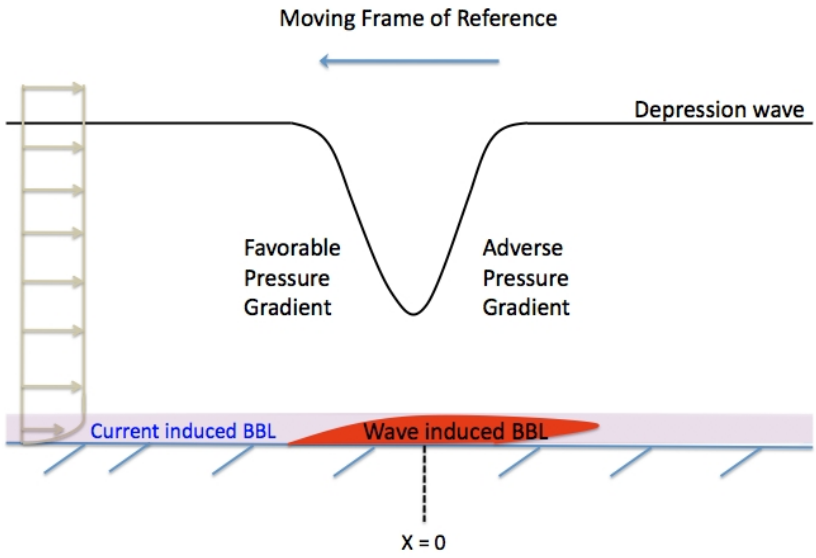

(a)

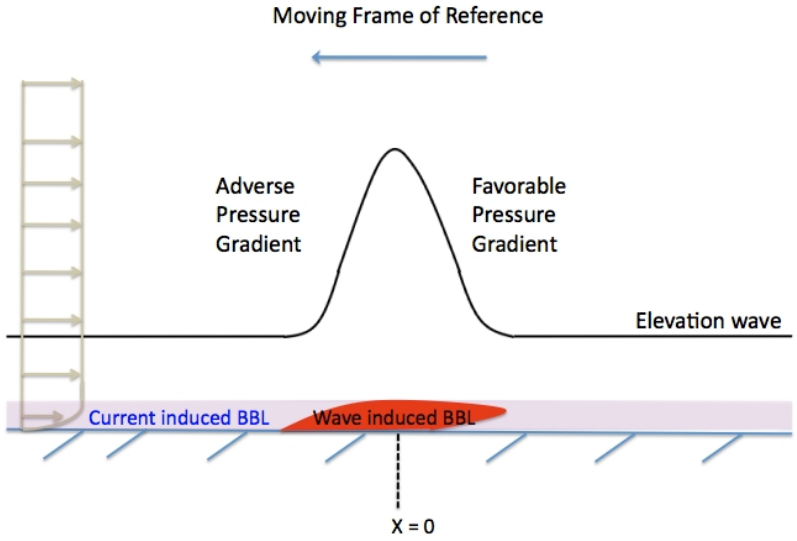

(b)

Figure 4.2: Schematic comparison of the current-induced and wave-induced BBL under a depression (a) and an elevation (b) wave. The current guarantees a fully developed boundary layer from the leading edge of the wave.

4.4 Extrapolation to the Ocean

Extrapolating from Figure 3.22 to oceanically relevant Reynolds numbers, which are several orders of magnitude larger ($C_{ph} \approx 3\,m/sec$; $H = 600\,m$ [83]), it is very likely that near-bed instabilities and turbulence driven by the mechanism considered here can develop at even lower wave amplitudes. The spatial variability and magnitude of the recorded bottom shear stresses lead us to think that they might be sufficient to detach bottom sediment and in combination with the significant w-velocities, resuspend sediment to even greater height above the seafloor. The sensitivity of the wave-induced BBL to upstream conditions, which generally in nature contain considerable levels of turbulence, is evidenced by the simulation of the 2-wave scenario and the investigation of the noise insertion. Thus one might speculate near-bed instabilities and the resulting to 3-D turbulent structures may be found under waves of even lower amplitudes than those examined in Figure 3.22. We should emphasize that the coherent structures driven by this instability (even in 3-D) can be more efficient in sediment transport than bursts and sweeps of nominal BBL for two reasons: 1) The turbulent dynamics of the nominal BBL do not show any coherency in space and in time. 2) As it is observed from our simulations, in the wave driven benthic excitation, the coherent vortices are ejected to a certain height and reside there for the whole duration of the simulation.

Oceanographers so far had the misconception that the peak turbulence would occur underneath a depression wave, which is not true as it is clearly seen from our simulations (vortex shedding is observed at the

wave footprint in the rear of the wave). For example Klymak & Moum [55] suggest that the location of the peak turbulence would coincide with the location of the maximum near-bottom velocity, which is underneath the NLIW.

Furthermore, we have identified that the vortex shedding signature on a stationary vertical ADV array would consist of vertical velocities which would have 180^0 vertical phase difference between the lower sensors and the ones that are positioned higher in the water column. This vortex shedding signature can be found in the observations by Bogucki et al. [12]. The vortex shedding signature expected to be recorded by an autonomous underwater vehicle (AUV) translating with the wave phase speed close to the bottom consists of oscillating at a frequency $tC_{ph}/H \approx 0.15$ vertical velocities, which would assume values an order of magnitude smaller than the wave phase speed. The approximate along wave propagation spacing of instruments that must be deployed to avoid missing intermittent bursts is a difficult topic because the spacing of the instability packets in our simulations depends on the amount of shear between the separated flow and the outer flow, with high sheared flows giving rise to more densely spaced instability packets. To offer some typical values, for the base case, the spacing of instability packets ranged between $x/H = 0$ and $x/H = 3.5$.

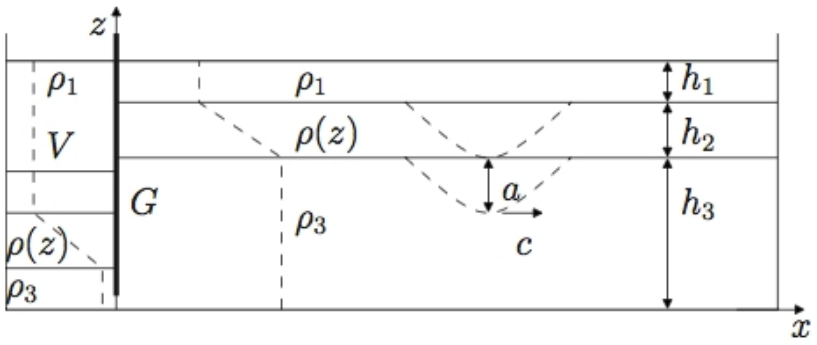

Figure 4.3: Schematic of the experimental setup applied by Carr et al. [19]. The sudden opening of the gate G could produce noise which could destabilize the wave-induced BBL at lower amplitudes than those predicted by our stability boundary (Figure 3.22).

4.5 Comparison with Laboratory Experiments

Comparison of the structure of the shed vortices under waves of depression between the simulations (Figure 3.7) and the laboratory experiments [19] (Figure 3.8) shows qualitative agreement. However, in the laboratory, the critical wave amplitude for a given Re_w and h_1/h_2 is found to be significantly lower. The exact explanation is not known, but a plausible hypothesis is that during the wave initialization and by the sudden opening of the gate, noise is generated which could destabilize the BBL and lead to instability development at even lower amplitudes. Another possible explanation is that during wave initialization, the initial waveform is steeper, resulting in a stronger adverse pressure gradient which could drive BBL instabilities even though the steady state wave is subcritical. One more possibility is that the three-dimensionality of the laboratory experiments could affect the stability of BBL. The threshold

amplitude of the instability might be lowered in a 3-D environment because the 3-D mode grows faster than a 2-D for this case [52]. Finally, the claim of quiescent background flow conditions during the laboratory experiments might not hold. The opening of the gate (Figure 4.3) may resulted in an oncoming current, as heavier fluid (density: ρ_3) replaced the lighter fluid (densities: ρ_1 and $\rho(z)$) which would settle at lower depth after the gate opening.

CHAPTER 5

CONCLUSIONS AND FUTURE WORK

5.1 Summary of Conclusions

The bottom boundary layer induced by NLIWs has been investigated using 2-D direct numerical simulations via a spectral multidomain penalty method model. Fourier spectral discretization is used in the horizontal direction and a Legendre multidomain spectral scheme is applied in the vertical direction. Both waves of depression and elevation were examined. The depression waves were propagating against oncoming barotropic current. The waveform was taken as the steady state solution of a fully nonlinear higher order KdV equation (Appendix A). The stability and characteristics of the wave-induced BBL were examined for values of Re_w as high as 100,000.

Self-sustained BBL global instabilities and intermittent vortex shedding were found to occur in the rear of depression waves for $Re_w > 60,000$ when the combined effect of the adverse pressure gradient and the barotropic current resulted in a sufficiently strong reversed near-bottom flow behind the wave trough. The strength of the adverse pressure gradient is determined by the wave amplitude. The critical wave amplitude above which instability occurs reduces with increasing Re_w, oncoming current strength and deeper thermocline. However, no instabilities were observed in the absence of an oncoming current. The instability appears close to the reattachment point of the separation bubble and imposes its own wavelength and frequency. As the instability devel-

ops, the separation bubble is partially broken down into a sequence of coherent vortices (5-12) which are ejected up to a maximum height that corresponds to approximately 8% of the total depth. Underneath the instabilities-vortices there are always pockets of alternating positive and negative vorticity at the bottom, which propagate at the same speed with the instabilities, approximately 15% greater than the wave phase speed. The presence of instabilities-vortices results in enhanced values of bottom shear stress and significant vertical velocities (up to 12% of C_{ph}), which suggests that the NLIW-induced BBL instability can be a driving mechanism for sediment resuspension in the coastal ocean and in lakes. Our results are in qualitative agreement with the laboratory experiments performed by Carr et al. [19]. The two-wave scenario and the insertion of external noise have proven that the stability of the NLIW-induced BBL depends on the upstream flow conditions and that instability development at lower amplitudes than those predicted by the stability boundary diagram is possible.

For the case of elevation waves, in most simulations the wave-induced BBL remained stable and no vortex shedding was observed, similarly to Carr et al. [18]. However, we remain intrigued by the observation of core formation and accompanied baroclinc generation of vorticity resulting in Kelvin-Helmholtz billows reaching a height equal to half the wave-guide depth in some of the cases (Figure 3.2). These Kelvin-Helmholtz billows cause a thermoclinic deformation which appears to be similar with the deformation observed in the simulations of Stastna & Lamb [92] or the simulations of Bogucki & Redekopp [10]. However, in their case the deformation was claimed to be due to ejected vortices

from the BBL. Nevertheless, since in the current study the waveform is forced to be frozen in time, the core formation should be dealt with scepticism and is prone to criticism. Further investigation is needed using non-frozen fully nonlinear waves.

5.2 Future Work

Even though the current study shed some light on the NLIW-induced BBL excitation, there are still open questions that need to be addressed. Firstly, the core formation under waves of elevation needs to be further investigated in a spatially evolving simulation. To this end, the wave should not be frozen in time and should be left freely to evolve. In order to study the core formation under an elevation wave, a spatially evolving simulation is needed with non-periodic lateral boundary conditions. Thus, a quadrilateral multidomain penalty method model should be developed.

Another aspect that needs to be further studied is whether wave-induced BBL instabilities could appear in the absence of an oncoming current at higher Re_w values. However, augmenting Re_w values implies also increased resolution, since the scale separation between the length-scale of the wave and the legthscale of the instabilities would increase, which would make the computational cost prohibiting. In order to deal with that, one could focus the computational domain on the region underneath the wave and prevent expending resolution on the non-active parts of the flow. By doing so, 3-D simulations can also be performed,

in order to investigate: a) whether transverse BBL instabilities form, b) how they alter the view of the primary NLIW-induced BBL instabilities and their 2-D structure, observed in the current study and c) whether the vortex shedding retains its intermittent character or it becomes continuous in 3-D.

However, confining the computational domain in the adverse pressure gradient region is not trivial. A subgrid scale model (SGS) [78] and a wall model is needed, although there is not such model which deals with both forward and adverse pressure gradient flows. If we want to simulate three-dimensional separated boundary layer flows at high Reynolds numbers, and at the same time keep a rational computational cost, we have to apply wall modeled large eddy simulations (WMLES) [80], by resolving the integral lengthscales and modeling the smaller scales in the inner layer. A careful design of the inflow and outflow conditions should also be made. If the computational domain starts just before the favorable pressure gradient region (depression wave), the sole lateral inflow would be the current-induced BBL. Since we do not want to have any vortices re-entering the computational domain, sponge layers could be used in the right lateral boundary in order to zero the outflowing velocity and density field.

We also propose to employ a Lagrangian particle tracking algorithm tailored for high-order spectral multidomain simulations, developed by Jacobs et al. [50], to assess the capacity of a wave-induced benthic eruption to distribute sedimentary particles vertically in the water column. The approach will be to use spatio-temporal velocity fields ob-

tained from selected direct numerical simulations of the globally unstable, wave-induced boundary layer behind waves of depression as input. Then, two different arrangements of particles will be used as initial states. First, starting with a prescribed vertical array of particles of given mass ratio immediately upstream of a solitary wave, the residual (alt., differential) vertical displacement of each particle in the ordered array will be computed as a function of time as the wave and associated unstable boundary layer flow pass by. Each particle will, of course, experience a differing horizontal displacement which is obtained as part of the computation. However, our primary interest is to assess the potential for the unstable boundary layer dynamics to lift particles to higher levels, and to determine whether there is a preference for forming layers or clouds of enhanced particle density behind a long wave, and the position of possible layers as a function of particle mass ratio and wave/environmental conditions. Such information should lead to definitive conclusions regarding the implications of wave-induced benthic processes to influence acoustical/optical properties and nutrient/biological transport. Second, we propose to place an array of particles at the lowest grid level of the benthic boundary layer and track the evolution of these particles as the wave-induced boundary layer develops and becomes unstable. The objective is to ascertain what particle distribution (cloud) is created solely by boundary layer uplift.

The current study dealt only with NLIWs propagating over a flat bottom. Consequently, it is of interest to look at NLIWs propagating over a gently shoaling bottom topography as there is a lack of simulations investigating this process. Such simulations might reveal the mecha-

nism driving NLIW polarity change, which is poorly understood. Polarity change is the transformation of a depression wave to an elevation wave through the process of NLIW shoaling. As the NLIW shoals, the thermocline which was originally closer to the surface (NLIW of depression), at some point starts lying closer to the bottom and then the KdV equation predicts an elevation wave. Moreover, a variable topography in x-direction will result in a variable shear and stratification, which will cause a continuous change of the adverse pressure gradient. Furthermore, by simulating the full evolution of a NLIW from generation to shoaling and then to breaking, one could estimate the energy dissipation during that process, which could be used as parameterization to Global Circulation Models (GCMs). In order to deal with gently shoaling topography, without loosing the spectral accuracy of the model in the horizontal direction, a quadrilateral spectral multidomain penalty method model should be developed.

APPENDIX A

FULL-RANGE, CUBIC APPROXIMATION WITH NONLINEAR DISPERSION, HIGHER ORDER KDV EQUATION

The fully nonlinear evolution of long waves along a single characteristic can be written as:

$$\eta_t + c_0\tilde{c}_E(\tilde{\eta})\eta_x + \beta_0 c_0 \left(\tilde{\beta}(\tilde{\eta})\tilde{c}_E(\tilde{\eta})\eta_{xx}\right)_x = 0 \tag{A.1}$$

with $\tilde{c}_E$ the non-dimensional nonlinear phase speed given by:

$$\tilde{c}_E = \frac{c_E}{c_0} = 1 - 3(\epsilon + \tilde{\eta})^2 + 3\epsilon(\epsilon + \tilde{\eta})\sqrt{\frac{1 - (\epsilon + \tilde{\eta})^2}{1 - \epsilon^2}} \tag{A.2}$$

where $\tilde{\eta} = 2\eta/H$ and $\epsilon = (h_2 - h_1)/H$ (H is the total depth)

$$\tilde{\beta}(\tilde{\eta}) = \frac{(h_1 - \eta)(h_2 + \eta)}{h_1 h_2} = \frac{1 - (\epsilon + \tilde{\eta})^2}{1 - \epsilon^2} \tag{A.3}$$

In the above c_0 is the linear phase speed given by Eq. 1.5 and $\beta_0 = \beta/c_0$ where β is given by Eq. 1.8.

APPENDIX B

NLIW VELOCITY AND DENSITY FIELDS

The current appendix deals with the NLIW density velocity fields and their gradients in a two-layer system with a prescribed thermoclinic displacement function $\eta(x)$. The density interface is positioned at $z = -1$, which is non-dimensionalized with h_1 (figure B.1) and the thickness of the thermocline is $2\delta_\rho$ (figure B.2). A local, normalized with the thermocline thickness, coordinate perpendicular to the density interface is defined as such:

$$\theta(x\,,\,z) = \frac{z - (-1 + \eta(x))}{\delta_\rho} \tag{B.1}$$

The total density as a function of position $(x\,,\,z)$ is:

$$\rho(x\,,\,z) = \frac{\rho_2 + \rho_1}{2} - \frac{\rho_2 - \rho_1}{2}\, tanh\,\theta(x\,,\,z) \tag{B.2}$$

Boussinesq approximation:

$$\rho(x\,,\,z) = \rho_0 + \rho_w(x\,,\,z) + \bar{\rho}(z) \;\longrightarrow\; \text{We do not consider } \rho_0 \tag{B.3}$$

Its gradients are:

$$\frac{\partial \rho}{\partial x} = \frac{\rho_2 - \rho_1}{2\delta_\rho}\,\frac{\partial \eta}{\partial x}\, sech^2\,\theta(x\,,\,z) \tag{B.4}$$

$$\frac{\partial \rho}{\partial z} = -\frac{\rho_2 - \rho_1}{2\delta_\rho}\, sech^2\,\theta(x\,,\,z) \tag{B.5}$$

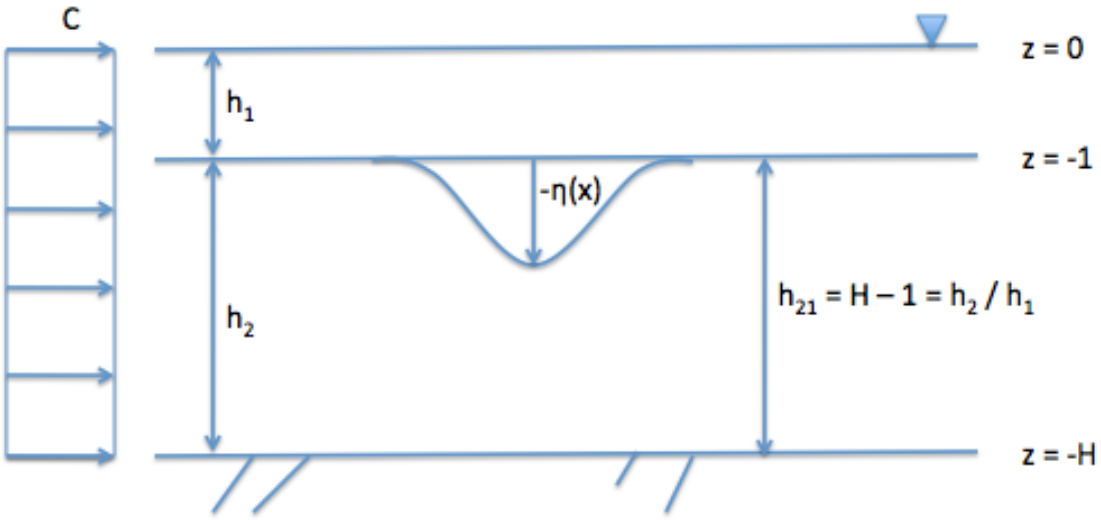

Figure B.1: Schematic of the coordinates and positioning of the NLIW.

The ambient density field may be found when setting $\eta(x) = 0$:

$$\theta(z) = \frac{z+1}{\delta_\rho} \tag{B.6}$$

$$\bar{\rho}(z) = \frac{\rho_2 + \rho_1}{2} - \frac{\rho_2 - \rho_1}{2} \tanh \theta(z) \tag{B.7}$$

$$\frac{\partial \bar{\rho}}{\partial x} = 0 \tag{B.8}$$

$$\frac{\partial \bar{\rho}}{\partial z} = -\frac{\rho_2 - \rho_1}{2\delta_\rho} \operatorname{sech}^2 \theta(z) \tag{B.9}$$

But the decomposition of the total density field is given by:

$$\rho = \bar{\rho} + \rho_w \Rightarrow \rho_w = \rho - \bar{\rho} \tag{B.10}$$

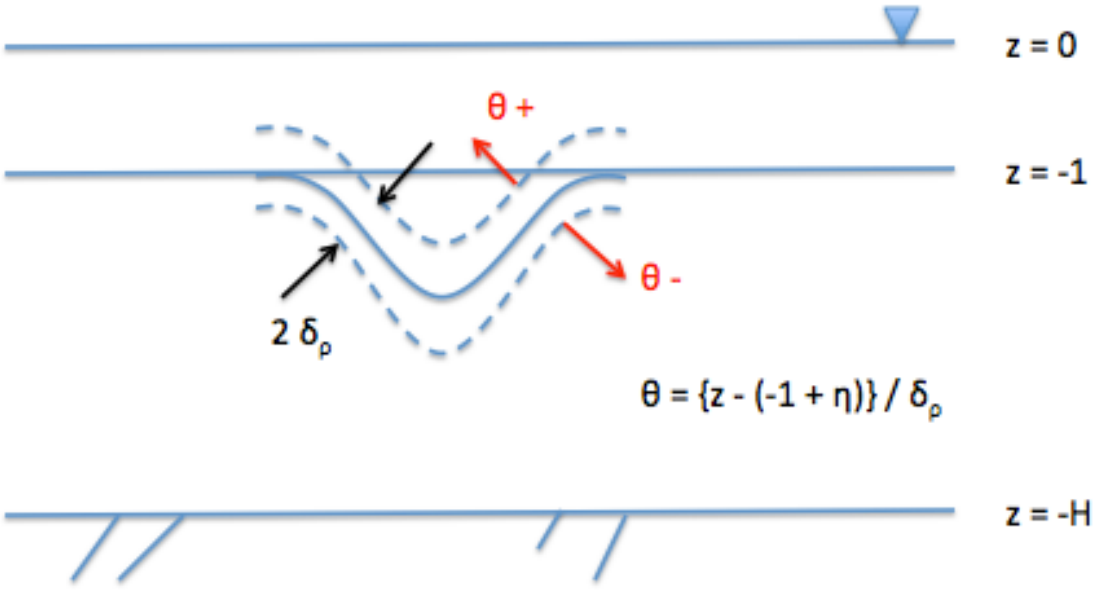

Figure B.2: Schematic of the thermocline and the local coordinate θ.

Consequently:

$$\rho_w = -\frac{\rho_2 - \rho_1}{2}\left[\tanh\theta(x\,,\,z) - \tanh\theta(z)\right] \tag{B.11}$$

$$\frac{\partial\rho_w}{\partial x} = \frac{\partial\rho}{\partial x} = \frac{\rho_2 - \rho_1}{2\delta_\rho}\frac{\partial\eta}{\partial x}\,sech^2\,\theta(x\,,\,z) \tag{B.12}$$

$$\frac{\partial\rho_w}{\partial z} = \frac{\partial\rho}{\partial z} - \frac{\partial\bar{\rho}}{\partial z} = -\frac{\rho_2 - \rho_1}{2\delta_\rho}\left[sech^2\,\theta(x\,,\,z) - sech^2\,\theta(z)\right] \tag{B.13}$$

The Brunt-Väisälä frequency profile is:

$$N^2(z) = -\frac{g}{\rho_0}\frac{\partial\bar{\rho}}{\partial z} = -\frac{g}{\rho_0}\left[-\frac{\rho_2 - \rho_1}{2\delta_\rho}\,sech^2\,\theta(z)\right] \tag{B.14}$$

For the horizontal wave velocity field we know from internal wave theory [64] that:

$$u_w(x\,,\,z) = \frac{c}{2}\bar{\bar{S}} + \frac{c}{2}\bar{\bar{D}}\tanh\theta(x\,,\,z) \tag{B.15}$$

where:

$$\theta(x\,,\,z) = \frac{z-(-1+\eta(x))}{\delta} \tag{B.16}$$

$$\bar{\bar{S}} = \frac{1}{1-\eta(x)} + \frac{h_{21}}{h_{21}+\eta(x)} \tag{B.17}$$

$$\bar{\bar{D}} = \frac{1}{1-\eta(x)} - \frac{h_{21}}{h_{21}+\eta(x)} \tag{B.18}$$

Thus:

$$\frac{\partial u_w}{\partial x} = \frac{c}{2}\frac{\partial \bar{\bar{S}}}{\partial x} + \frac{c}{2}\frac{\partial \bar{\bar{D}}}{\partial x}\,tanh\,\theta(x\,,\,z) - \frac{c}{2\delta}\,\bar{\bar{D}}\,\frac{\partial \eta}{\partial x}\,sech^2\,\theta(x\,,\,z) \tag{B.19}$$

$$\frac{\partial u_w}{\partial z} = \frac{c}{2\delta}\,\bar{\bar{D}}\,sech^2\,\theta(x\,,\,z) \tag{B.20}$$

Where:

$$\frac{\partial \bar{\bar{S}}}{\partial x} = \frac{\partial \eta}{\partial x}\left[\frac{1}{(1-\eta(x))^2} - \frac{h_{21}}{(h_{21}+\eta(x))^2}\right] \tag{B.21}$$

$$\frac{\partial \bar{\bar{D}}}{\partial x} = \frac{\partial \eta}{\partial x}\left[\frac{1}{(1-\eta(x))^2} + \frac{h_{21}}{(h_{21}+\eta(x))^2}\right] \tag{B.22}$$

From Continuity we have:

$$\frac{\partial w_w}{\partial z} = -\frac{\partial u_w}{\partial x} \tag{B.23}$$

$$w_w(x\,,\,z) = -\int_{-H}^{z}\frac{\partial u_w}{\partial x}\,dz =$$

$$= -\frac{c}{2}\int_{-H}^{z}\frac{\partial \bar{\bar{S}}}{\partial x}\,dz - \frac{c}{2}\int_{-H}^{z}\frac{\partial \bar{\bar{D}}}{\partial x}\,tanh\,\theta(x\,,\,z)\,dz +$$

$$\frac{c}{2\delta}\,\bar{\bar{D}}\,\frac{\partial \eta}{\partial x}\int_{-H}^{z}sech^2\,\theta(x\,,\,z)dz =$$

$$= -\frac{c}{2}\frac{\partial \bar{\bar{S}}}{\partial x}(z+H) - \frac{c\,\delta}{2}\frac{\partial \bar{\bar{D}}}{\partial x}\,ln\left[\frac{cosh\,\theta(x\,,\,z)}{cosh\,\theta(x\,,\,H)}\right] +$$

$$\frac{c}{2}\,\bar{\bar{D}}\,\frac{\partial \eta}{\partial x}\,[tanh\,\theta(x\,,\,z) - tanh\,\theta(x\,,\,H)] \tag{B.24}$$

BIBLIOGRAPHY

[1] P. Aghsaee, L. Boegman, and K. G. Lamb. Breaking of shoaling internal solitary waves. *J. Fluid Mech.*, submitted, 2010.

[2] J. H. Almutairi, L. E. Jones, and N. D. Sandham. Intermittent Bursting of a Laminar Separation Bubble on an Airfoil. *AIAA Journal*, 48:414–426, February 2010.

[3] J. R. Apel. *Principles of Ocean Physics*. Academic Press, Ltd, 1987.

[4] J. R. Apel, J. R. Proni, and R. L. Charnell. Observations of oceanic internal and surface waves from earth resources technology satellite. *J. Geophys. Res.*, 80:865–881, 1975.

[5] John R. Apel, Lev A. Ostrovsky, and Yuri A. Stepanyants. Internal solitons in the ocean. *The Journal of the Acoustical Society of America*, 98(5):2863–2864, 1995.

[6] J. Bloesch. A review of methods used to measure sediment resuspension. *Hydrobiologia*, 284:13–18, 1994.

[7] L. Boegman, J. Imberger, G. N. Ivey, and J. P. Antenucci. High-frequency internal waves in large stratified lakes. *Limnol. Oceanogr.*, 48(2):895–919, 2003.

[8] L. Boegman and G. N. Ivey. Flow separation and resuspension beneath shoaling nonlinear internal waves. *J. Geophys. Res.*, 114, 2009.

[9] D. Bogucki, T. Dickey, and L. G. Redekopp. Sediment resuspension and mixing by resonantly generated internal solitary waves. *J. Phys. Oceanogr.*, 27:1181–1196, 1997.

[10] D. Bogucki and L. G. Redekopp. A mechanism for sediment resuspension by internal solitary waves. *Geophys. Res. Lett.*, 26:1317–1320, 1999.

[11] D. Bogucki and L. G. Redekopp. Climate of long internal waves and resuspension on the coastal shelf. *Oceanologia*, 50:5–21, 2008.

[12] D. Bogucki, L. G. Redekopp, and J. Barth. Internal solitary waves in the Coastal Mixing and Optics Experiment 1996: Multimodal structure and resuspension. *J. Geophys. Res.*, 110(C2):Art. No. C02024, 2005.

[13] J. P. Boyd. *Chebyshev and Fourier Spectral Methods*. Dover, Mineola, New York, 2001.

[14] J. P. Boyd. Chebyshev solution of the near-singular one-dimensional Helmholtz equation and related singular perturbation equations: Multiple scale series, exact particular integral for polynomial forcing, asymptotic Chebyshev coefficients of the exponential function and boundary layer rule of thumb. *Numerical Algorithms*, 38:197–207, 2005.

[15] D. L. Boyer, D. B. Haidvogel, and N. Perenne. Laboratory-numerical model comparisons of canyon flows: A parameter study. *J. Phys. Oceanogr.*, 34(7):1588–1609, 2004.

[16] B. Butman, P. S. Alexander, A. Scotti, R. C. Beardsley, and S. P. Anderson. Large internal waves in Massachusetts Bay transport

sediments offshore. *Continental Shelf Research.*, 26:2029–2049, 2007.

[17] M. Carr and P. A. Davies. The motion of an internal solitary wave of depression over a fixed bottom boundary in a shallow two-layer fluid. *Phys. Fluids*, 18(1):Art. No. 016601, 2006.

[18] M. Carr and P. A. Davies. Boundary layer flow beneath an internal solitary wave of elevation. *Phys. Fluids*, 22(2):026601, 2010.

[19] M. Carr, P. A. Davies, and P. Shivaram. Experimental evidence of internal solitary wave-induced global instability in shallow water benthic boundary layers. *Phys. Fluids*, 20(1):Art. No. 066603, 2008.

[20] W. Choi and R. Camassa. Fully nonlinear internal waves in a two-fluid system. *Journal of Fluid Mechanics*, 396(-1):1–36, 1999.

[21] J. M. Chomaz. Transition to turbulence in open flows: what linear and fully nonlinear local and global theories tell us. *Europ. J. Mech. B-Fluids*, 23:385–399, 2004.

[22] D. R. Christie. The Morning Glory of the Gulf of Carpentaria: A paradigm for non-linear waves in the lower atmoshere. *Aust. Meteorol. Mag.*, 41:21–60, 1992.

[23] R. E. Davis and A. Acrivos. Solitary waves in deep water. *J. Fluid Mech.*, 29:593–601, 1967.

[24] M. O. Deville, P. F. Fischer, and E. H. Mund. *High Order Methods for Incompressible Fluid Flow*. Cambridge University Press, 2002.

[25] P. J. Diamessis, J. A. Domaradzki, and J. S. Hesthaven. A spectral multidomain penalty method model for the simulation of high Reynolds number localized stratified turbulence. *J. Comput. Phys.*, 202:298–322, 2005.

[26] P. J. Diamessis and L. G. Redekopp. Numerical investigation of solitary internal wave-induced global instability in shallow water benthic boundary layers. *J. Phys. Oceanogr.*, 36(5):784–812, 2006.

[27] V. D. Djordjevic and L. G. Redekopp. The fission and disintegration of internal solitary waves moving over two-dimensional topography. *J. Phys. Oceanogr.*, 8:1016–1024, 1978.

[28] W. S. Don, D. Gottlieb, and J. H. Jung. A multidomain spectral method for supersonic reactive flows. *J. Comput. Phys.*, 192:325–354, 2003.

[29] U. Ehrenstein and F. Gallaire. Two-dimensional global low-frequency oscillations in a separating boundary-layer flow. *Journal of Fluid Mechanics*, 614(-1):315–327, 2008.

[30] D.M. Farmer. Observations of long nonlinear internal waves in a lake. *J. Phys. Oceanogr.*, 8:63–73, 1978.

[31] D.M. Farmer and L. Armi. The generation and trapping of solitary waves over topography. *Science*, 283:188–190, 1999.

[32] Clifford S. Gardner, John M. Greene, Martin D. Kruskal, and Robert M. Miura. Method for solving the Korteweg-deVries Equation. *Phys. Rev. Lett.*, 19(19):1095–1097, Nov 1967.

[33] D. Gottlieb and J. S. Hesthaven. Spectral methods for hyperbolic problems. *Journal of Computational and Applied Mathematics*, 128:83–131, 2001.

[34] W. D. Grant and O. S. Madsen. The continental-shelf bottom boundary layer. *Ann. Rev. Fluid Mech.*, 18:265–305, 1986.

[35] R. Grimshaw, E. Pelinovsky, and O. Poloukhina. Higher-order korteweg-de vries models for internal solitary waves in a stratified shear flow with a free surface. *Nonlin. Processes in Geophys.*, 9:221–235, 2002.

[36] R. H. J. Grimshaw. Evolution equations for weakly nonlinear, long internal waves in a rotating fluid. *Stud. Appl. Math.*, 73:1–33, 1985.

[37] R. H. J. Grimshaw, L. A. Ostrovsky, V. I. Shrira, and Yu. A. Stepanyants. Long nonlinear surface and internal waves in a rotating ocean. *Surv. Geophys.*, 19:289–338, 1998.

[38] J. L. Guermond and J. Shen. Velocity-correction projection methods for incompressible flows. *SIAM J. Numer. Anal.*, 41(1):112–134, 2003.

[39] Y. Guo, J. K. Sveen, P. A. Davies, J. Grue, and P. Dong. Modeling the motion of an internal solitary wave over a bottom ridge in a stratified fluid. *Environmental Fluid Mechanics*, 4:415–441, 2004.

[40] D. Halpern. Observations of short period internal waves in Massachusetts Bay. *J. Mar. Res.*, 29:116–132, 1971.

[41] D.A. Hammond and L.G. Redekopp. Local and global instability properties of separation bubbles. *Eur. J. Mech. B Fluids*, 17:145–164, 1998.

[42] K. R. Helfrich. Internal solitary wave breaking and run-up on a uniform slope. *J. Fluid Mech.*, 243:133–154, 1992.

[43] K. R. Helfrich and W. K. Melville. Long non-linear internal waves. *Ann. Rev. Fluid Mech.*, 38:395–425, 2006.

[44] J. S. Hesthaven. A stable penalty method for the compressible Navier-Stokes equations: II. One-dimensional domain decomposition schemes. *SIAM J. Sci. Comput.*, 18(3):658–685, 1997.

[45] J. S. Hesthaven and D. Gottlieb. A stable penalty method for the compressible Navier-Stokes equations: I. Open boundary conditions. *SIAM J. Sci. Comput.*, 17(3):579–612, 1996.

[46] H. P. Horton. *Laminar separation bubbles in two- and three-dimensional incompressible flow*. PhD thesis, University of London, 1968.

[47] P Huerre and PA Monkewitz. Local and Global Instabilities in Spatially Developing Flows. *Ann. Rev. Fluid Mech.*, 22:473–537, 1990.

[48] P. Huerre and M. Rossi. Hydrodynamic instabilities in open flows. In C. Godreche and P. Manneville, editors, *Hydrodynamics and Nonlinear Instabilities*, pages 81–294. Cambridge University Press, 1998.

[49] K. Hunkins and M. Fliegel. Internal undular surges in Seneca Lake: A natural occurrence of solitons. *J. Geophys. Res.*, 78:539–548, 1982.

[50] G.B. Jacobs, D.A. Kopriva, and F. Mashayek. Towards efficient tracking of inertial particles with high-order multidomain methods. *Journal of Computational and Applied Mathematics*, 206(1):392 – 408, 2007.

[51] Tae-Chang Jo and Wooyoung Choi. Dynamics of strongly nonlinear internal solitary waves in shallow water. *Studies in Applied Mathematics*, 109:205–227(23), 2002.

[52] L. E. Jones, R. D. Sandberg, and N. D. Sandham. Direct numerical simulations of forced and unforced separation bubbles on an airfoil at incidence. *Journal of Fluid Mechanics*, 602(-1):175–207, 2008.

[53] Tsunehiko Kakutani and Nobuyoshi Yamasaki. Solitary waves on a two-layer fluid. *Journal of the Physical Society of Japan*, 45(2):674–679, 1978.

[54] G. E. Karniadakis, M. Israeli, and S. A. Orszag. High-order splitting methods for the incompressible Navier-Stokes equations. *J. Comput. Phys.*, 97:414–443, 1991.

[55] J. M. Klymak and J. N. Moum. Internal solitary waves of elevation advancing on a shoaling shelf. *Geophys. Res. Lett.*, 30(20):2045–2049, 2003.

[56] A. Kremheller and H. Fasel. Water tunnel experiments on three dimensional separation bubbles on a flat plate. In *40th Fluid Dynamics Conference and Exhibit*, 2010.

[57] P. K. Kundu and I. M. Cohen. *Fluid Mechanics*. Academic Press, San Diego, 2004.

[58] K. G. Lamb and B. Wan. Conjugate flows and flat solitary waves for a continuously stratified fluid. *Phys. Fluids*, 10:2061–2079, 1998.

[59] C. Y Lee and R. P Beardsley. The generation of long nonlinear internal waves in a weakly stratified shear flow. *J. Geophys. Res.*, 79(3):453–462, 1967.

[60] O. S. Lee. Observations of internal waves in shallow water. *Limnol. and Oceanogr.*, 6:312–321, 1961.

[61] J. J. Leichter, G. Shellenbarger, and S. R. Genovese. S. J., Wing. Breaking internal waves on a Florida (USA) coral reef: a plankton pump at work? *Marine Ecology - Progress Series*, 166:83–97, 1998.

[62] J. G. Levin, M. Iskandarani, and D. B. Haidvogel. A spectral filtering procedure for eddy-resolving simulations with a spectral element ocean model. *J. Comput. Phys.*, 137:130–154, 1997.

[63] R. R. Long. Some aspects of the flow of stratified fluids. i. a theoretical investigation. *Tellus*, 42:42–58, 1953.

[64] S. A. Maslowe and L. G. Redekopp. Long nonlinear waves in stratified shear flows. *J. Fluid Mech.*, 101:321–348, 1980.

[65] T. Maxworthy. A note on internal solitary waves produced by tidal flow over a three dimensional ridge. *J. Geophys. Res.*, 84:338–346, 1979.

[66] H. Michallet and E. Barthelémy. Experimental study of interfacial solitary waves. *Journal of Fluid Mechanics*, 366(-1):159–177, 1998.

[67] H. Michallet and G. N. Ivey. Experiments on mixing due to internal solitary waves breaking on uniform slopes. *J. Geophys. Res.*, 104(C6):13,467–13,477, 1999.

[68] J. W. Miles. On internal solitary waves. *Tellus*, 31:456–462, 1979.

[69] J. W. Miles. Solitary waves. *Ann. Rev. Fluid Mech.*, 12:11–43, 1980.

[70] Peter A. Monkewitz and Patrick Huerre. Influence of the velocity ratio on the spatial instability of mixing layers. *Phys. Fluids*, 25(7):1137–1143, 1982.

[71] J. N. Moum, , and W. D. Smyth. The pressure disturbance of a nonlinear internal wave train. *J. Fluid Mech.*, 558:153–177, 2006.

[72] J. N. Moum, D. M. Farmer, E. L. Shroyer, W. D. Smyth, and L. Armi. Dissipative losses in nonlinear internal waves propagating across the continental shelf. *J. Phys. Oceanogr.*, 37:1989–1995, 2007.

[73] J. N. Moum, D. M. Farmer, E. L. Shroyer, W. D. Smyth, and L. Armi. Energy transport by nonlinear internal waves. *J. Phys. Oceanogr.*, In Press, 2007.

[74] J. N. Moum, D. M. Farmer, W. D. Smyth, L. Armi, and S. Vagle. Structure and generation of turbulence at interfaces strained by internal solitary waves propagating shoreward over the continental shelf. *J. Phys. Oceanogr.*, 33:2093–2112, 2003.

[75] J. N. Moum and J. D. Nash. Seafloor pressure measurements of nonlinear internal waves. *J. Phys. Oceanogr.*, 38:481–491, 2008.

[76] D. E. Mowbray and B. S. H. Rarity. A theoretical and experimental investigation of the phase configuration of internal waves of small amplitude in a density stratified liquid. *Journal of Fluid Mechanics Digital Archive*, 28:1–16, 1967.

[77] L. A. Ostrovsky and Y. A. Stepanyants. Do internal solitons exist in the ocean? *Rev. Geophys.*, 26:293–310, 1989.

[78] T. M. Ozgokmen, T. Iliescu, and P. F. Fischer. Large eddy simulation of stratified mixing in a three-dimensional lock-exchange system. *Ocean Modeling*, 26:134–1556, 2009.

[79] L. L. Pauley, P. Moin, and W. C. Reynolds. The structure of two-dimensional separation. *J. Fluid Mech.*, 220:397–411, 1990.

[80] U. Piomelli. Wall-layer models for large-eddy simulations. *Progress in Aerospace Sciences*, 44:437–446, 2008.

[81] P. Puig, A. Palanques, J. Guillén, and M. El Khatab. Role of internal waves in the generation of nepheloid layers on the northwestern Alboran slope: Implications for continental margin shaping. *Journal of Geophysical Research (Oceans)*, 109(C18):9011–+, sep 2004.

[82] Luis Santos Quaresma, Joo Vitorino, Anabela Oliveira, and Jos da Silva. Evidence of sediment resuspension by nonlinear internal waves on the western portuguese mid-shelf. *Marine Geology*, 246(2-4):123 – 143, 2007.

[83] D. M. Reeder and M. B. Ma. Very large subaqueous sand dunes on the upper continental slope in South China Sea generated by episodic shoaling deep-water internal solitary waves. *J. Acoustic. Soc. America*, submitted, 2009.

[84] A. Saggio and J. Imberger. Internal wave weather in stratified lakes. *Limnol. Oceanogr.*, 43:1780–1795, 1998.

[85] T. Sakai and L. G. Redekopp. Models for strongly-nonlinear evolution of long internal waves in a two-layer stratification. *Non-Linear Processes in Geophysics*, 14:31–47, 2007.

[86] A. Scotti and J. Pineda. Observation of very large and steep internal waves of elevation near the Massachussetts coast. *Geophys. Res. Lett.*, 31:L22307, 2004.

[87] A. Scotti and J. Pineda. Plankton accumulation and transport in propagating nonlinear internal fronts. *Journal of Marine Research*, 65:117–145(29), January 2007.

[88] RL Simpson. Turbulent Boundary Layer Separation. *Ann. Rev. Fluid Mech.*, 21:205–234, 1989.

[89] W. D. Smyth and J. N. Moum. Length scales of turbulence in stably stratified mixing layers. *Phys. Fluids*, 12:1327–1342, 2000.

[90] T. P. Stanton and L. A. Ostrovsky. Observations of highly nonlinear internal solitons over the Continental Shelf. *Geophys. Rev. Let.*, 25(14):2695–2698, 1998.

[91] M. Stastna and K. G. Lamb. Large fully nonlinear internal solitary waves: The effect of background current. *Phys. Fluids*, 29(11):Article No. 1512, 2002.

[92] M. Stastna and K. G. Lamb. Vortex shedding and sediment resuspension associated with the interaction of an internal solitary wave and the bottom boundary layer. *Geophys. Rev. Let.*, 14(9):2987–2999, 2002.

[93] M. Stastna and K. G. Lamb. Sediment resuspension mechanisms associated with internal waves in coastal waters. *J. Geophys. Res.*, 113:10016–+, oct 2008.

[94] J. K. Sveen, Y. Guo, P. A. Davies, and J. Grue. On the breaking of internal solitary waves at a ridge. *J. Fluid Mech.*, 469(-1):161–188, 2002.

[95] Itiro Tani. Low-speed flows involving bubble separations. *Progress in Aerospace Sciences*, 5:70 – 103, 1964.

[96] S. A. Thorpe. *The Turbulent Ocean*. Cambridge University Press, 2005.

[97] S. A. Thorpe, A. Hall, and I. Crofts. The internal surge in loch ness. *Nature*, 237:96–98, 1972.

[98] B. Turkington, A. Eydeland, and S. Wang. A computational

method for solitary inernal waves in a continuously stratified fluid. *Studies in Applied Mathematics*, 85:93–127, 1991.

[99] S. K. Venayagamoorthy and O. B. Fringer. Numerical simulations of the interaction of internal waves with a shelf break. *Phys. Fluids*, 18(7):076603, 2006.

[100] B. J. Wang and L. G. Redekopp. Long internal waves in shear flows: Topographic resonance and wave-induced global instability. *Dyn. Atmos. Ocean.*, 33:263–302, 2001.

[101] Georges L. Weatherly and Paul J. Martin. On the structure and dynamics of the oceanic bottom boundary layer. *Journal of Physical Oceanography*, 8(4):557–570, 1978.

[102] K. B. Winters, J. McKinnon, and B. Mills. A spectral model for process studies of density stratified flows. *J. of Atmos. Ocean. Techn.*, 21(1):69–94, 2004.

[103] N. J. Zabusky and M. D. Kruskal. Interaction of "solitons" in a collisionless plasma and the recurrence of initial states. *Phys. Rev. Lett.*, 15(6):240–243, Aug 1965.

[104] J. Ziegenbein. Short internal waves in the strait of gibraltar. *Deep Sea Research and Oceanographic Abstracts*, 16(5):479 – 482, IN14–IN19, 483–484, IN20, 485–487, 1969.

[105] J. Ziegenbein. Spatial observations of short internal waves in the strait of gibraltar. *Deep Sea Research and Oceanographic Abstracts*, 17(5):867 – 875, 1970.